

論文 / 著書情報
Article / Book Information

題目(和文)	
Title(English)	Fabrication and Application of Micro Diaphragm-type Electromagnetic Actuators Utilizing Thin Film Permanent Magnet
著者(和文)	ZHICHAO
Author(English)	Chao Zhi
出典(和文)	学位:博士(工学), 学位授与機関:東京工業大学, 報告番号:甲第9692号, 授与年月日:2014年12月31日, 学位の種別:課程博士, 審査員:進士 忠彦,香川 利春,北條 春夫,初澤 毅,吉田 和弘
Citation(English)	Degree:Doctor (Engineering), Conferring organization: Tokyo Institute of Technology, Report number:甲第9692号, Conferred date:2014/12/31, Degree Type:Course doctor, Examiner:,,,,,
学位種別(和文)	博士論文
Type(English)	Doctoral Thesis

Fabrication and Application of Micro Diaphragm-type Electromagnetic Actuators Utilizing Thin Film Permanent Magnet

Supervisor:
Professor Tadahiko SHINSHI
Professor Haruo HOUJOH

Department of Mechano-Micro Engineering
Tokyo Institute of Technology

Chao ZHI

Abbreviations in this thesis

2D: Two-Dimensional

3D: Three-Dimensional

B_r : Magnetic Remanence

DEMA: Diaphragm-type ElectroMagnetic Actuator

H_c : Magnetic Coercivity

MEMS: Micro-Electro-Mechanical System

PDMS: PolyDiMethylSiloxane

PLD: Pulsed Laser Deposition

PMMA: PolyMethylMethAcrylate

TFPM: Thin Film Permanent Magnet

VSM: Vibration Sample Magnetometer

Contents

Chapter 1	Introduction	1
1.1	Background.....	1
1.1.1	Micro diaphragm-type actuators	1
1.1.2	Thin Film Permanent Magnet (TFPM)	3
1.1.3	Configuration of DEMA.....	5
1.2	Objective of this study.....	8
1.3	Thesis summary.....	9
Chapter 2	Micro DEMA utilizing TFPM and its application to a prototype pump	12
2.1	Introduction	12
2.1.1	Background of this chapter.....	12
2.1.2	Objective of this chapter.....	12
2.1.3	Solution	13
2.2	Principle and design of micro DEMA	13
2.2.1	Electromagnetic actuator design	13
2.2.2	Diaphragm design	17
2.3	Fabrication of the DEMA.....	19
2.3.1	TFPM fabrication on PDMS.....	19
2.3.2	Electromagnet fabrication.....	22

2.4 Evaluation of DEMA.....	23
2.4.1 Force evaluation.....	23
2.4.2 Displacement evaluation	24
2.5 Application of the DEMA to a prototype pump.....	26
2.5.1 Principle of the pump.....	26
2.5.2 Design and fabrication of the pump.....	27
2.5.3 Pump evaluations.....	29
2.6 Conclusion	34
2.6.1 Summary.....	34
2.6.2 Remaining problems and future work.....	34
 Chapter 3 MEMS process integration of TFPM with flexible diaphragm.....	 36
3.1 Introduction	36
3.1.1 Background of this chapter.....	36
3.1.2 Objective of this chapter.....	36
3.1.3 Solution	36
3.2 Proposal of fabrication process for TFPM integration with PDMS diaphragm	36
3.2.1 Proposed process	36
3.2.2 Fabrication	38
3.3 Evaluation of the flexible diaphragm with TFPM.....	41

3.3.1 TFPM magnetic property evaluation.....	41
3.3.2 PDMS mechanical property evaluation	42
3.3.3 Reaction temperature evaluation	44
3.3.4 Process optimization	51
3.4 Conclusion	53
3.4.1 Summary.....	53
3.4.2 Future work	54
 Chapter 4 Development of high force/energy density planar micro electromagnetic actuators and their applications to a flexible MEMS pump.....	 55
4.1 Introduction	55
4.1.1 Background of this chapter.....	55
4.1.2 Objectives of this chapter	58
4.1.3 Solutions	59
4.2 Analysis and proposals of the planar micro electromagnetic actuators using TFPM.....	 59
4.2.1 Characteristics of TFPM magnetic flux density.....	59
4.2.2 High performance planar micro electromagnetic actuators design...	63
4.2.3 Magnetic field Simulation	66
4.3 Fabrication of the planar-type electromagnetic actuators	68
4.3.1 Fabrication of TFPM patterns.....	68
4.3.2 Fabrication of permalloy layer by electroplating	71

4.3.3 Fabrication of micro-coil	73
4.4 Evaluation of the actuator	77
4.4.1 Evaluation of the magnetic property of TFPM	77
4.4.2 Evaluation of the magnetic property of permalloy	77
4.4.3 Evaluation of surface magnetic flux density	78
4.4.4 Evaluation of the electromagnetic force	79
4.4.5 Evaluation of force/energy density	81
4.4.6 Evaluation of misalignment effect on the actuator performance	82
4.4.7 Evaluation of PDMS diaphragm's displacement.....	87
4.5 Application of the actuator to a flexible MEMS pump.....	94
4.5.1 Design of the flexible MEMS pump	94
4.5.2 Fabrication of the flexible MEMS pump.....	94
4.5.3 Evaluation of the flexible MEMS pump.....	101
4.6 Further enhancement of the actuator's force	103
4.6.1 Alternate magnetization of TFPM	103
4.6.2 Scaling down of the permanent magnet feature size.....	105
4.7 Conclusion	108
4.7.1 Summary.....	108
4.7.2 Future work	109
Chapter 5 Conclusion and future work	110

5.1 Conclusions	110
5.2 Future works	112
References	113

Acknowledgements

Chapter 1 Introduction

1.1 Background

1.1.1 Micro diaphragm-type actuators

Micro-Electro-Mechanical System (MEMS) is a rapidly developing and promising industry currently. Many MEMS devices, such as accelerometers, pressure sensors and microphones have been successfully applied to automobiles, robotics and consumer products. In the next generation, in many intelligent devices such as microfluidic devices, wearable devices and point of care testing devices, MEMS-based sensors and actuators should play a more significant role. The MEMS market is predicted to reach 20 billion dollars until 2018 with a compound annual growth rate of 13% [1].

Among many MEMS devices such as micro pumps, energy harvesting devices and tactile displays [2-5], diaphragm-type actuators are commonly utilized. Diaphragm-type actuator consists of an actuator and a flexible diaphragm. Figure 1.1 shows a reciprocating micro pump driven by a diaphragm-type actuator. In the micro pump, the diaphragm together with the actuator moves up and down periodically. Meanwhile, the valves control the liquid flow direction by opening and closing the inlet and outlet. As a result, the pump function can be performed. In many MEMS devices, the diaphragm-type actuators usually possess the size of several square millimeter (mm^2) in area and several micrometer (μm) to several mm in thickness.

The actuator part in the diaphragm-type actuator varies much in principle. The most widely utilized ones are based on the principle of electrostatic, electromagnetic and piezoelectric. Their characteristics are listed in Table 1.1. Electrostatic actuator is suitable for MEMS integration process with a low power consumption. However, the driving voltage and frequency are high, and the

working distance is small. What is worse, the electrostatic actuator is sensitive to environment such as humidity and dust [6]. Piezoelectric actuator is similar with electrostatic actuator in driving voltage and working distance. Meanwhile, it can also be fabricated by MEMS processes such as Pulsed Laser Deposition (PLD) [7]. Compared with the above two kinds of actuators, electromagnetic actuator has long working range, and the driving voltage is low. Furthermore, it is robust and stable in humidity and dusty environment.

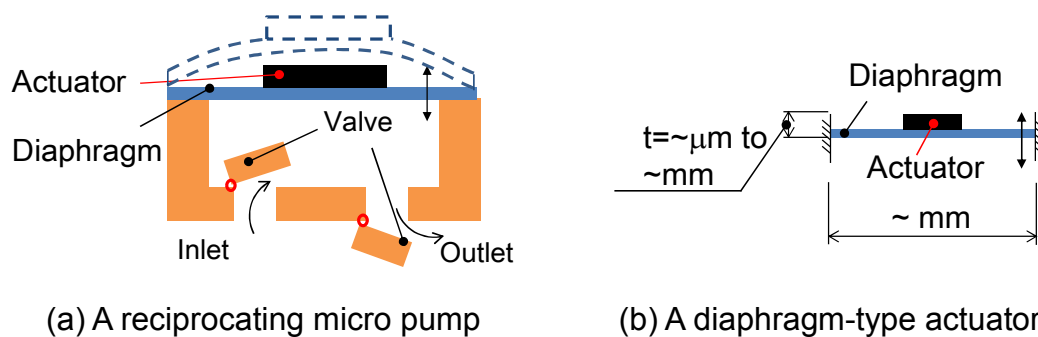


Fig. 1.1 Configuration of a diaphragm type actuator applied to a micro pump

Table 1.1 Actuator characteristics comparison

Actuator type	Driving voltage	Working distance	Integration
Electrostatic	0.1-1kV	0.1-10 μm	+++
Electromagnetic	1-10V	0.1-1mm	+
Piezoelectric (Film type)	0.1-1kV	0.1-10 μm	++

On the other hand, the diaphragm materials can be divided into two categories. One is based on non-polymeric materials such as metal, Si, SiO₂, etc. Their Young's moduli are in the range of several ten to several hundred GigaPascal (GPa). The Poisson's ratios are less than 0.3. The other category is made of polymers such as PolyMethylMethAcrylate (PMMA), Polyimide and PolyDiMethylSiloxane (PDMS). They possess Young's moduli from several MegaPascal (MPa) to several GPa, and their Poisson's ratios range from 0.3 to 0.5. The properties comparison of the diaphragm materials are summarized in

Table 1.2.

Table 1.2 Diaphragm material characteristics comparison

Diaphragm material	Young's modulus	Poisson's ratio
Metal/Si/SiN/SiO ₂ , etc	~10GPa to ~10 ² GPa	0.1 to 0.3
Polymer (PMMA, Polyimide, PDMS), etc	~MPa to ~GPa	0.3 to 0.5

The combination of the electromagnetic actuator with polymeric diaphragm, which is also called Diaphragm-type ElectroMagnetic Actuator (DEMA), exhibits the advantage of large displacement and low actuation voltage. Thus, it is a common actuator to drive tactile displays, micro valves and micro pumps [5, 8, 9].

1.1.2 Thin Film Permanent Magnet (TFPM)

Although electromagnetic actuator has the advantage of long working distance and low actuation voltage, it faces a bottleneck of integration. As mentioned by O. Cugat et al. [10], rare-earth-based bulk NdFeB or SmCo permanent magnet possesses high magnetic property with Magnetic Remanence (B_r) up to 1.1-1.5 Tesla (T) and Magnetic Coercivity (H_c) up to 0.8-1.1MA/m [62]. The fabrication processes are, however, limited to sintering or casting process. The feature size of sintering or casting process is in mm scale, thus micro patterning of bulk permanent magnet becomes rather difficult.

Y. Zhou et al. developed a micro pump utilizing a bulk NdFeB permanent magnet with a size of 3mm×3mm×0.5mm. J. Streque developed a tactile display in which permanent magnet arrays with unit size of Φ 1mm×0.5mm were utilized [5, 9]. The big size of the permanent magnets in the above MEMS devices is a limitation for the miniaturization and batch fabrication process.

For wafer level deposition processes of permanent magnet, conventional methods include electroplating, sputtering and Pulsed Laser Deposition (PLD)

[11]. Although electroplating is widely utilized in MEMS process as well as semiconductor process due to its low cost, low process temperature and fast fabrication rate, the resulting magnetic performance is not high. One reason is that permanent magnets fabricated by electroplating are usually based on CoPt, FePt or CoNiMnP. High performance NdFeB permanent magnets cannot currently be electroplated. The H_c of electroplated permanent magnets is usually in the range of 0.03MA/m to 0.2MA/m, and the B_r is less than 0.5T [12, 13, 21]. On the other hand, sputtering or PLD processes can realize NdFeB permanent magnets with H_c more than 0.6MA/m and B_r above 1T [14, 15, 16].

Table 1.3 Properties of different permanent magnets

Materials	Fabrication method	Thickness [μm]	B_r [T]	H_c [MA/m]	$(BH)_{max}$ [kJ/m³]	Heat resistance [K]
NdFeB [62]	Sintering	1000	1.1~1.5	0.8~ 1.1	~300	353~530
NdFeB/Ta [15]	Sputter	1	1.3	0.9	319	438
NdFeB [18]	Sputter	6	1.1	0.4	160	NA
FePt [19]	PLD	90	0.9	0.6	118	NA
NdFeB [20]	Screen printing	10~50	0.2~0.4	0.3~ 0.9	NA	NA
CoPt [21]	Electroplating	8	1.0	0.3	69	NA

Table 1.3 compares the properties of permanent magnets which are fabricated by different methods. It can be concluded that the thin film permanent magnet made of NdFeB/Ta [15] exhibited magnetic properties equivalent to the bulk sintered NdFeB permanent magnet [62]. The high B_r of 1.3T and high H_c of 1MA/m enable this NdFeB/Ta to generate larger magnetic field than other film-type permanent magnet. Furthermore, the sputtering method is compatible with

many MEMS processes. While for thin film permanent magnet made by other fabrication processes [18, 20] or using other materials [19, 21], their magnetic performances are inferior to the bulk NdFeB permanent magnet.

Figure 1.2 shows a cross section view of the multi-layered thin film NdFeB/Ta permanent magnet (TFPM) in [15]. Utilizing this TFPM, electromagnetically actuated MEMS devices can realize high performance, batch fabrication and miniaturization.

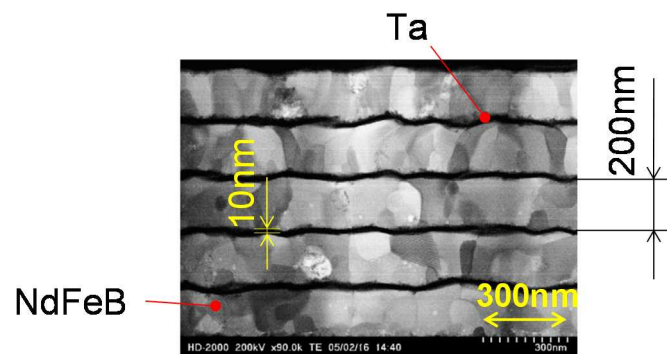


Fig 1.2 Cross section of the thin film NdFeB permanent magnet

1.1.3 Configuration of DEMA

As shown in Fig. 1.3, DEMA in MEMS is composed of the following three basic components:

- Flexible polymeric diaphragm (Made of PMMA, PDMS, Parylene or others)
- Moving actuator on the diaphragm (Made of film permanent magnet, bulk permanent magnet, planar coil or ferromagnetic material)
- External magnetic field source (Provided by bulk permanent magnet, bulk coil or planar coil)

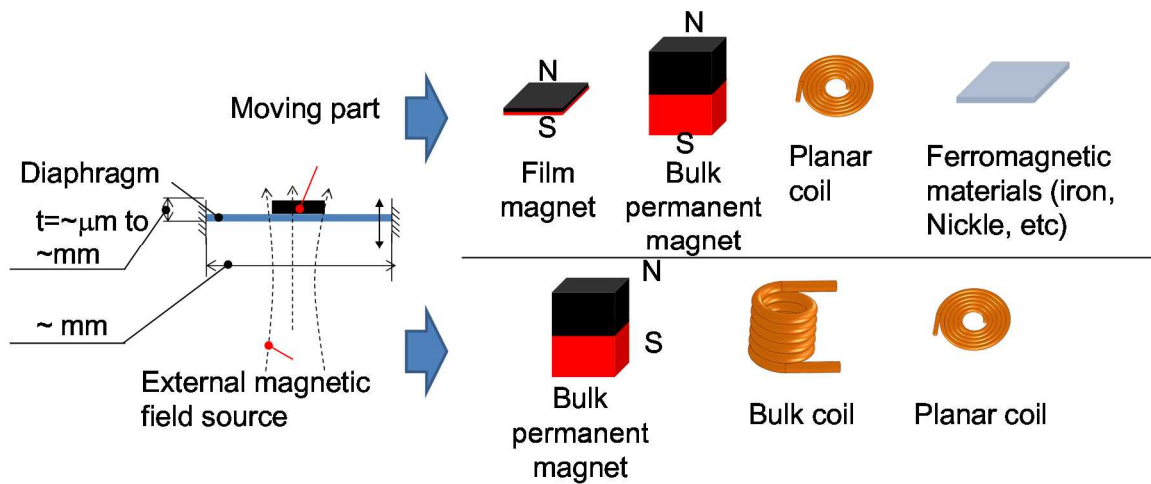


Fig. 1.3 Configuration of the DEMA

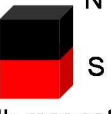



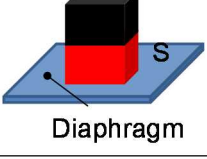
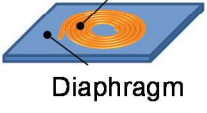
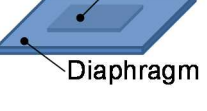
Different configurations of electromagnetic actuators are listed and compared in Table 1.4, in which the fabrication process of the moving part and the generated force are discussed.

In Cell 2-1, 2-2 and 2-3, the moving part is made of bulk permanent magnet, the fabrication process is sintering or casting. They are incompatible with batch fabrication and miniaturization.

In Cell 3-1, 3-2 and 3-3, the moving part is made of planar coil, the fabrication of planar coil on the diaphragm is compatible with MEMS process. However, the heat generation of the coil is a fatal problem. It would damage or deform the diaphragm [22]. Furthermore, due to the periodical movement of the diaphragm, the coil will easily become damaged under repeated stress [63].

In Cell 4-1, 4-2 and 4-3, the moving part is made of ferromagnetic material, the force generated between the external field and the moving actuator is limited to the attractive force. As a result, bi-directional actuation can not be realized.

Table 1.4 Comparison of electromagnetic actuators' configuration for DEMA
(Evaluation items: generated force and moving part fabrication process)

External Moving	 Bulk magnet	 Bulk coil	 Planar coil
 Film magnet Diaphragm	Easy for MEMS Difficult to control force direction 1-1	Easy for MEMS 1-2	Easy for MEMS Small force 1-3
 Bulk magnet Diaphragm	Large force Difficult to control force direction Not MEMS-based 2-1	Large force Not MEMS-based 2-2	Not MEMS-based 2-3
 Planar coil Diaphragm	Easy for MEMS Coil heat to diaphragm 3-1	Easy for MEMS Small force Coil heat to diaphragm 3-2	Easy for MEMS Small force Coil heat to diaphragm 3-3
 Ferromagnetic material Diaphragm	Easy for MEMS Difficult to control force direction Attractive force only 4-1	Easy for MEMS Attractive force only 4-2	Easy for MEMS Small force Attractive force only 4-3

When the moving part is made of film permanent magnet, there is no heat generation on the diaphragm and the diaphragm could be actuated bi-directionally. Furthermore, the film permanent magnet can be fabricated by MEMS processes. To drive the film permanent magnet using bulk permanent magnet in Cell 1-1, it is difficult to alternate the force direction. Thus, the reciprocation actuation is difficult. Despite such circumstances, Shen et al. [23] controlled the magnetic field direction by connecting the bulk permanent magnet with a rotational motor. It attained high energy efficiency compared with other kinds of electromagnetic actuators. However, it utilized the extra bulk motor.

Therefore, the configuration proposed in this thesis is the film permanent magnet driven by bulk coil in Cell 1-2 or film permanent magnet driven by planar coil in Cell 1-3.

1.2 Objective of this study

The objective of this study is focused on the research of DEMA using TFPM. The proposed DEMA should have the following features:

- High performance (Large force and long working distance)
- Fully MEMS-based fabrication (Fabricated by MEMS process, compatible with miniaturization and integration)

Micro pump is selected as a target device to apply the DEMA. It should have the characteristics of portability, flexibility and high performance. Figure 1.4 shows the prospective view of the micro pump and its future application.



Fig. 1.4 Flexible micro pump prospective view and its future application

The approaches to realize the research objective are as follows:

1. Realization of a DEMA using TFPM and bulk coil

A DEMA consisting of a moving film permanent magnet on a polymeric diaphragm and an external bulk coil should be proposed and evaluated. This DEMA should achieve the same performance as conventional DEMA utilizing bulk permanent magnet and bulk coil. The developed actuator will drive a pump.

This work will be done in Chapter 2.

2. Integration of TFPM with flexible diaphragm

TFPM integration process with flexible diaphragm should be solved. The fabrication process should not damage the magnetic property of TFPM and mechanical property of the diaphragm. Furthermore, the process should be MEMS-based. This work will be done in Chapter 3.

3. Realization of a DEMA using TFPM and planar coil

Electromagnetic actuators consisting of TFPM driven by planar coils should be proposed. The actuators should be fabricated by fully MEMS process. Furthermore, effort should be made to increase the generated force. The actuators will be applied to drive a MEMS pump. Meanwhile, TFPM and planar coil should enable the flexibility and portability of the MEMS pump. These works will be done in Chapter 4.

1.3 Thesis summary

This thesis is summarized as follows:

Chapter 2 “Micro DEMA utilizing TFPM and its application to a prototype pump”

An electromagnet to drive a TFPM on a PDMS diaphragm is designed and optimized. A 3mm diameter and 20 μ m thick TFPM is sputtered on a 50 μ m thick Nb substrate and bonded with a flexible PDMS diaphragm. The electromagnet has a closed magnetic circuit. Several shapes of magnetic core are designed to concentrate the magnetic flux around the TFPM area. The force and working displacement of the DEMA are simulated and experimentally measured. The DEMA is then utilized to drive a diffuser valveless prototype pump. The pump's flow rate, pressure are measured. The temperature of the electromagnet is also

measured.

In this chapter, three problems remain. Firstly, TFPM integration with PDMS is not compatible with batch fabrication and miniaturization. Secondly, bulk electromagnet is selected instead of the planar micro coil to generate sufficient force. The coil has large size and is fabricated by mechanical wiring. Thus, it is not suitable for portable application and miniaturization. Thirdly, the prototype pump is made of high stiffness material and is not suitable for flexible application. These problems are to be solved in Chapter 3 and Chapter 4.

Chapter 3 “MEMS process integration of TFPM with flexible diaphragm”

A MEMS fabrication process that enables a flexible PDMS diaphragm to be integrated with TFPM is proposed. TFPM can not be sputtered directly on PDMS because the high sputtering temperature will damage PDMS. The proposed process involves, firstly, sputtering the TFPM onto a Si substrate, then coating this with PDMS, and finally etching Si by XeF_2 gas. The heat generated during the XeF_2 etching process degrades the magnetic property of the TFPM. Meanwhile, it detaches TFPM from the PDMS layer. The substrate temperature in XeF_2 etching process, the magnetic properties of the TFPM and the mechanical properties of the PDMS diaphragm are evaluated experimentally. The parameters during XeF_2 etching process can be adjusted considering temperature requirements.

Chapter 4 “Development of high force/energy density planar micro electromagnetic actuators and their applications to a flexible MEMS pump”

Several planar-type micro electromagnetic actuators are proposed consisting of patterned TFPM, mesh coils and ferromagnetic layers. Different from conventional planar micro electromagnetic actuators having a film permanent magnet and a spiral micro-coil, this chapter originally proposes segmentation patterns of TFPM such as line/space and chessboard, and mesh coils

surrounding the segmentations. The TFPMs are segmented to reduce the self-demagnetization factor and to generate larger flux densities. The generated magnetic flux density is further enhanced by covering TFPM with permalloy layer. The proposed micro-coils possess a Two-Dimensional (2D) structure and are easy to fabricate compared with spiral shape micro-coil. In the simulation, the segmented TFPM can generate force that is several times larger than that of without segmentation. Furthermore, the actuator's force magnitude is enhanced by covering a ferromagnetic layer on TFPM patterns. The proposed actuators are fabricated by fully integrated MEMS processes. The magnetic flux densities, the electromagnetic forces and the alignment errors between TFPM and micro-coil are simulated and measured. Meanwhile, the force density and energy density of the proposed electromagnetic actuator are defined and evaluated. The patterned TFPM is then attached to PDMS diaphragm and driven by the micro-coil. The diaphragm displacement is evaluated.

A flexible MEMS pump is fabricated using a PDMS-based pump body. The micro-coil could become flexible by depositing copper pattern on flexible polyimide film. The DEMA consisting of planar type micro electromagnetic actuator is utilized to actuate the MEMS pump. However, due to the alignment error between TFPM pattern and micro-coil, the MEMS pump could not work currently.

Chapter 5 “Conclusion and future work”

This chapter summarizes the achieved results in previous chapters. Future works of this study are also proposed.

Chapter 2 Micro DEMA utilizing TFPM and its application to a prototype pump

2.1 Introduction

2.1.1 Background of this chapter

Currently, DEMAs in MEMS pumps consist of bulk permanent magnets bonded with flexible diaphragms. The flexible diaphragms with permanent magnets are driven by coils with iron cores. To drive the micro pumps using DEMA, the generated magnetic force is from 1mN to 100mN, and the diaphragm displacement is from 10 μ m to 500 μ m.

C. Yamahata et al. [24] bonded a Φ 3mm \times 3mm NdFeB permanent magnet on a PDMS diaphragm utilizing a molding process. The electromagnet was composed of a coil with 4800 turns and an iron core. C. Yamahata further fabricated a bond permanent magnet using the NdFeB powder mixed with resin [25]. However, the B_r of NdFeB/resin decreased from 0.75T to 0.3T because the permanent magnet powder volume ratio in the bond permanent magnet is 40%. The force of actuators in [24, 25] reached around 100mN. The diaphragm displacement was not mentioned. Y. Zhou et al. placed a 3mm \times 3mm \times 0.5mm NdFeB permanent magnet into an 800 μ m thick PDMS diaphragm. The electromagnet was composed of a hand-wired coil with 924 turns and an iron core [9]. This DEMA realized 30mN force with 34 μ m displacement. The use of the bulk NdFeB permanent magnet in the above references made the micro pumps not only bulky, but also incompatible with batch fabrication process.

2.1.2 Objective of this chapter

This chapter aims to develop a DEMA utilizing TFPM. The force of the DEMA should attain mN order. The displacement should attain several hundred μ m order.

2.1.3 Solution

To generate sufficient force on TFPM, an electromagnet with a closed magnetic circuit is designed. TFPM is bonded with a low stiffness diaphragm to attain the required displacement.

2.2 Principle and design of micro DEMA

2.2.1 Electromagnetic actuator design

A configuration of the electromagnetic actuator for DEMA in orthogonal coordinate system is shown in Fig. 2.1. According to Ampere's law, the magnetic force applied on an elemental volume of permanent magnet by the external magnetic field is given in Eq. 2.1 [26, 27].

$$d\vec{F}_{mag} = (\vec{M} \cdot \nabla) \vec{B} dV \quad (2.1)$$

Where

\vec{M} : Magnetization of the permanent magnet

\vec{B} : External magnetic flux density

V : Volume of the permanent magnet

\vec{F}_{mag} : Electromagnetic force working on the permanent magnet

As the DEMA works in the Z direction, the force in the Z direction is only considered in the following contents. Assuming the thickness is much smaller than the length and width in the case of TFPM. Eq. 2.1 can be transformed to Eq. 2.2.

$$F_{mag_Z} \approx M_z h \int_S \frac{dB_z}{dz} dS \quad (2.2)$$

Where

h : Thickness of TFPM

S : XY cross section of TFPM

From Eq. 2.2, the magnetic force is proportional to the TFPM's thickness and the magnetic flux density gradient in Z direction (dB_z/dz). In order to increase the actuation force, increasement of dB_z/dz is necessary because the increasement of TFPM's thickness is limited.

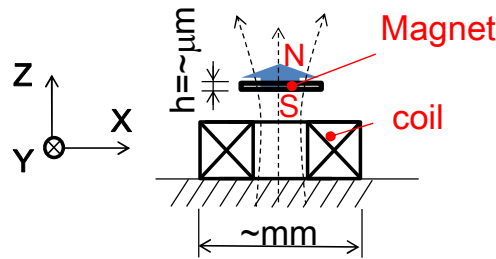


Fig. 2.1 Proposed DEMA configuration

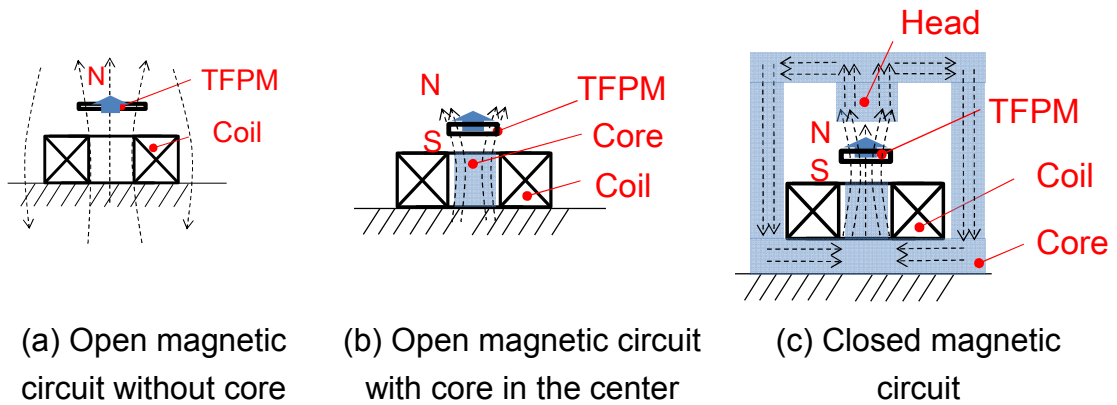


Fig. 2.2 Comparison of open and closed loop magnetic circuits

To design the electromagnet, closed magnetic loop is utilized because it can greatly decrease the magnetic resistance and concentrate the magnetic flux density into the magnetic core. The open and closed magnetic circuit design are illustrated in Fig. 2.2. The arrows show the flow of magnetic flux. In Fig. 2.2(a), there is no core in the coil. In Fig. 2.2(b), there is a magnetic core in the center of the coil. In Fig. 2.2(c), there is a closed magnetic core.

The closed loop electromagnet are designed in Figs. 2.3 (a, b) and compared

with the electromagnet that only has core in the center in Fig. 2.3(c). The default unit in Fig. 2.2 and the following figures is millimeter. The size of the electromagnet is 32mm in diameter and 22mm in height. The cross section of the coil is 10mm×10mm with a core of 6mm in diameter at bottom and 3mm in diameter at top. The material of the core is pure iron with a magnetic flux density saturation around 2.2T. The distance between TFPM's center plane and the head is 0.5mm. is 0.5mm.

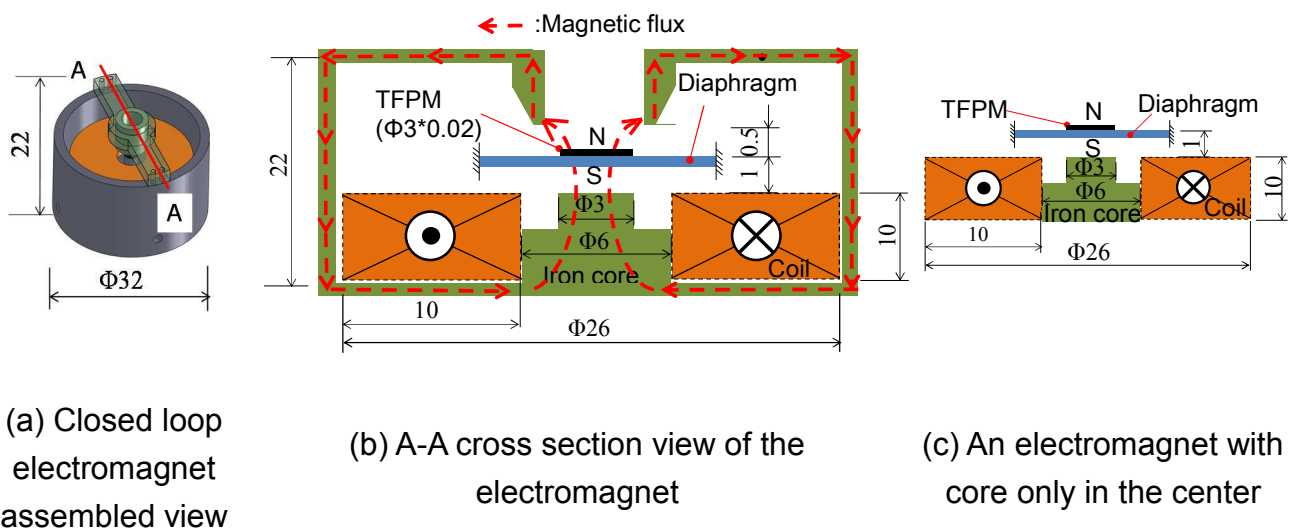


Fig. 2.3 Designed electromagnets

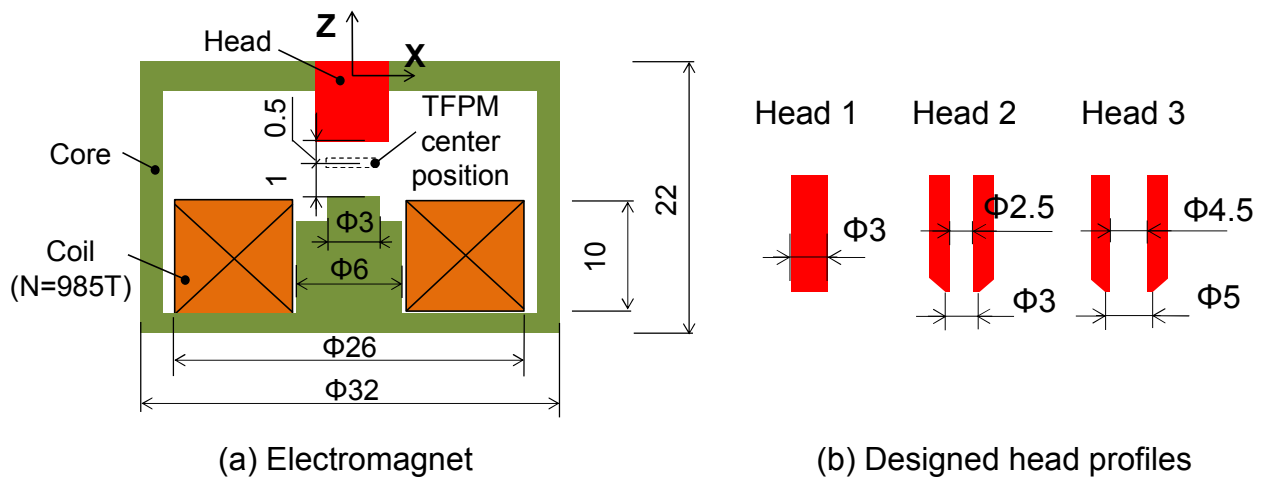


Fig. 2.4 Closed electromagnet with head variations

FEM magnetic analysis software (Maxwell 3D Ver. 14, Ansys Japan) is used to calculate the electromagnetic flux density and force. In the simulation, the TFPM is magnetized in +Z direction. The current input into the coil is shown in Fig. 2.3(b) to generate a magnetic flux density in the +Z direction in the center core.

The head profile of the electromagnet, as shown in Fig. 2.4(a), affects much on the electromagnetic force. Three different head profiles are designed in Fig. 2.4(b). Head 1 is a column-shaped one, which is commonly utilized in closed electromagnet designs. Head 2 and Head 3 have holes in the center. The hole in Head 3 is larger than that of Head 2. Furthermore, the bottoms of Head 2 and Head 3 are cone shape to concentrate the magnetic flux density at the TFPM position.

The forces generated by the electromagnet with three different heads and without head are compared in Fig. 2.5. The force magnitude increases linearly with the increase of the coil current. Furthermore, the electromagnet with Head 3 can generate the largest negative force. Unlike others, the force generated by the electromagnet with Head 1 is positive.

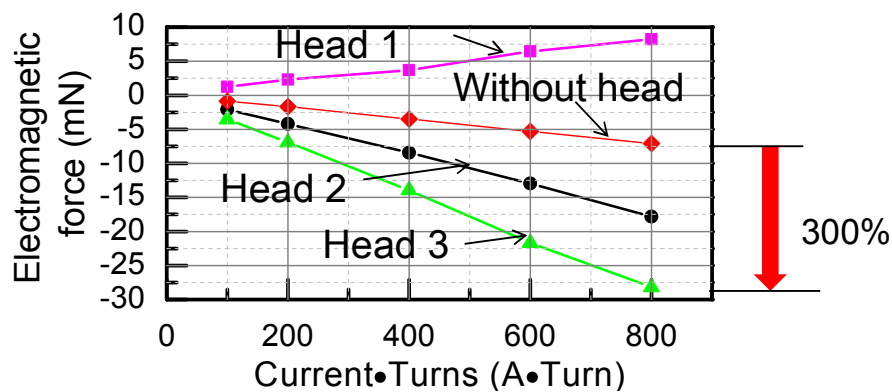


Fig. 2.5 Simulated force on the TFPM

To explain the force direction and magnitude in Fig. 2.5, the magnetic flux density gradient in the Z direction (dB_z/dz) is analyzed. The dB_z/dz generated by

the electromagnet along the TFPM center position indicated in Fig. 2.4(a) is shown in Fig. 2.6. For the electromagnet with Head 1, the dB_z/dz is positive in the range of $-1.5\text{mm} \leq X \leq 1.5\text{mm}$. Thus the integrated force is positive. However, for Head 2 and Head 3, dB_z/dz in the same area are negative. Thus, the integrated forces are negative. Furthermore, for Head 3, the integration of dB_z/dz is larger than that of Head 2 in magnitude. Head 3 is selected for the electromagnet as it can generate the largest electromagnetic force.

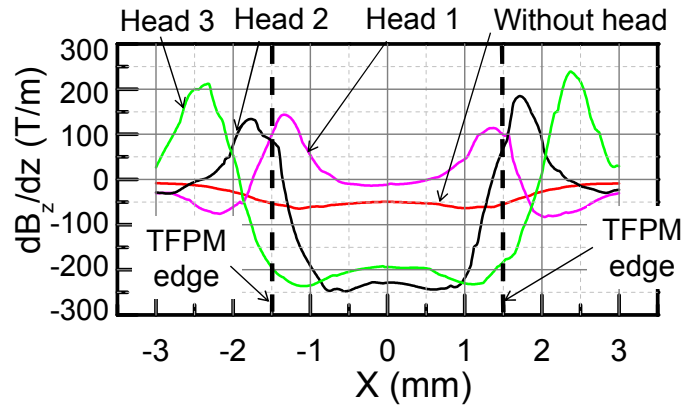


Fig. 2.6 Magnetic flux density gradient along the TFPM centerline

2.2.2 Diaphragm design

The diaphragm with TFPM in the DEMA is shown in Fig. 2.7. The TFPM is placed in the center of the diaphragm. The diameters of the diaphragm and the TFPM are 7mm and 3mm. The diaphragm structure can be modeled as a fixed-edge disk. The electromagnetic force on the TFPM is assumed to distribute uniformly.

3D CAD (SolidWorks Simulation, 2012, SolidWorks Corp.) is used to calculate the diaphragm displacement. The solver is non-linear analysis using large displacement calculation model.

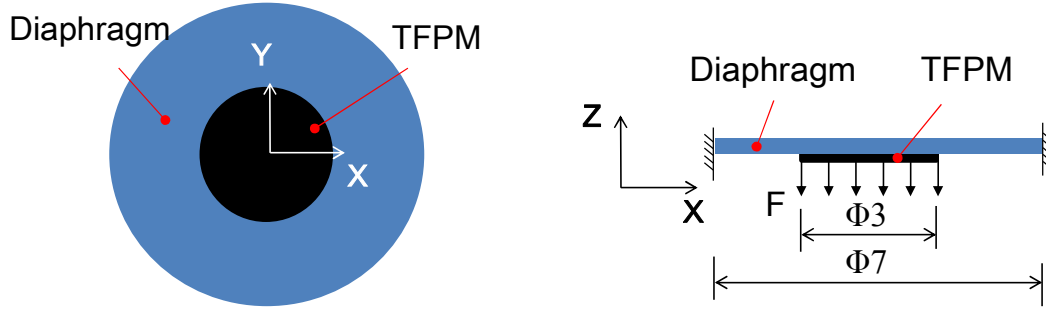


Fig. 2.7 Fixed-edge diaphragm with uniform load in the center circular area

Table 2.1 Mechanical properties of candidate diaphragm materials

Material	Young's modulus	Poisson's ratio	Yield strength/ tensile strength
Si [28, 29]	160.0 GPa	0.3	120.0 GPa
Polyimide [30]	2.5 GPa	0.34	0.231 GPa
PDMS [31, 32]	0.002 GPa	0.45	0.007 GPa

Three kinds of materials are used as diaphragm candidates: Si, polyimide and PDMS. Their mechanical parameters for simulation are listed in Table 2.1. The mechanical property of TFPM is same as in [43, 62]. Other settings for simulation are: electromagnetic force 30mN; TFPM thickness 20 μ m.

For each candidate diaphragm, the thickness is adjusted to meet the required displacement. The maximum displacement with the relationship of thickness is shown in Fig. 2.8. As the thickness of TFPM is 20 μ m, the thickness of the diaphragm ranges from 20 μ m to 100 μ m.

In the case of Si diaphragm, the displacement is in the order of 1 μ m to 10 μ m. The displacement for polyimide diaphragm is from 10 μ m to 100 μ m. While for PDMS diaphragm, the displacement ranges from 500 μ m to 1000 μ m, which meets

the requirement of the diaphragm displacement. Considering the fact that PDMS is difficult to operate when it is very thin (less than $60\mu\text{m}$), $80\mu\text{m}$ thick PDMS is finally selected. Besides the mechanical property, the PDMS also possesses the property of transparency, stability, bio-compatibility and easy operation, which is a common material in microfluidic field and biological engineering.

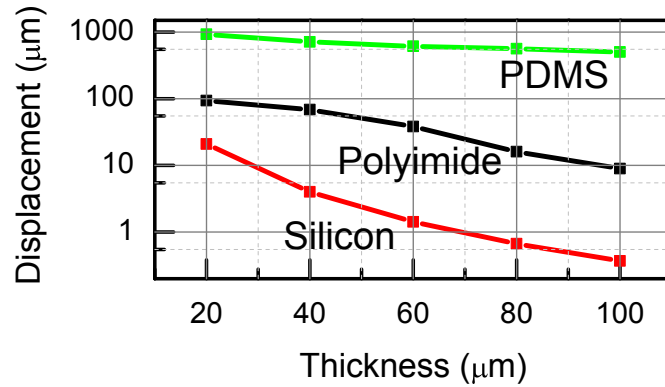


Fig. 2.8 Diaphragm's thickness-displacement curve

2.3 Fabrication of the DEMA

2.3.1 TFPM fabrication on PDMS

TFPM is fabricated by magnetron sputtering process. The sputtering parameters are listed in Table 2.2 [15, 59]. The sputtering temperature of 733K exceeds PDMS's temperature limitation which is around 473K [33], so that directly depositing TFPM on PDMS is impossible. A tentative method is to sputter TFPM on a metal sheet, followed by bonding with the PDMS diaphragm.

Four types of metal sheet are tested as substrates for sputtering: $12\mu\text{m}$ thick Al sheet, $10\mu\text{m}$ thick Cu sheet, $15\mu\text{m}$ thick Nb sheet and $50\mu\text{m}$ thick Nb sheet. TFPM thickness is first set to be $6\mu\text{m}$ that consists of 200nm NdFeB and 10nm thick Ta deposited sequentially. Ti plate with a hollow pattern in the center is used as a hard mask to cover the substrate during sputtering.

Table 2.2 Sputtering parameters

Target composition	Nd ₄₁ FeB _{1.2} Co ₁ (wt%) and Ta (99.95%)
Sputtering temperature	733K
Pressure	Base pressure better than 3×10^{-4} Pa; Ar working pressure 0.6Pa
Power	Co-doped NdFeB: RF-500W; Ta: RF-300W
Average rate	NdFeB: 3nm/s; Ta: 0.8nm/s

Table 2.3 shows the TFPM's magnetic properties on four types of substrates compared with a typical SiO₂ substrate. The heat resistance of the TFPM is defined as the temperature at which the irreversible magnetic flux density loss reaches -5%. It is 438K for a SiO₂ substrate, noted by Uehara [17].

In the case of Al sheet, damage occurs in the sputtered areas. It is because the temperature at the sputtered area is higher than 733K due to the ion particle's kinetic energy transferred to the substrate. The temperature of the substrate is increased and is close to the melting point of Al around 923K.

Cu sheet can resist high temperature, so the TFPM keeps its profile. However, the diffusion of Cu into NdFeB decreases the H_c to 0.6MA/m, the Cu effect on the magnetic performance is discussed in detail in [34]. Heat resistance of TFPM also decreases from 438K to less than 363K.

The Nb sheet of 15 μ m in thickness can maintain the TFPM's magnetic property. However, the residual stress after sputtering deforms the sheet. The Nb sheet of 50 μ m is finally selected. The sputtered 6 μ m thick TFPM on different metal substrates are illustrated in Fig. 2.9.

The 20 μ m thick TFPM on 50 μ m thick Nb substrate is then fabricated. To reduce the deposition time of TFPM, the thickness of NdFeB layer is changed from 200nm to 300nm. The Ta layer's thickness keeps the same. The fabrication results are shown in Fig. 2.10.

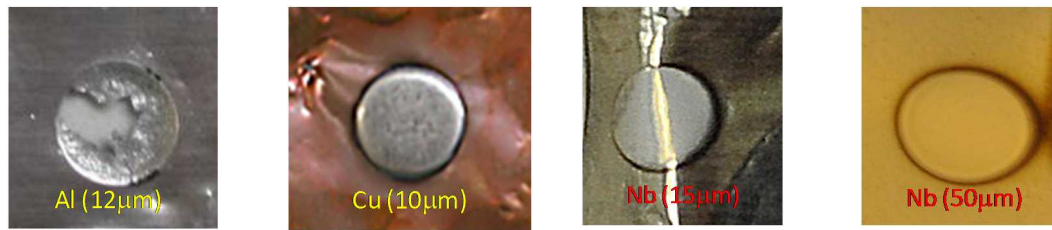


Fig. 2.9 Sputtered 6μm thick TFPM on four kinds of substrates

Table 2.3 TFPM characteristics on different substrates as sputtering

Substrate		Magnetic property			Comment
Material	Thickness	B_r	H_c	Heat resistance	
SiO ₂	—	1.25T	1.32MA/m	438K	Typical substrate
Al	12μm	NA	NA	NA	Damaged
Cu	10μm	1.20T	0.6MA/m	< 363K	H_c decreased
Nb	15μm	1.30T	1.25MA/m	> 363K	Surface deformation
	50μm	1.32T	1.05MA/m	> 363K	



Fig. 2.10 Sputtered 20μm thick TFPM on 50μm thick Nb substrate

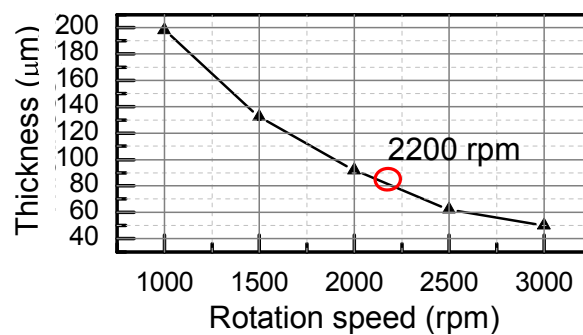


Fig. 2.11 Rotation speed and thickness of PDMS

Meanwhile, the PDMS (SIM-260, CAT-260, Shin-Etsu Chemical Co., Japan) is used to fabricate the diaphragm. PDMS pre-polymers of SIM-260 base and CAT-260 curing agent are firstly mixed with the weight ratio of 10:1, followed by being degassed in a vacuumed chamber (ASONE Corp., Japan). Then, the liquid state PDMS is spin-coated on a glass wafer at a speed of 2200rpm for 30s and cured at 348K for four hours on a hot plate. Finally, the PDMS film is peeled off from the glass substrate.

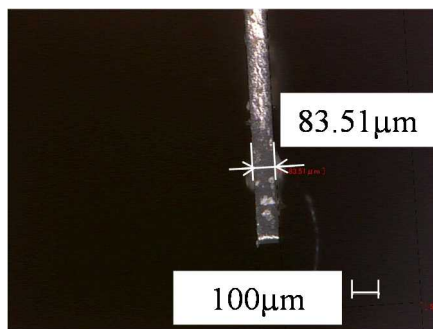


Fig. 2.12 PDMS thickness measurement

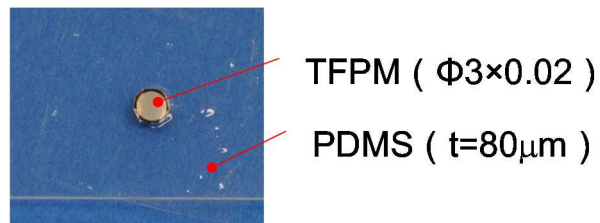


Fig. 2.13 TFPM bonded with PDMS diaphragm

The PDMS thickness is measured by a CCD microscope (VW-6000SP, Keyence Co.). Figure 2.11 shows the relationship between rotational speed and the thickness of PDMS film. Figure 2.12 shows the side view of the PDMS film taken by the CCD microscope, which shows that the diaphragm thickness is 83.5μm.

The TFPM sputtered on Nb substrate is then bonded on PDMS diaphragm by uncured PDMS. After curing process, two parts bond together irreversibly. The fabricated PDMS diaphragm with TFPM is shown in Fig. 2.13.

2.3.2 Electromagnet fabrication

The electromagnet is fabricated by conventional mechanical machining process. The custom-made coil has 985 turns with electric resistance 13Ω. Figure

2.14(a) shows the photograph of the electromagnet parts. The electromagnet with the coil inside is then filled with epoxy resin to fix the coil position. The assembled electromagnet is shown in Fig. 2.14(b).

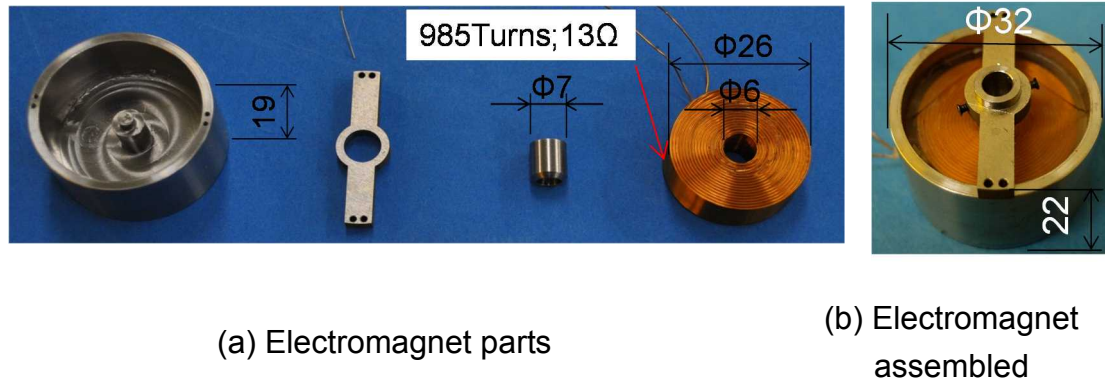


Fig. 2.14 Electromagnet fabrication

2.4 Evaluation of DEMA

2.4.1 Force evaluation

An electronic force balance with a resolution of 0.1mg (Sefi ITX-220 ASONE Corp.) is utilized to measure the electromagnetic force between TFPM and the coil. The measurement setup is shown in Fig. 2.15. The electromagnet is placed on the stage of the electronic force balance. The magnetized TFPM on the Nb substrate is fixed by a non-magnetic holder which is connected with an outside fine stage. The gap between the TFPM and the electromagnet is adjusted by the fine stage with 10 μ m positioning resolution in X-Y-Z direction. When a current passes through the coil, an electromagnetic force is generated on the TFPM. The force on the electromagnet causes a variation to the measurement result.

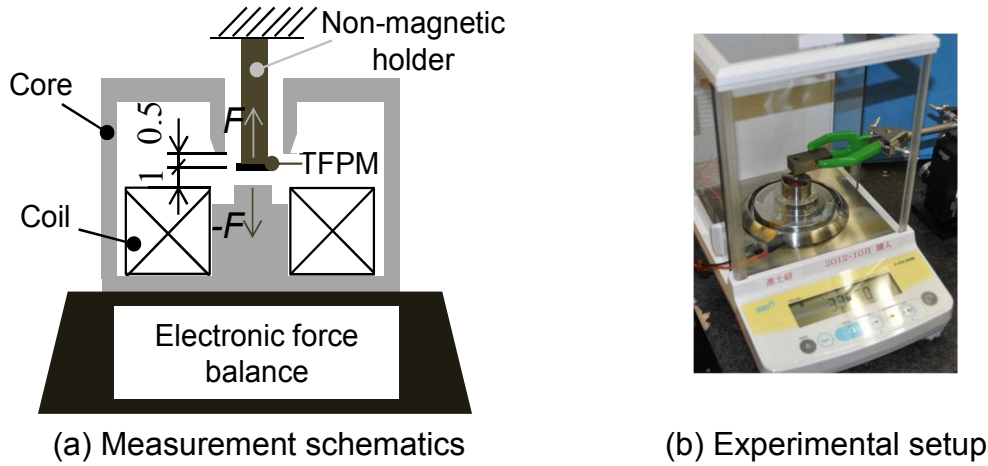


Fig. 2.15 Electromagnetic force measurement

Figure 2.16 shows the measured force in comparison with the simulated one. There is good agreements between the simulated and experimental results. The electromagnetic force has a linear relationship with input current. The simulated and experimental coefficients are 35.07mN/A and 35.75mN/A, respectively.

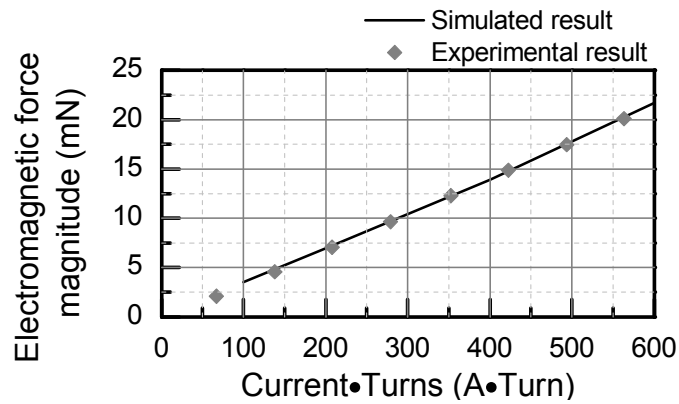


Fig. 2.16 Comparison of electromagnetic force in simulation and experiment

2.4.2 Displacement evaluation

A schematic view of the diaphragm displacement measurement is shown in Fig. 2.17. A PDMS diaphragm attached with TFPM is clamped by acrylic plates with a hole in the center. Following that, they are assembled with the electromagnet. The displacement of the PDMS diaphragm is measured by a laser

displacement sensor (LK-G155, Keyence Corp. Japan) with a measurement range of 4mm and a resolution of 10 μ m.

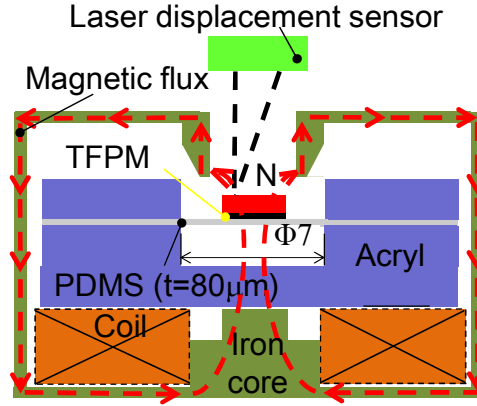


Fig. 2.17 Diaphragm displacement measurement setup

The measured diaphragm displacement and coil current are shown in Fig. 2.18(a). Utilizing the experimental force-current coefficient of 35.75mN/A calculated from Fig. 2.16, the relationship between force and displacement is derived, shown as the solid line in Fig. 2.18(b). Furthermore, the measured displacement is compared with the simulated one in Fig. 2.18(b). There is a good agreement between simulation and experiment. The experimental result demonstrates that the DEMA could reach $\pm 500\mu$ m displacement.

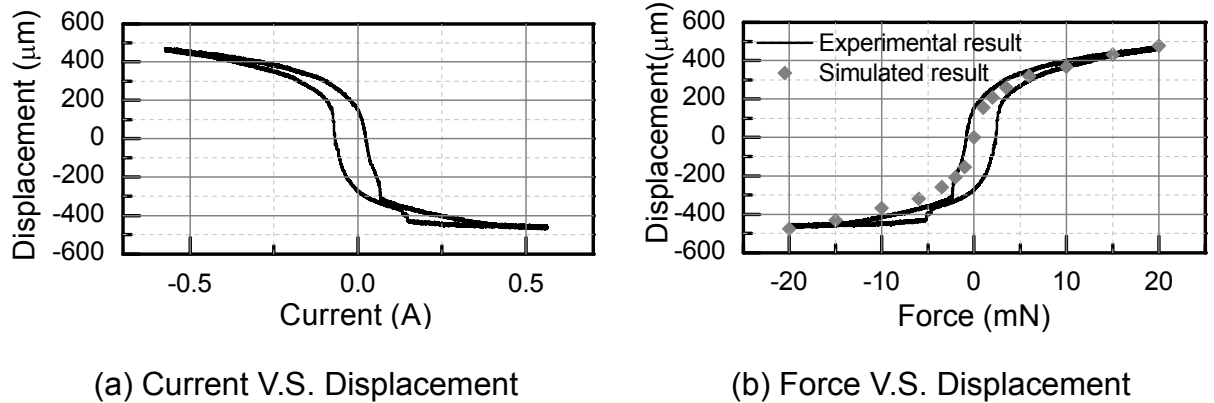


Fig. 2.18 Displacement characteristic of the DEMA

2.5 Application of the DEMA to a prototype pump

2.5.1 Principle of the pump

The developed DEMA is utilized to actuate a prototype pump. A diffuser type valveless pump is selected for the DEMA application. The characteristics of this type of pump are: no moving valve, simple structure and easy fabrication.

The principle of the diffuser valveless micro pump is shown in Fig. 2.19. The pump consists of an external coil and a pump chip. TFPM is bonded onto a diaphragm. When a current passes through the coil, an electromagnetic force is generated on the TFPM, leading to the deformation of the diaphragm. When the direction of the current is reversed, the diaphragm moves in the opposite direction.

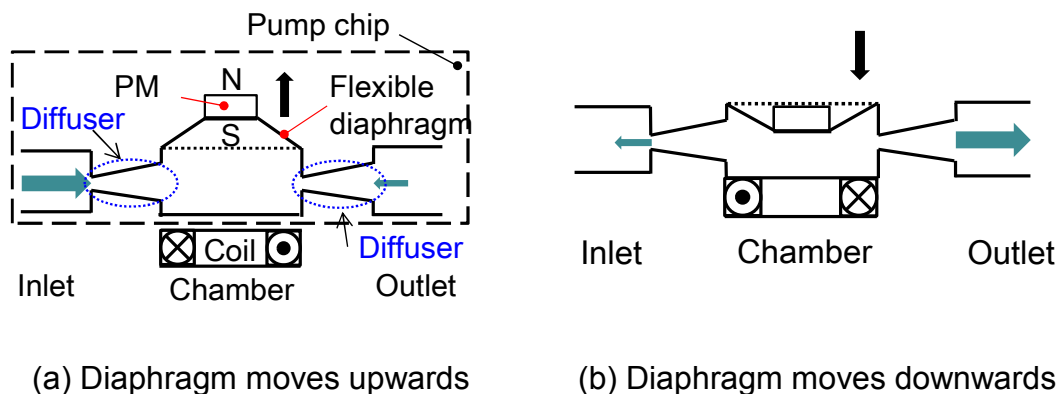


Fig. 2.19 Diffuser type pump working principle

Diffuser components connect the chamber with the inlet and outlet ports. It has been proved that, for a certain range of expanding angle, the diffuser has a smaller fluidic resistance in the diverging direction than converging direction [2]. This results in more liquid flowing into the chamber from the inlet than outlet when the diaphragm moves upward. On the contrary, when the diaphragm moves downwards, more liquid flows out from the outlet. After a complete pump cycle, a net flow is generated from the inlet to the outlet. By repeating the above cycle, the pump can transport liquid (or gas) from the inlet to the outlet.

2.5.2 Design and fabrication of the pump

The diffuser element in diffuser valveless pump is the most important part. Its parameters such as the length, the angle, and the throat width affect pump efficiency greatly. Olsson et al. [2], Yamahata et al. [25] and many other researchers have investigated the diffuser properties from the aspects of experiment and simulation. The diffuser parameters selected in this thesis are the optimized one which is discussed in detail in [25].

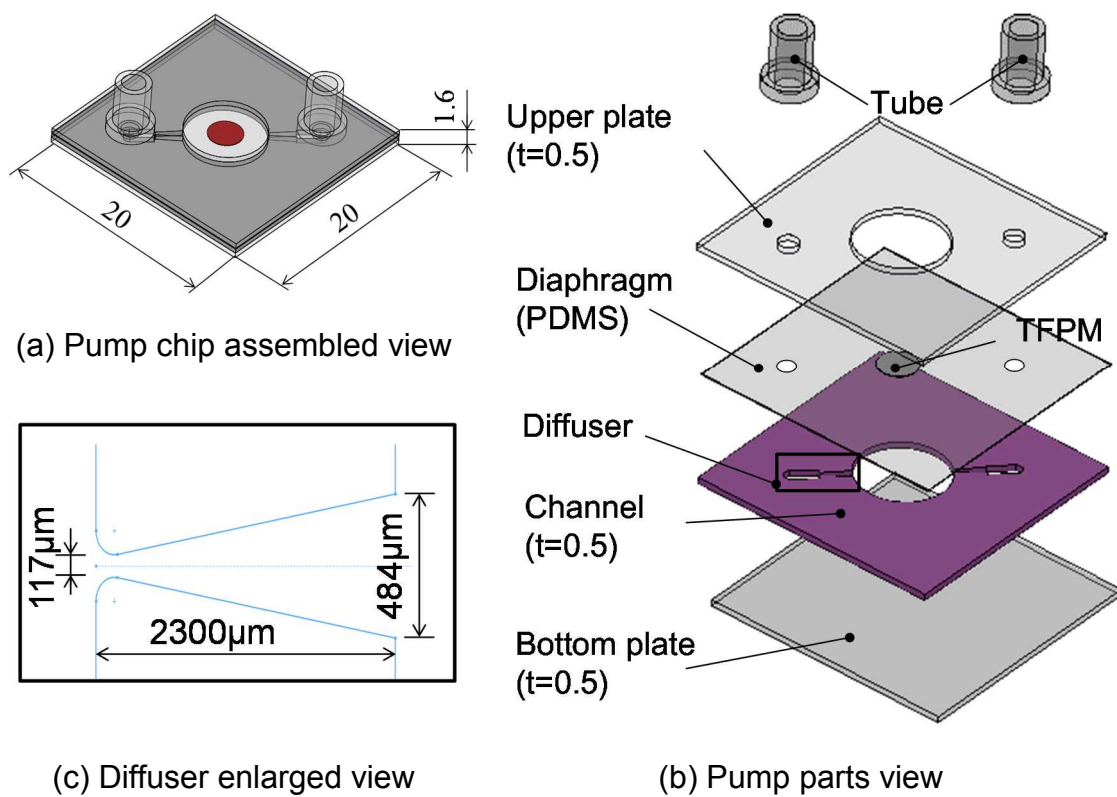


Fig. 2.20 Diffuser valveless pump design

The designed pump is shown in Fig. 2.20. The pump chip has a total size of 20mm×20mm×1.6mm. It consists of several plates. Apart from the diaphragm which is made of PDMS, the other plates' thicknesses are all 0.5mm. The diffuser's parameters are shown in Fig. 2.20(c).

The prototype pump is fabricated. The upper and bottom plates are made of

acryl and fabricated by a CO₂ laser cutting machine (L-906PC, IIDA KOGYO Co.). Three materials are tested to fabricate the channel plate. The materials of the plate, the fabrication methods and the fabrication results are compared in Table 2.3. The diffusers machined by laser cutting in the acryl plate and quartz exhibit fabrication error around 100 μ m. Furthermore, the surface after fabrication are not smooth and tapers exist on the cutting surface. The Ti substrate fabricated by wire cutting is selected due to its fine profile.

Table 2.3 Fabrication of the channel plates

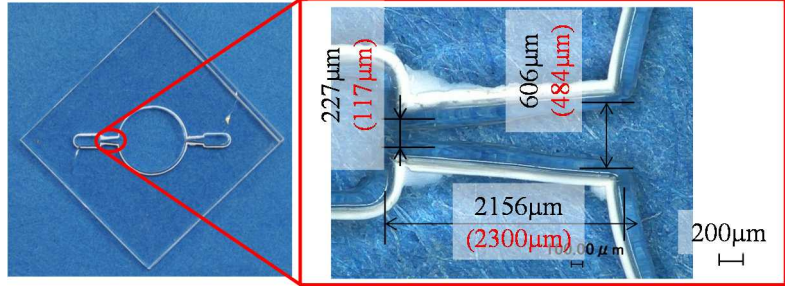
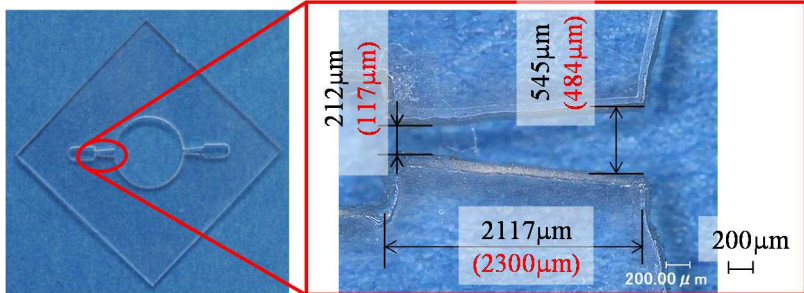
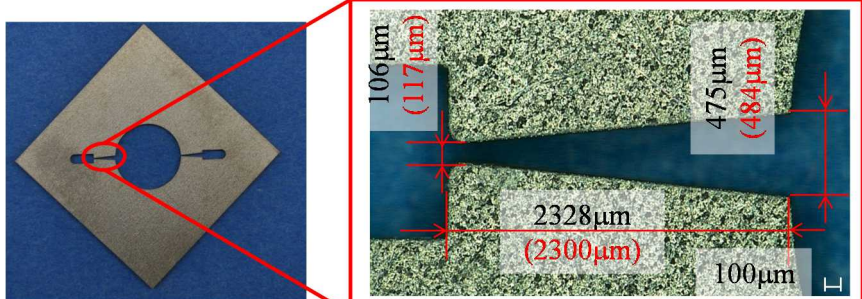
Material	Method	Fabrication result
Acryl	CO ₂ laser cutting	
Quartz	CO ₂ laser cutting	
Ti	Wire cutting	

Figure 2.21(a) shows the fabricated pump chip. A square shape sink with 0.5mm depth, shown in Fig. 2.21(b), is fabricated in the epoxy resin of electromagnet as an assembling hole for pump chip. The pump chip is then assembled with electromagnet, shown in Fig. 2.21(c). The assembled pump has a total size of 32mm in diameter and 22mm in height.

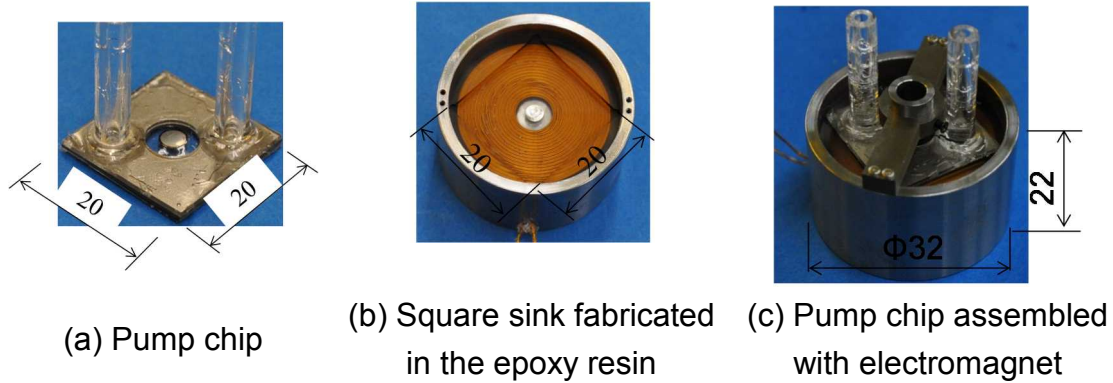


Fig. 2.21 Fabrication of the prototype pump

2.5.3 Pump evaluations

2.5.3.1 Evaluation of flow rate/pressure

The flow rate/pressure of the fabricated micro pump is evaluated. The experimental setup is shown in Fig. 2.22(a). Ethanol is used as the experimental liquid because of its small surface tension. Video camera is used to observe the liquid in the tube. Sinusoidal and square wave voltage signal are input into the coil respectively with voltage amplitude variation from 1V to 8V. The flow rate is calculated by observing the variations of the liquid height in the tube over a certain period. The pressure is calculated by observing the maximum liquid height difference between inlet and outlet tubes. The flow rate and pressure calculation are shown in Fig. 2.22(b).

The amplitude of the signal is first set to be 5V, and the frequency varies from 1 to 100Hz. The measured flow rate is shown in Fig. 2.23(a). The flow rate attains peaks of 32 μ L/min and 17 μ L/min at 10Hz when applying square and sinusoidal voltages respectively. In order to measure the maximum flow rate, the

signal type is fixed to the square type and the driving frequency is fixed at 10Hz. Fig. 2.23(b) shows the relationship between flow rate and input voltage. The pump attains a maximum flow rate of 50 $\mu\text{L}/\text{min}$ at a voltage amplitude of 8V.

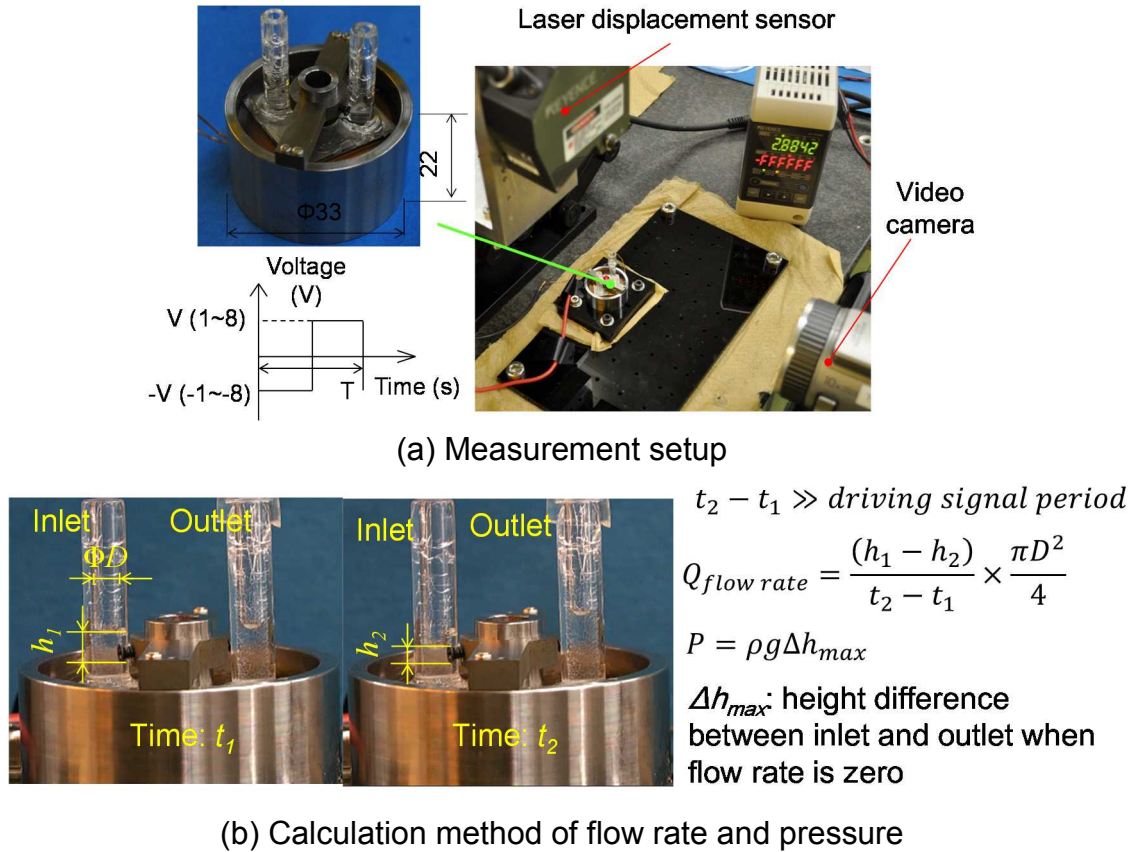


Fig. 2.22 Experimental setups for evaluating the pump performance

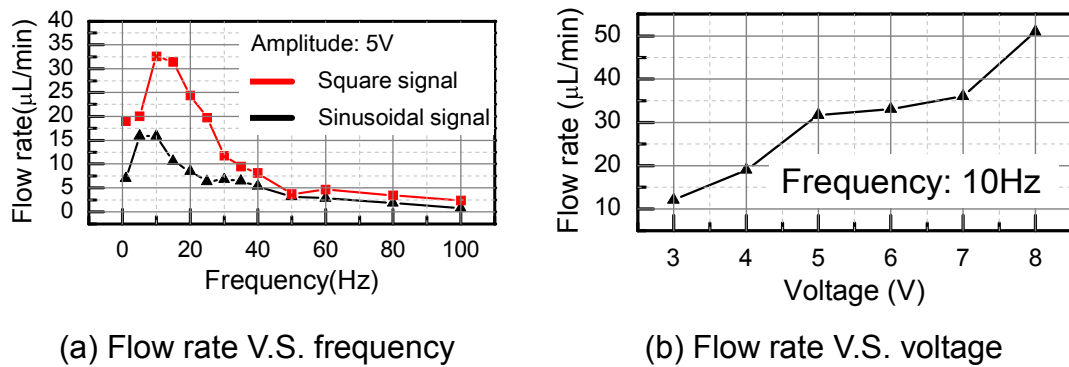


Fig. 2.23 Evaluation of pump flow rate

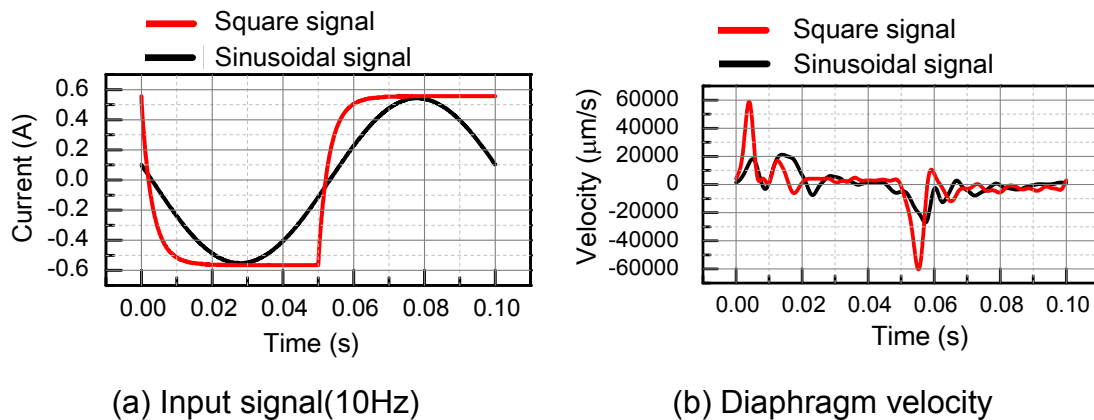


Fig. 2.24 Diaphragm velocities with different input signal

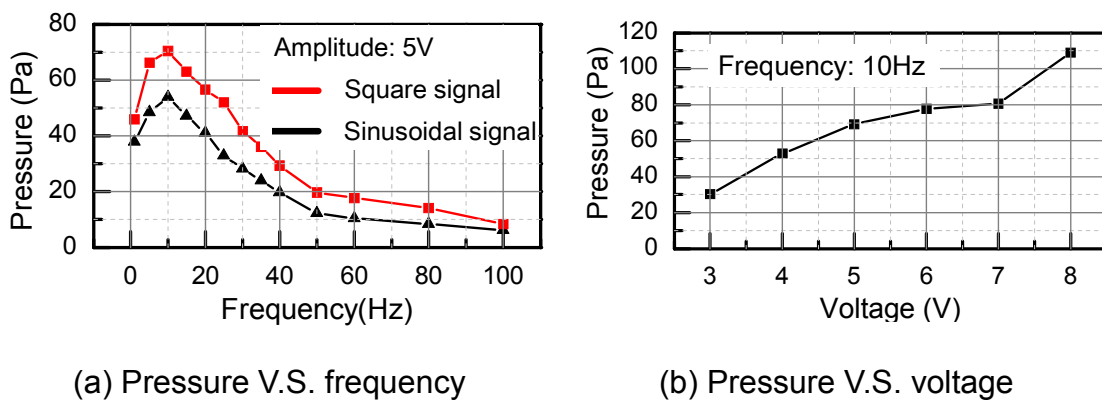


Fig. 2.25 Evaluation of pump pressure

The flow rate difference between two types of signals is due to the diaphragm velocity difference. Figure 2.24 shows the input signal profile and the diaphragm velocity at 10Hz frequency. The diaphragm velocity generated by square signal is double of that by the sinusoidal one. As a result, the flow rate are different.

The pressure of the pump is also evaluated in Fig. 2.25. It attains peaks of 70Pa and 55Pa when applying square and sinusoidal signal with 5V voltage and 10Hz frequency. In order to measure the maximum pressure, the signal type is fixed to the square type and the driving frequency is fixed at 10Hz. Fig. 2.25(b) shows the relationship between pressure and input voltage. The pump attains a maximum pressure of 110Pa when 8V voltage is applied. The pressure difference between two types of signal might be induced by the energy difference between

two signals.

2.5.3.2 Evaluation of bubble tolerant property

As the fabricated pump has a large diaphragm displacement, it can generate a large stroke volume. During the experiment, this pump is demonstrated to have the capability of bubble tolerance when it is driven by a square wave voltage with an amplitude of 8V at a frequency of 10Hz. According to [35], in order to realize bubble tolerance, the compression ratio ε should reach a minimum value of 0.07, ε is defined as the ratio between the stroke volume (V_{stroke}) and chamber volume ($V_{chamber}$), as shown in Fig. 2.26(a). For valveless pump, the criteria of bubble tolerance have not been experimentally measured. In this work, the diaphragm displacement is measured when the bubble tolerance phenomenon occurred, as shown in Fig. 2.26(b).

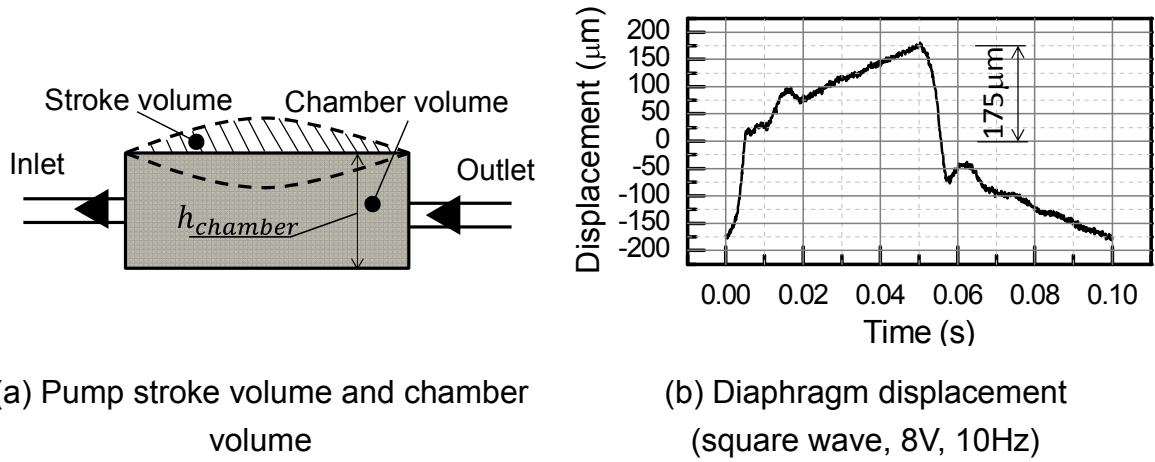


Fig. 2.26 Micro pump bubble tolerance evaluation

Fig. 2.27 shows a simplified model of the diaphragm displacement profile. The diaphragm displacement profile is assumed to be a circular truncated cone one. c is the radius of the TFPM, a is the radius of the diaphragm and d denotes the displacement of the diaphragm. The V_{stroke} and $V_{chamber}$ can be calculated by Eq. 2.3 and Eq. 2.4, in which $h_{chamber}$ is the height of chamber. The calculated compression ratio is about 0.188. This experimentally measured compression

ratio meets the required minimum value in theory [35]. Furthermore, it provides an experimental data for bubble tolerance property of diffuser valveless pump.

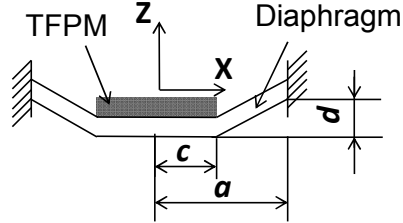


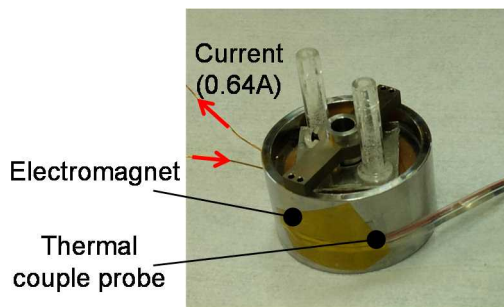
Fig. 2.27 Simplified model for diaphragm displacement profile

$$V_{stroke} = \pi c^2 d + \int_c^a 2\pi x d \frac{a-x}{a-c} dx \quad (2.3)$$

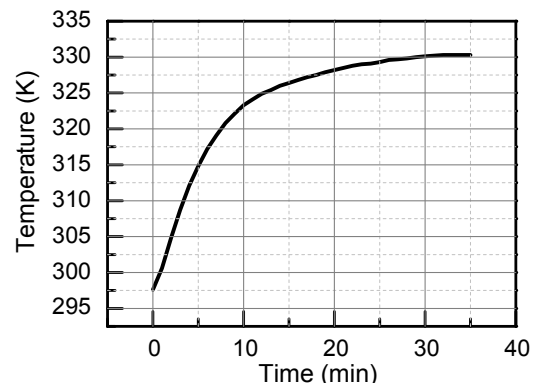
$$V_{chamber} = \pi a^2 h_{chamber} \quad (2.4)$$

2.5.3.3 Evaluation of temperature

During the pump working process, the voltage input into the coil is 8V and the current is around 0.64A. The temperature of the electromagnet is measured at this condition. The measurement setup and the result is shown in Fig. 2.28. The temperature is stabilized at 330K.



(a) Experimental setup



(b) Measured temperature

Fig. 2.28 Temperature measurement of the electromagnet

The temperature increase would increase the resistance of the coil. Thus it would decrease the current and degrade the actuator's force.

Furthermore, the high temperature of the electromagnet influences the pump efficiency. The viscosity of ethanol/water changes with temperature [65, 66]. And the viscosity would influence the pump efficiency by affecting Reynolds number and the “pressure-loss coefficient”, which are described in detail in [67]. Furthermore, the high temperature may change the property of the drugs when the pump is applied into drug delivery system.

2.6 Conclusion

2.6.1 Summary

In this chapter, a DEMA was realized utilizing a TFPM and an electromagnet with a closed magnetic circuit. The DEMA generated an electromagnetic force with a coefficient of 35.75mN/A and achieved a displacement of $\pm 500\mu\text{m}$.

The developed DEMA was then utilized to drive a diffuser valveless prototype pump successfully. The maximum flow rate of 50 $\mu\text{L}/\text{min}$ and maximum pressure of 110Pa were realized by applying a square wave voltage with a magnitude of 8V at a frequency of 10Hz. The large diaphragm displacement ($\pm 500\mu\text{m}$) enabled this pump to have bubble tolerance and self-priming. The temperature of the electromagnet reaches 330K when 8V constant voltage is input into the coil.

2.6.2 Remaining problems and future work

Several problems remain unsolved for the DEMA and prototype pump developed in this chapter. The problems are listed below.

- The first problem is the fabrication process of TFPM on PDMS diaphragm. TFPM is first sputtered on the Nb substrate, followed by cutting using scissors. Finally, the substrate is bond with PDMS diaphragm. The

fabrication process is shown in Fig. 2.29. This process, however, is not suitable for batch fabrication and miniaturization due to the using of scissors and the remaining of Nb. This problem will be solved in Chapter 3.

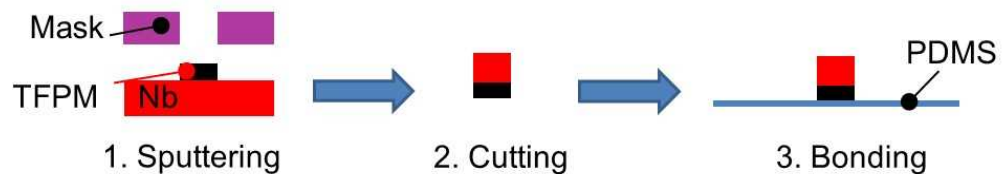


Fig. 2.29 TFPM fabrication process on PDMS

- The second problem is that the fabricated electromagnet has large size, which is not suitable for MEMS process and portable application. This problem will be solved in Chapter 4 by designing a planar type micro electromagnetic actuator.
- The third problem is that the fabricated pump has large size and is not flexible, which is not convenient for portable application in drug delivery systems. This problem will also be solved in Chapter 4.

In the future work, the viscosity variation on the pump's fluidic performance should be considered in simulation. Furthermore, cooling system should be developed to stabilize the temperature at the desired value.

Chapter 3 MEMS process integration of TFPM with flexible diaphragm

3.1 Introduction

3.1.1 Background of this chapter

As mentioned in Chapter 2, the TFPM fabrication process with PDMS was not compatible with batch fabrication. Furthermore, the Nb substrate for TFPM sputtering remained. It was difficult to remove Nb material without damaging TFPM.

3.1.2 Objective of this chapter

The objective of this chapter is to develop and evaluate a batch fabrication process that can integrate TFPM with PDMS material.

3.1.3 Solution

To solve the described problem, suitable sacrificial layer is selected for TFPM sputtering. After that, the sacrificial layer is etched without damaging other material and structure.

3.2 Proposal of fabrication process for TFPM integration with PDMS diaphragm

3.2.1 Proposed process

The process shown in Fig. 3.1 is proposed for fabricating the diaphragm consisting of TFPM on PDMS. A Si substrate is selected in the first step. Following that, TFPM is sputtered on the Si through a hard mask made of Ti and magnetized. PDMS is then coated on the surface. Finally, Si is etched by XeF_2 gas.

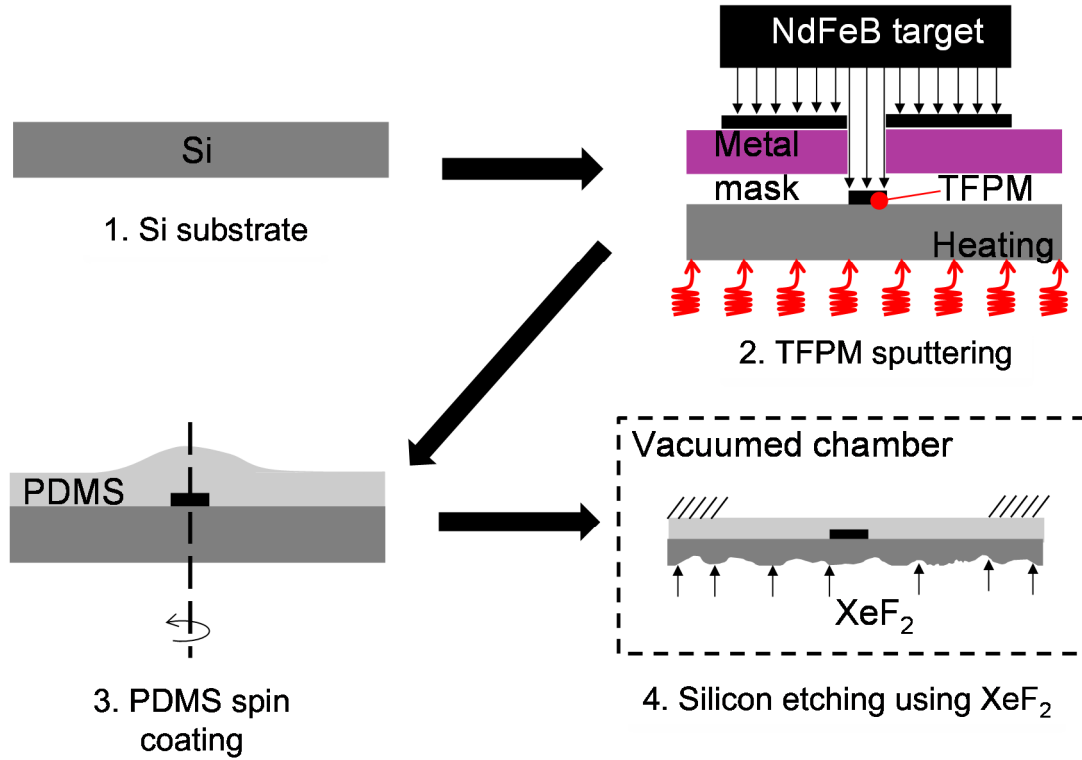


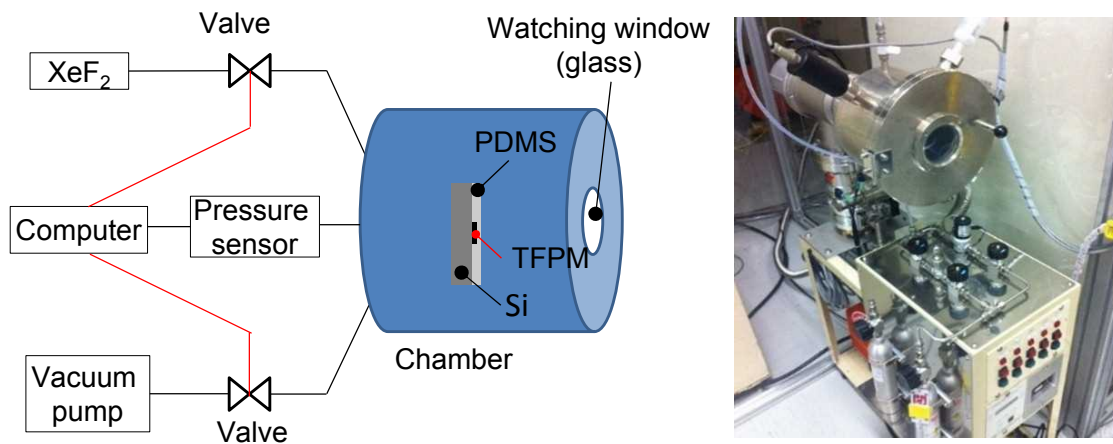
Fig. 3.1 Proposed fabrication process

Si is specially chosen for the substrate because there is little residual deformation and diffusion between TFPM and Si during sputtering process [36]. To etch Si, many candidate solutions are tested. Wet etching of Si using KOH or TMAH damages TFPM and detaches TFPM from PDMS. Dry etching of Si using reactive or non-reactive ion etching process is difficult to control etching stop. XeF₂ gas phase dry etching process is finally selected. The main reaction equation between XeF₂ and Si is shown in Eq. 3.1. There is no chemical reaction between XeF₂ and TFPM [36]. Furthermore, no reaction between XeF₂ and PDMS is reported [37].

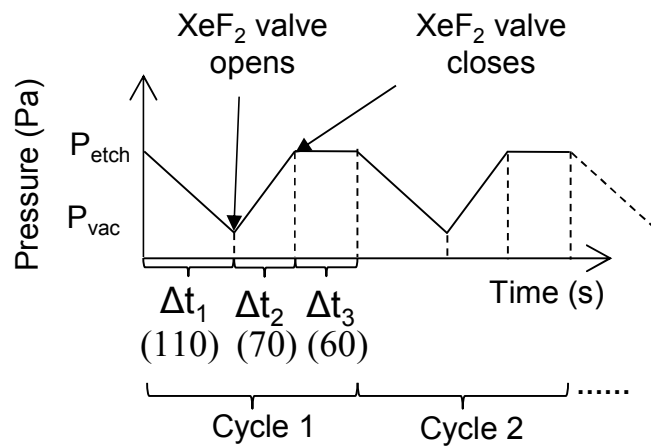


The schematic and experimental setup for XeF₂ dry etching are illustrated in Figs. 3.2(a, b). A solenoid valve fills and evacuates the chamber with XeF₂ by

detecting the signal from a pressure sensor connected to the chamber. Figure 3.2(c) shows the relationship between etching pressure and etching time during one etching cycle. When the chamber pressure reaches P_{vac} , the XeF_2 valve opens. When the chamber pressure attains P_{etch} , the XeF_2 valve closes. The reaction then keeps for some time and the chamber pressure slightly increases above P_{etch} . Finally, the chamber is vacuumed to P_{vac} again. The above process is one complete cycle. It is then repeated for some cycles until Si is fully removed.



(a) Schematic setup

(b) XeF_2 etching machine(c) Process of XeF_2 etchingFig. 3.2 Si etching using XeF_2

3.2.2 Fabrication

The process parameters are illustrated in Fig. 3.3. The detailed ones are

described in the following contents.

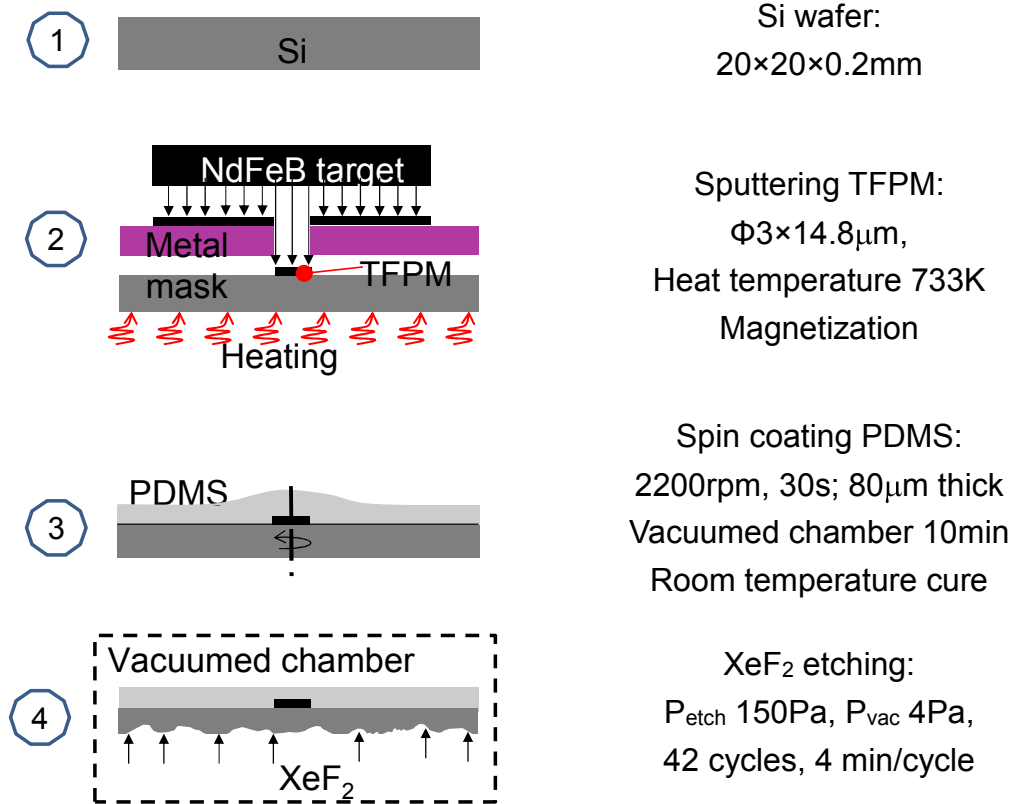


Fig. 3.3 Process parameters

Step 1: A 20mm×20mm square, 200μm thick Si substrate is prepared.

Step 2: A 14.8μm thick, 3mm diameter TFPM, consisting of 300nm thick NdFeB and 10nm thick Ta layers deposited sequentially, is sputtered onto the Si substrate through a Ti hard mask and magnetized in the vertical direction. The substrate temperature maintains 733K during sputtering. The sputtering parameters are the same as in Table 2.2.

Step 3: An 80μm thick PDMS is spin-coated onto the Si and the TFPM surface. The substrate is then placed in a vacuum chamber for 10 minutes to remove bubbles and cured at room temperature for 24 hours. Figure 3.4 shows the substrate after Step 3.

Step 4: The Si substrate is etched in XeF_2 gas. P_{vac} is 4 Pa and P_{etch} is 150Pa. The etching process consists of 42 repeated cycles. The average time for the etching process denoted in Fig. 3.2(c) (evacuation time Δt_1 , filling time Δt_2 and holding time Δt_3) are 110s, 70s and 60s, respectively. The average etching rate is $1.2\mu\text{m}/\text{min}$.

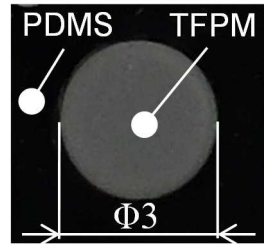
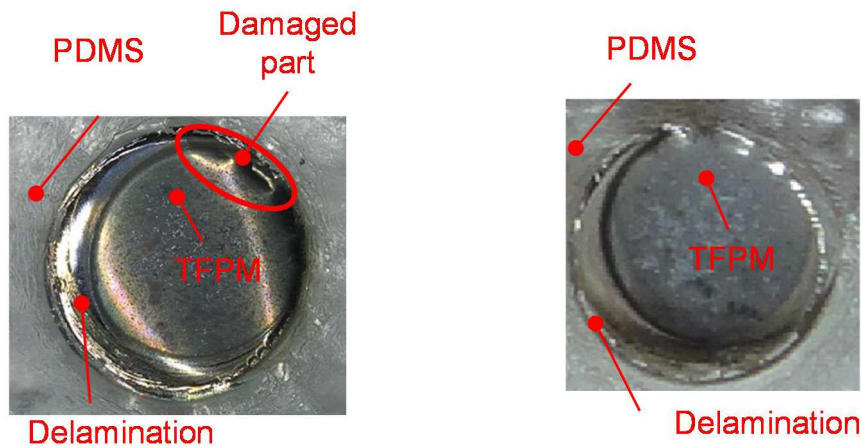


Fig. 3.4 Substrate before XeF_2 etching

Table 3.1 Thermal properties of the materials

Material	Heat conductivity [W/(m·K)]	Specific heat capacity [J/(kg·K)]	Thermal expansion coefficient [$10^{-6}/\text{K}$]
NdFeB	9	500	-4.8 (perpendicular to magnetization)
PDMS	0.18	1180	310
Si	130	705	2.9

PDMS, TFPM and Si have different thermal expansion coefficients, which are compared in Table 3.1. The thermal effect in this process has a large influence on the fabrication result. Figure 3.5 shows the fabricated magnetic diaphragms at different PDMS curing temperatures. The standard curing temperature of 343K and curing time of 30 minutes for PDMS generate small cracks on the upper right side of the TFPM. By modifying the curing temperature to 298K and extending the curing time to 24 hours, the damage on the TFPM can be avoided as a result of the reduced internal stress in the PDMS.



(a) PDMS cured at 343K
(Curing time 30min)

(b) PDMS cured at 298K
(Curing time 24h)

Fig. 3.5 Fabricated magnetic diaphragm after XeF_2 etching

However, in both samples shown in Fig. 3.5, parts of the TFPMs detach from the PDMS diaphragm. The delamination is caused by the reaction heat in the XeF_2 etching process which will be evaluated in the following section.

3.3 Evaluation of the flexible diaphragm with TFPM

3.3.1 TFPM magnetic property evaluation

In order to evaluate the magnetic properties of the TFPM before and after XeF_2 etching, the J-H curve of the TFPM is measured using a vibrating sample magnetometer (VSM). The second quadrant of the J-H curves are shown in Fig. 3.6.

After sputtering and magnetization, the TFPM has a B_r of 1.44 T and a H_c of 1.36 MA/m. However, after XeF_2 gas etching, the B_r decreases to 1.06 T. After re-magnetization process, the magnetic curve recovers. The decrease of magnetization might be caused by the heat generated during the XeF_2 etching process. An evaluation of the substrate temperature during the XeF_2 etching

process is given in Section 3.3.3.

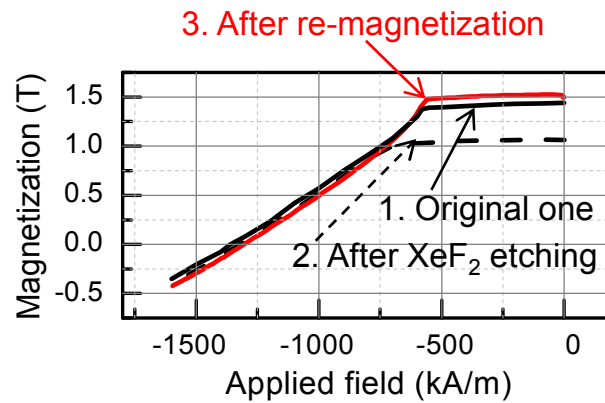


Fig. 3.6 J-H curve of the TFPM

3.3.2 PDMS mechanical property evaluation

In order to evaluate the mechanical properties of PDMS diaphragm after XeF₂ gas etching, force-displacement curve of the diaphragm is experimentally measured. The measurement setup is shown in Fig. 3.7. The magnetic diaphragm fabricated in Fig. 3.5(b) is sandwiched between two acrylic plates with 7mm diameter holes at their centers. The permanent magnet is re-magnetized. Uncured PDMS is used to bond the diaphragm with acrylic plates. The force on TFPM is generated using the electromagnet developed in Chapter 2. The diaphragm displacement is measured by the laser displacement sensor.

The current-displacement curve is experimentally measured, as shown in Fig. 3.8(a). The relationship between the force on TFPM and the current input into electromagnet is linear, with a simulated value of 37.8mN/A. The current-displacement curve is converted to force-displacement curve, indicated as the solid line in Fig. 3.8(b).

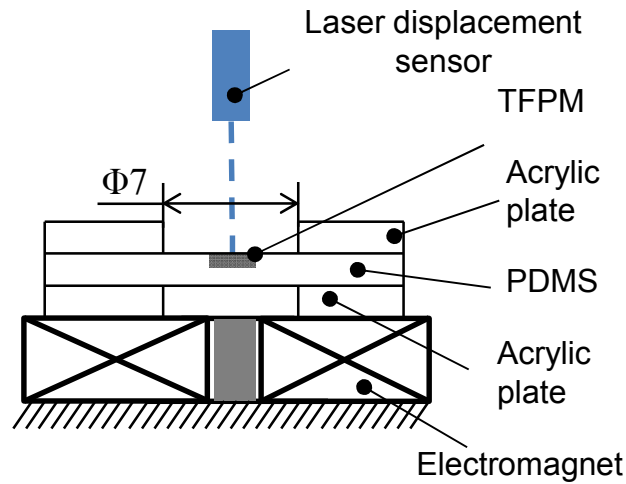


Fig. 3.7 Diaphragm displacement measurement setup

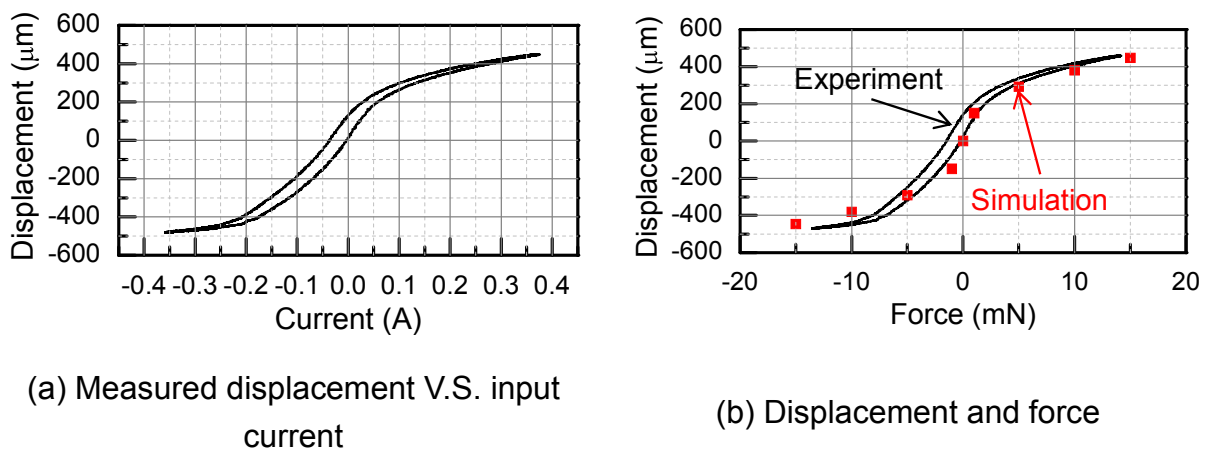


Fig. 3.8 Measured and simulated diaphragm displacement

The force-displacement curve is also simulated. In the simulation model, the edge of PDMS film is clamped and a uniform pressure is distributed in the central circular area, as shown in Fig. 3.9. Different from the model in Chapter 2, TFPM in Fig. 3.9 is inserted into PDMS diaphragm. The simulated result is compared with the experimental one in Fig. 3.8(b), which shows that there is good agreement between simulation and experiment. It demonstrates that the Young's modulus of 2MPa and Poisson's ratio of 0.45 for PDMS used in the simulation are the same as conventional values [31, 32]. It can be concluded that PDMS

retains its mechanical properties after XeF₂ gas etching.

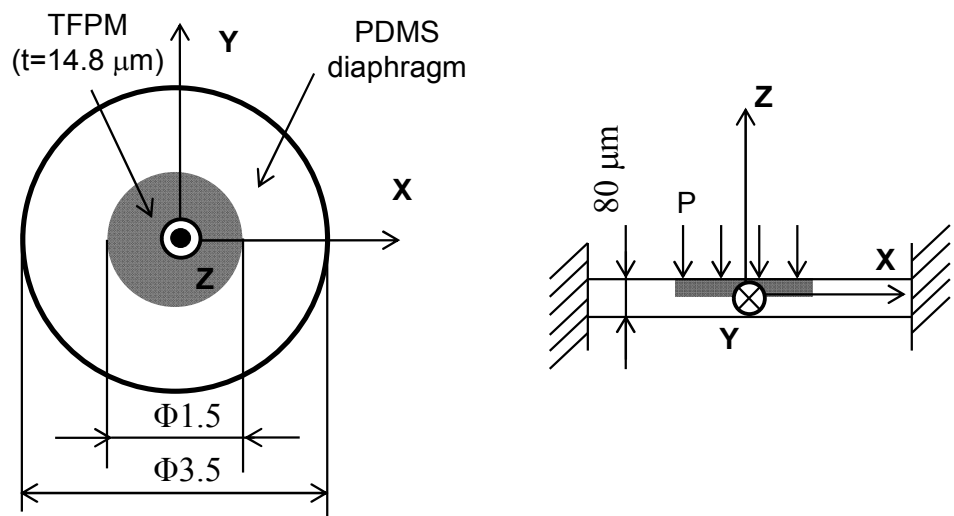
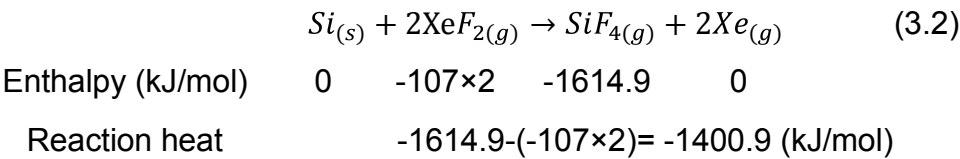


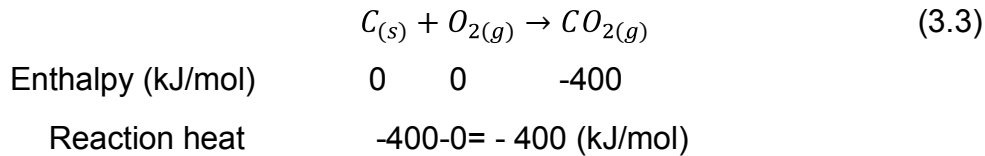
Fig. 3.9 Displacement simulation model

3.3.3 Reaction temperature evaluation

The exothermic reaction between Si and XeF₂ generates 1400kJ/mol heat from enthalpy aspect, as shown in Eq. 3.2. The reaction heat generation is a relatively high value compared with charcoal burning process, which is only 400kJ/mol, shown in Eq. 3.3.

The heat can substantially increase the temperature of the TFPM as well as the PDMS. Temperature measurement of the Si during XeF₂ etching was firstly demonstrated by F. I. Chang [38] using polysilicon piezoresistors fabricated on Si surface through a complex process. The relationship between the temperature and etching pressure was not discussed. Furthermore, the geometry of the substrate was not clear to calculate the reaction heat precisely.





Since the etching process is performed in a vacuumed chamber filled with XeF_2 gas, as shown in Fig. 3.2(a), a non-contact infrared thermometer setup is proposed to measure the temperature across the watching window made of glass. Figure 3.10(a) shows the transmission spectrum of glass [39]. Infrared wave with a wavelength over $5\mu m$ cannot penetrate the glass window. To measure the substrate temperature through the glass window, an infrared thermometer with a detecting wavelength between $1.95\mu m$ and $2.5\mu m$ (FTK9S-R80A-10S61, Japan Sensor Corp.) is adopted. The specifications of the infrared thermometer are shown in Table. 3.2.

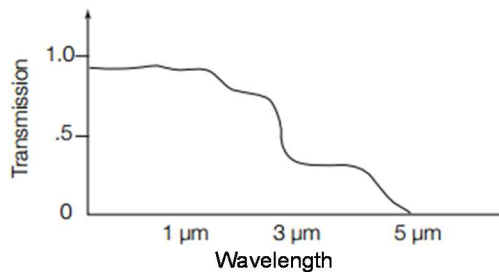
Table 3.2 Specifications of the infrared thermometer

Measurement range	353K ~ 693K
Wavelength	$1.95\mu m \sim 2.5\mu m$
Response time	0.8s
Standard distance (From the probe to the target)	100mm
Minimum target size (At standard distance)	$\Phi 9mm$
Temperature resolution	0.1K

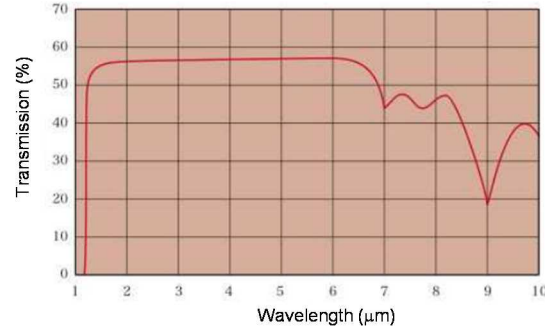
In Fig. 3.2(a), Si substrate with TFPM and PDMS (Si-TFPM-PDMS) is utilized. To measure the temperature, TFPM can be neglected from Si-TFPM-PDMS because the size of TFPM is $\Phi 3mm \times 14.8\mu m$. It is very small compared with Si substrate with the size of $20mm \times 20mm \times 200\mu m$.

Infrared wave with wavelength from $1.95\mu m$ to $2.5\mu m$ can penetrate Si, PDMS as well as glass. The transmission spectrum for Si is shown in Fig. 3.10(b) [40]. Si is “transparent” when the infrared wavelength ranges from $1.5\mu m$ to $5\mu m$. PDMS is also “transparent” in this wavelength range [69]. In this way, the

temperature measured is not pure “Si temperature”, but the temperature of other object, such as the chamber wall. Direct measurement of Si temperature using the infrared thermometer in Table 3.2 is not possible.



(a) Glass [39]



(b) Si [40]

Fig. 3.10 Transmission spectrum for glass and Si

To measure the temperature of Si substrate, the PDMS is replaced by a 10 μm thick blackbody spray (JSC3, Japan Sensor Corp.). The emissivity of blackbody spray in relationship with wavelength is shown in Fig. 3.11 [61]. The emissivity of blackbody spray reaches 0.94 when the wavelength ranges from 1 μm to 14 μm . It demonstrates that the blackbody spray can radiate almost all energy that it has absorbed. Furthermore, blackbody spray does not react with XeF_2 gas.

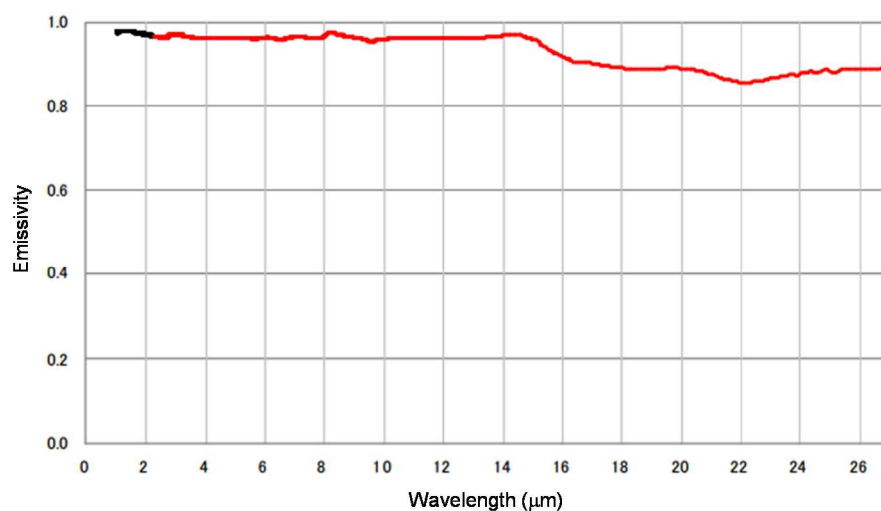


Fig. 3.11 Emissivity of blackbody spray [61]

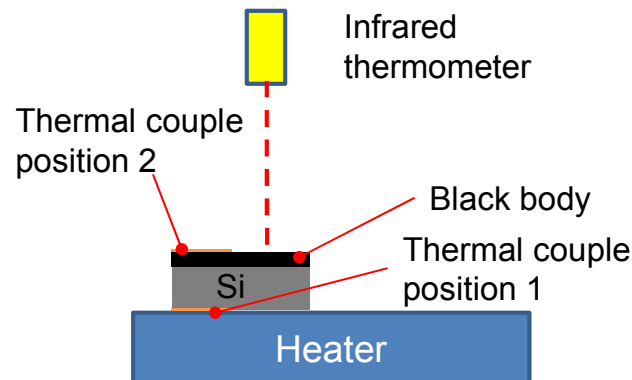


Fig. 3.12 Evaluating the temperature on Si and blackbody

The Si substrate is $200\mu\text{m}$ thick, while the blackbody spray on Si is $10\mu\text{m}$ thick. The temperature measured is from “blackbody spray” but not from “Si”. In order to verify whether the temperature at the two places are the same, a thermal couple is utilized to evaluate the feasibility. Fig. 3.12 shows the experimental setup. The infrared thermometer measures the temperature of the blackbody with an emissivity setting of 0.94. The heater gradually warms up the substrate from 350K to 470K. Thermal couple is placed on two positions separately. The first position is the surface of Si. The other position is the surface of the blackbody spray.

The measurement results in Fig. 3.13 clearly show that the temperature of Si and that of blackbody are very close in the range of 370K to 450K. The maximum error is within 3K. Thus, it is feasible to use the blackbody spray and the infrared thermometer.

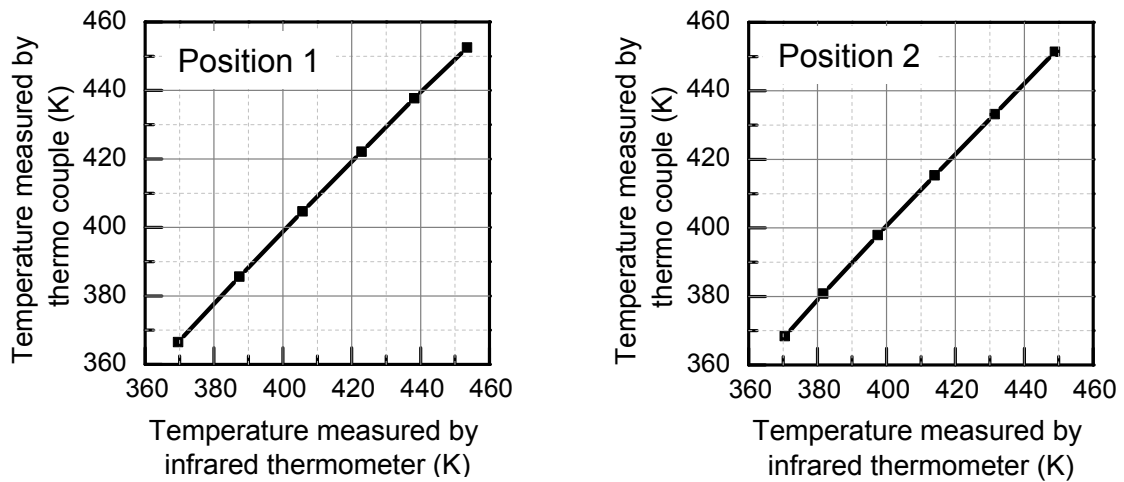


Fig. 3.13 Comparison of Si temperature and blackbody spray temperature

To measure the temperature across the glass watching window using the infrared thermometer, calibration is performed. The glass is disassembled from the XeF_2 etching chamber and is placed between the infrared thermometer and the substrate. The calibration setup is shown in Fig. 3.14(a), a thermal couple measures the temperature as a reference temperature. Due to the infrared wave's energy loss after penetrating the glass, the emissivity setting for the infrared thermometer is changed from 0.94 to 0.7. The calibration result is shown in Fig. 3.14(b). The temperatures measured by the infrared thermometer and thermal couple coincide well with a maximum error less than 10K.

The experimental setup to measure the temperature during XeF_2 etching process is shown in Fig. 3.15. The distance between the infrared thermometer and the blackbody spray is 100mm.

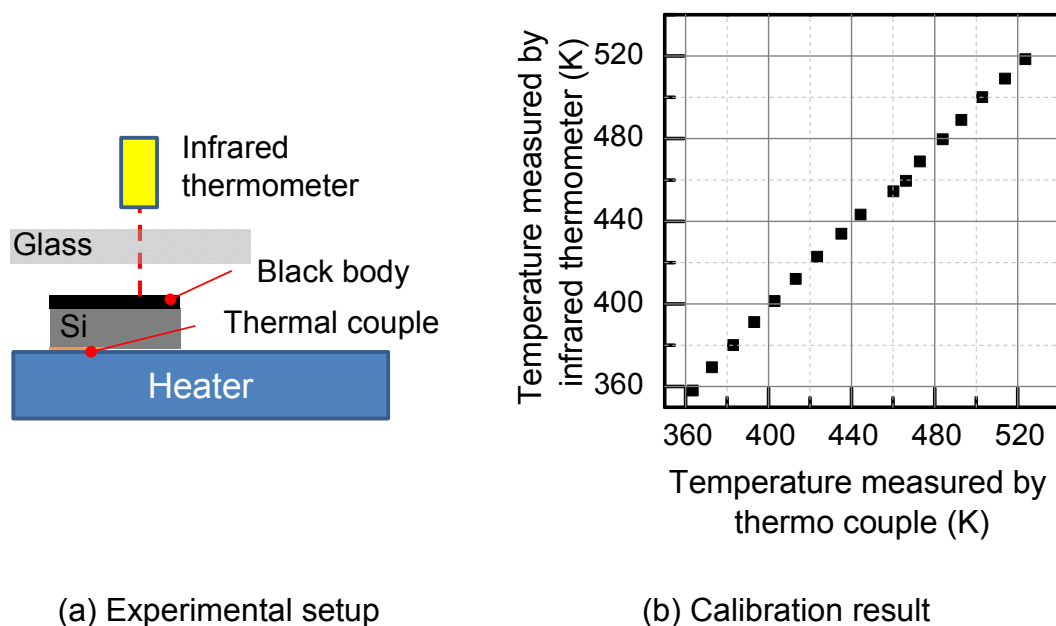


Fig. 3.14 Calibration method of the emissivity
(Placing the glass between the sample and infrared thermometer)

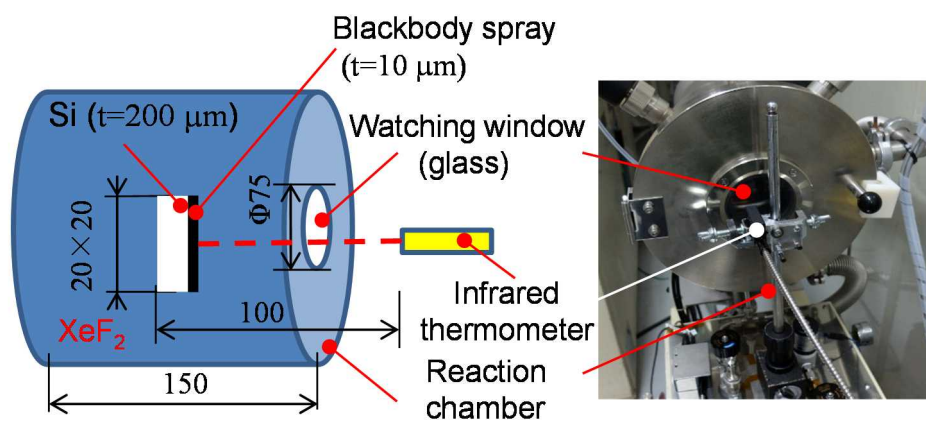


Fig. 3.15 Temperature measurement setup

The temperature measured during the etching process is shown in Fig. 3.16. In the case of 150Pa etching pressure, the substrate temperature increases when XeF_2 valve is open, and reaches a peak of 453K within 60s. The temperature drops when XeF_2 valve is closed.

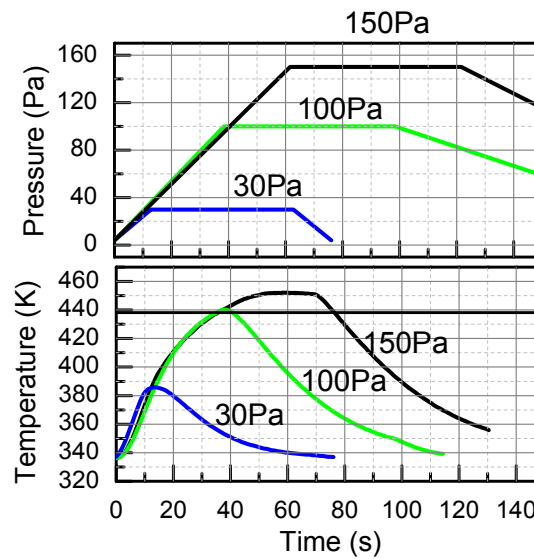


Fig. 3.16 Si temperature and pressure during the etching process

The maximum temperature of 450 K during the process is responsible for the degradation in the magnetic property of TFPM, which was discussed in Section 3.3.1. Heat resistance of TFPM is the temperature at which irreversible magnetic flux density loss reaches -5%, which was described in Section 2.3.1. Since TFPM's heat resistance and Curie temperature are 438K and 583K respectively [17], the highest temperature of 450K during XeF_2 etching process degrades but not fully diminishes TFPM's magnetic property.

Meanwhile, the thermal expansion coefficient of PDMS is much different from that of TFPM, as shown in Table 3.1. Thus, the thermal stress generated during XeF_2 etching process detaches TFPM from PDMS diaphragm, which can explain the delamination phenomenon in Fig. 3.5.

Figure 3.17 shows the variation in the maximum substrate temperature with relationship of XeF_2 etching pressure. As the pressure decreases, the maximum temperature also decreases. When the process pressure is 80Pa, the maximum temperature drops below 430K, under which temperature the magnetic performance of TFPM remains unaffected.

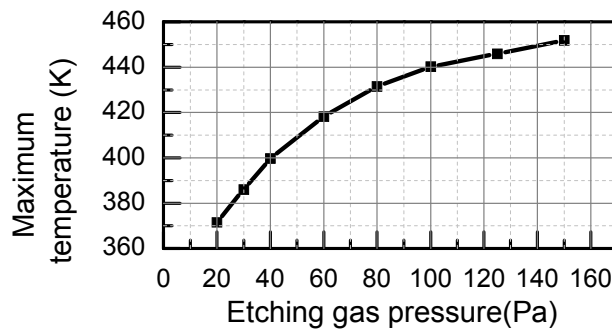


Fig. 3.17 Temperature dependence on maximum process pressure

3.3.4 Process optimization

According to the evaluation result in Section 3.3.1 and Section 3.3.2, TFPM recovered its magnetic performance after re-magnetization. Meanwhile, PDMS layer retained its mechanical performance. However, delamination of TFPM from PDMS layer gives rise to a shift of the effective center of the TFPM from the actual center. It will cause the misalignment of diaphragm applied to micro devices. Thus, this should be avoided during fabrication process.

As the delamination is caused by the high temperature (450K) during XeF_2 etching process, the XeF_2 etching pressure is decreased to reduce the process temperature. Figure 3.18 shows the modified XeF_2 etching parameters. The maximum etching pressure is decreased to 30Pa, and average process time for one cycle is modified to 100s. The average etching rate is $1.1\mu\text{m}/\text{min}$, which is almost the same with the one of 150Pa etching pressure.

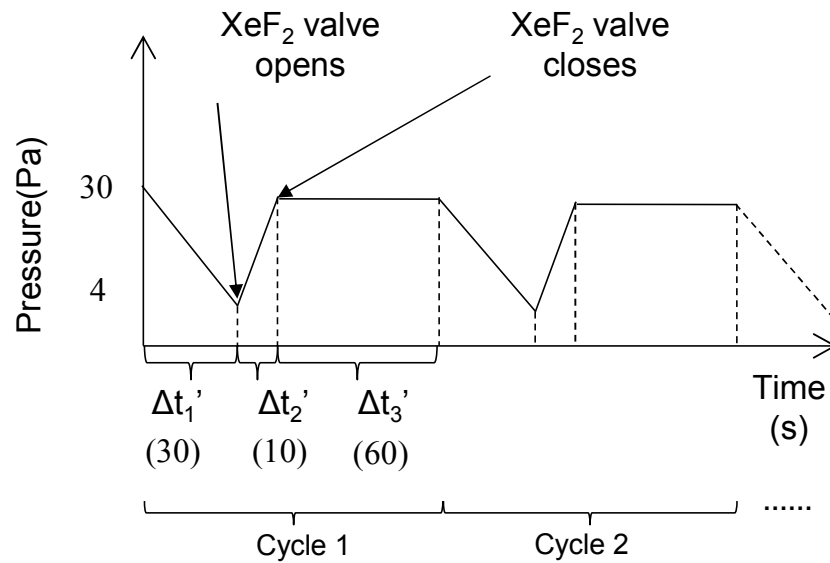
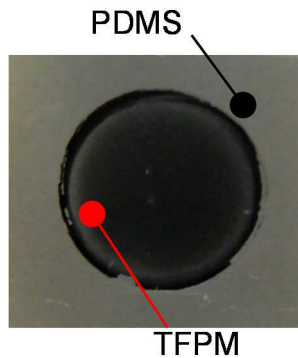


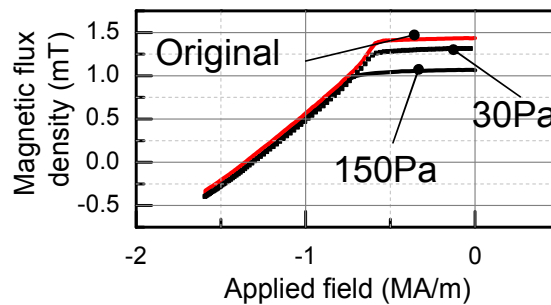
Fig. 3.18 XeF₂ etching parameters with 30Pa etching pressure

The fabricated PDMS diaphragm with TFPM using the optimized process parameters is shown in Fig. 3.19(a). TFPM remains attached to the PDMS diaphragm and there is no observable delamination. Furthermore, J-H curve of TFPM is measured again and the measurement result is shown in Fig. 3.19(b). The J-H curve of TFPM fabricated in 30Pa etching pressure remains almost the same as the original J-H curve of TFPM.

The thermal expansion coefficient of TFPM and Si are different. After depositing TFPM on Si substrate, TFPM is suppressed in room temperature, and it will expand after removing Si. Owing to the low stiffness of PDMS, the expanding energy of TFPM is totally absorbed by PDMS diaphragm. There is no observable deformation of the fabricated diaphragm.



(a) Fabricated result



(b) Measured J-H curve

Fig. 3.19 Fabricated magnetic diaphragm with optimized process parameters

3.4 Conclusion

3.4.1 Summary

In conclusion, a MEMS fabrication process which enables the integration of a sputtered TFPM on a PDMS diaphragm is proposed. This process was compatible with batch fabrication. The thermal effects of XeF_2 etching process, the magnetic performance of TFPM as well as the mechanical properties of PDMS were evaluated. Temperature measurements revealed that the temperature of TFPM rose to 453K during XeF_2 etching process at an etching pressure of 150Pa. The reaction heat degraded TFPM's magnetic property and caused partial delamination of TFPM from PDMS layer. The substrate temperature with respect to XeF_2 etching pressure was experimentally measured by a calibrated infrared thermometer setup penetrating the glass window. Evaluation results showed that TFPM retained its magnetic properties with a re-magnetization process and PDMS maintained its mechanical properties. After optimization, achieved by changing the XeF_2 etching pressure to 30Pa, the fabricated magnetic diaphragm retained its shape and magnetic properties. The reaction rate of 150Pa and 30Pa etching pressure were almost the same.

3.4.2 Future work

In future work, the fabricated PDMS diaphragm integrated with TFPM can be applied to micro pumps. Furthermore, it is expected that the magnetic diaphragms will be applied to many other MEMS devices such as micro valves, energy harvesting devices and tactile display devices.

Chapter 4 Development of high force/energy density planar micro electromagnetic actuators and their applications to a flexible MEMS pump

4.1 Introduction

4.1.1 Background of this chapter

In Chapter 2, a DEMA was proposed and realized. It utilized an electromagnet with a closed magnetic circuit which is suitable for generating a large force and a large displacement. However, the large size electromagnet was used, which is difficult to be applied for MEMS devices. Meanwhile, although the DEMA developed in Chapter 2 successfully actuated a prototype pump, the pump was not applicable to flexible and delicate surfaces due to the large size of electromagnetic actuator as well as the hard pump body. In some applications such as the attachment of pump on human skin in drug delivery system, the hard pump body and large electromagnet cause the application inconvenient.

Some researchers have developed planar micro electromagnetic actuators which are integrated with MEMS fabrication process. Common configuration for these actuators is the planar micro permanent magnet driven by planar spiral micro-coil, which is illustrated in Fig. 4.1.

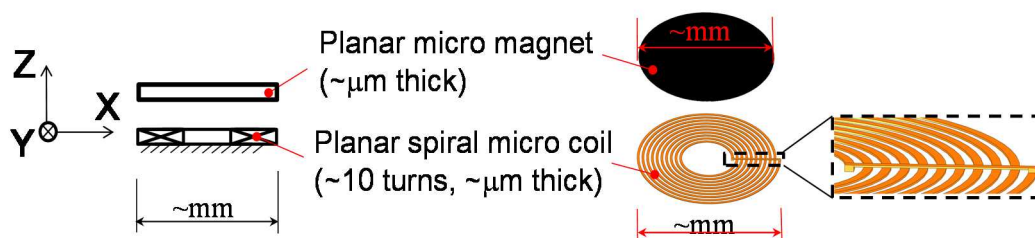
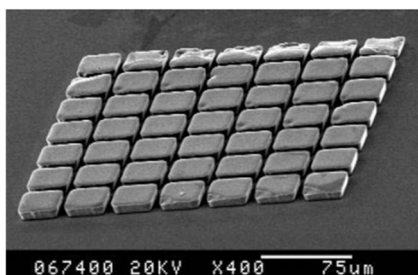


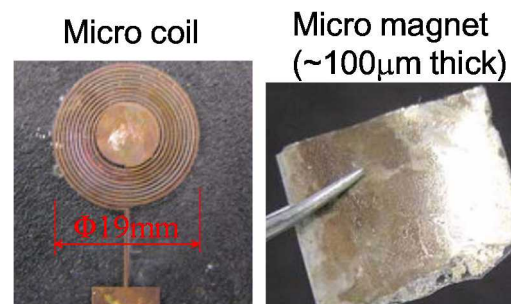
Fig. 4.1 Configuration of planar micro electromagnetic actuator

The generated force of such actuators, however, is fairly low. Su et al. [41] developed an actuator which is composed of an electroplated CoNiMnP permanent magnet array ($0.35\text{mm} \times 0.35\text{mm} \times 0.02\text{mm}$) and a micro-coil (7 turns), shown in Fig. 4.2(a), it generated $36\mu\text{N/A}$ force in simulation. C. Y. Lee et al. [42] realized an integrated micro actuator shown in Fig. 4.2(b), the force generated by the electroplated permanent magnet (3mm in diameter, $110\mu\text{m}$ thick) and micro-coil (20 turns, 19mm in diameter) was around $135\mu\text{N/A}$ in simulation. The integrated micro electromagnetic actuators are rarely utilized in cases requiring several mN order force. Force and energy density are defined to be force and energy divided by actuator's volume with unit current input into the coil [70, 71]. The actuator developed in [42] possessed $75\mu\text{N}/\text{mm}^3/\text{A}$ force density with energy density $4.23 \times 10^{-9} \text{J}/\text{mm}^3/\text{A}$.

Furthermore, the spiral micro-coil involves the central electrode connection, which is enlarged in Fig. 4.1. This Three-Dimensional (3D) structure requires the fabrication process of through holes electroplating [44] or resist insulation [45], thus complicating the fabrication.



(a) Permanent magnet pattern in [41]



(b) Planar micro electromagnetic actuator in [42]

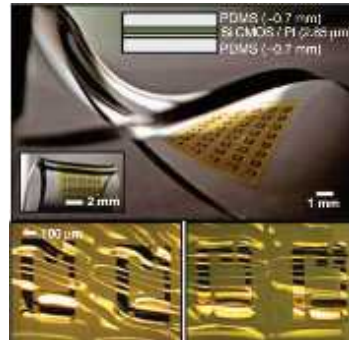
Fig. 4.2 Planar type electromagnetic actuator developed previously

Besides the scaling effect that electromagnetic interaction reduces as the actuator size scales down [10], there are still some reasons that degrade the performance of micro planar type electromagnetic actuator and limit its application. Firstly, film type permanent magnets fabricated using electroplating process are usually based on CoPt, FePt or CoNiMnP. As mentioned in Section 1.1.2, the H_c and B_r of these magnets are much inferior to those of the bulk NdFeB permanent magnets. Secondly, planar micro permanent magnets are several μm in thickness and several mm^2 in area. Due to the large self-demagnetization factor [46], the magnetic flux density distribution is much different from that of common bulk permanent magnet, which is illustrated in detail in Section 4.2. Thus the spiral micro-coil and planar micro permanent magnet are not efficiently designed.

Meanwhile, flexible electronic devices are recently popular in consumer product, wearable technologies and point of care testing field [54, 47, 48]. Fig. 4.3 shows the recent research and development of flexible devices. Rogers et al. [47] develops a variety of flexible and stretchable film type sensors based on Si, polymers and metals. Someya et al. [48] realizes ultra-thin and ultra-light electronic films that are potential for medical and consumer product application. The patterning of electronic circuit on flexible substrate is also achieved in commercial applications [49]. The pump chip body could become flexible using flexible material [9]. By combining the technologies above, it is possible to realize a flexible micro pump, which is very useful in point of care testing field or drug delivery systems.



(a) Flexible mobile phone developed by LG. Co. [54]



(b) Stretchable and foldable devices [47]



(c) Ultra-thin and flexible electronic circuit [48]

Fig. 4.3 Recent technologies for flexible electronic devices

4.1.2 Objectives of this chapter

The first objective of this chapter is to enhance the force of planar type micro electromagnetic actuators and simplify the micro-coil fabrication. The electromagnet proposed in this chapter should have the following features:

- MEME-based: the permanent magnet and the coil should be fabricated by fully MEMS-based process.
- Large force: the planar type actuator proposed in this chapter should generate mN order force to actuate pumps, tactile display devices and other MEMS devices.
- The micro-coil designed in this chapter should have 2D structure, which is easy to fabricate.

The second objective of this chapter is to utilize the planar type micro electromagnetic actuator and the technology developed in Chapter 3 to realize a MEMS pump. The pump should have the following features:

- Flexible, transparent and portable: the pump should have flexible pump

body that can be applied on curved and delicate surfaces such as human skin. Furthermore, the pump should be transparent for flow monitoring and particle detection.

- High performance, small size and batch fabrication: utilizing the developed electromagnetic actuator in this chapter, the pump should have small size and high performance compared with other electromagnetically actuated MEMS pumps. Furthermore, the pump should be fabricated by MEMS-based process.

4.1.3 Solutions

The solutions to enhance the force of planar type micro electromagnetic actuator are as follows. Firstly, high performance TFPM which has been described in Section 1.1.2 is utilized. Secondly, line/space and chessboard segmentations of TFPM are designed to reduce the self-demagnetization effect. The 2D meander type and mesh type micro-coils are also originally proposed in correspondence with the permanent magnet patterns. Thirdly, the actuator performance is further enhanced by covering a ferromagnetic layer on TFPM.

The solution for realizing flexible and portable MEMS pumps is to select flexible materials as pump body and combine the recently developed technologies with the MEMS pump.

4.2 Analysis and proposals of the planar micro electromagnetic actuators using TFPM

4.2.1 Characteristics of TFPM magnetic flux density

Magnetization M is a quantity that describes the degree to which permanent magnets are magnetized. It only exists within the permanent magnet. Magnetic poles are generated by M . Magnetic field H that is generated by magnetic poles begins from the N pole and ends at the S pole. Magnetic flux density field, also

known as B , is defined as the sum of M and H , illustrated in Eq. 4.1.

$$B = \mu_r \mu_0 (H + M) \quad (4.1)$$

Where μ_0 is the vacuum magnetic permeability in SI and μ_r is the ratio of the permeability of a specific medium to μ_0 . Figure 4.4 illustrates a block permanent magnet sample with M , H and B . It clearly shows that part of the H that is inside of the permanent magnet, radiating from N pole to S pole, demagnetizes magnetization. Since this field is generated by the permanent magnet itself, it is called self-demagnetization field H_d [46].

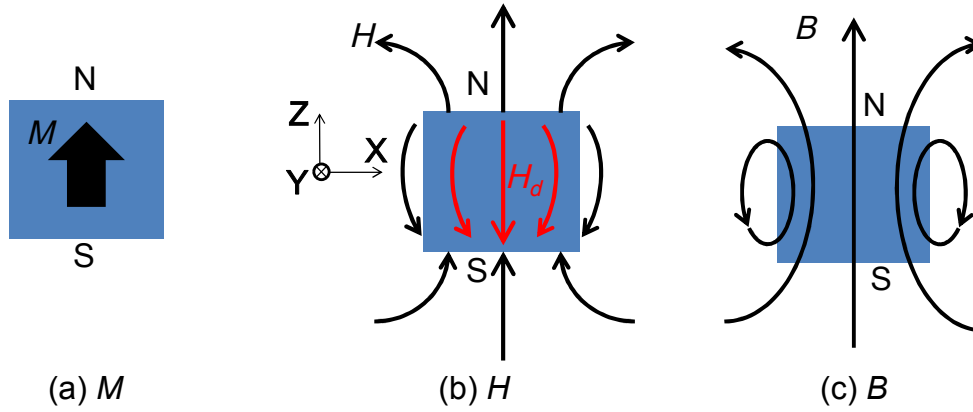


Fig. 4.4 M , H and B generated by a block permanent magnet

The direction of H_d is opposite to M . The magnitude of H_d is proportional to M with a factor of N_d . The relationship between M , H_d and N_d is expressed in Eq. 4.2. Where N_d is called self-demagnetization coefficient.

$$H_d = -N_d M \quad (4.2)$$

N_d can be calculated schematically in Fig. 4.5 and is expressed in Equation 4.3.

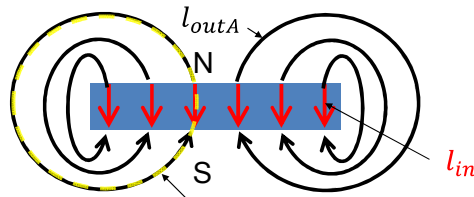
$$N_d = \frac{1}{1 + l_{in}/l_{out}} \quad (4.3)$$

Where l_{in} and l_{out} represent the lengths of H field inside and outside of the magnet. Equation 4.3 also indicates that the value of N_d is only related with the shape of permanent magnet. For a standard sphere or a cube, the self-

demagnetization coefficient is $1/3$ at X, Y and Z direction, respectively. Furthermore, as H_d is generated by M , the N_d of the permanent magnet does not exceed 1. By combining Eq. 4.1 and Eq. 4.2, the magnetic flux density inside the magnet can be expressed in Eq. 4.4.

$$B = \mu_0 \mu_r M (1 - N_d) \quad (4.4)$$

→ H field line outside the magnet H_{out} , line length l_{out}
 → H field line inside the magnet H_{in} , line length l_{in}



Selected closed path l in Ampere law

1. Ampere law $\oint_l \vec{H} \cdot d\vec{l} = I = 0$ (for magnet [46])
2. $l_{out}|H_{out}| - l_{in}|H_{in}| = 0 \Rightarrow |H_{out}/H_{in}| = l_{in}/l_{out}$
3. $-H_d = |H_{in}|$, $M = |H_{in}| + |H_{out}|$ [72]
4. $N_d = -\frac{H_d}{M} = \frac{|H_{in}|}{|H_{in}| + |H_{out}|} = \frac{1}{1 + |H_{out}/H_{in}|} = \frac{1}{1 + l_{in}/l_{out}}$

Fig. 4.5 Schematic calculation of N_d

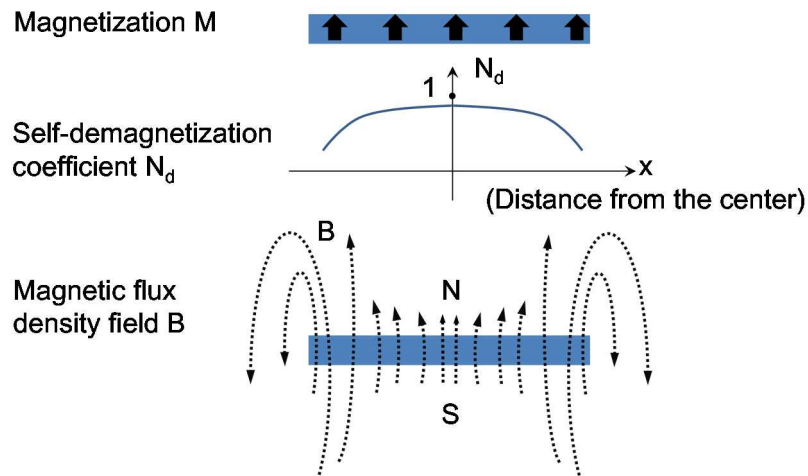


Fig. 4.6 B generated by a film type permanent magnet

From Eq. 4.4, the B is close to 0 as N_d reaches 1. Meanwhile, the N_d is close to 1 near the center of the TFPM, and it gradually decreases when the position is apart from the center, shown in Fig. 4.6 [46]. As a result, the edge of the film permanent magnet generates relatively stronger B than that in the center. The B distribution of TFPM is also shown in Fig. 4.6.

When TFPM is actuated by the micro-coil, the distribution of B generated by TFPM affects the performance of electromagnetic actuator. A simplified model is established to evaluate the electromagnetic force between TFPM and spiral coil. The model is shown in Fig. 4.7(a). The size of TFPM and the spiral coil are $5\text{mm} \times 5\text{mm} \times 0.02\text{mm}$ and $7.5\text{mm} \times 7.5\text{mm} \times 0.02\text{mm}$, respectively. The cross section of each coil turn is $0.05\text{mm} \times 0.05\text{mm}$. For simplicity, the spiral coil is modeled as a combination of square loops that have the same center but have different lengths as shown in Fig. 4.7(b). The current density input into each coil turn is 100A/mm^2 , and the gap between TFPM and coil is $10\mu\text{m}$. The force generated on each coil turn is then simulated.

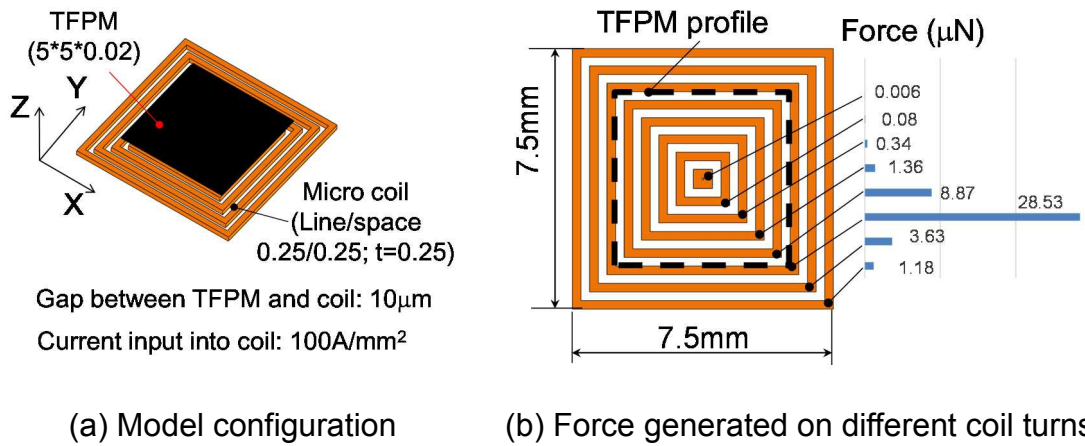


Fig. 4.7 Model for calculating TFPM interaction with different coil turns

The electromagnetic force distribution is shown in Fig. 4.7(b). The dashed line is the profile of TFPM and the column figure shows the force generated on each coil turn. It reveals that the coil turn closest to TFPM edge can generate the

maximum force while the coil turn which is far away from TFPM edge generates smaller force. The edge of TFPM contributes more to electromagnetic interaction. On the contrary, the center of the TFPM contributes less.

Besides the above analysis related with permanent magnet geometry, the magnetic core effect using ferromagnetic materials is also considered. The ferromagnetic material is widely utilized in industry such as transformers or solenoids. As the permeability of ferromagnetic material such as pure iron or permalloy is high [68], the magnetic resistance of magnetic core is small. Covering one side of the TFPM pattern with ferromagnetic layer can greatly enhance the magnetic flux density in the other side. Thus, it is predictable that the force generated by the actuator would increase due to the addition of ferromagnetic layer on TFPM.

Based on the analysis above, to enhance the performance of micro electromagnetic actuator, this chapter proposes the following two methods:

- TFPM is segmented to generate more “edges”.
- TFPM is covered with a ferromagnetic layer.

4.2.2 High performance planar micro electromagnetic actuators design

Three types of planar micro electromagnetic actuator are designed and compared. In all the actuators, the size of TFPM is designed to be $5\text{mm} \times 5\text{mm} \times 20\mu\text{m}$ and the outer size of the coil is the same as the TFPM.

A geometrical view of the actuator is shown in Fig. 4.8. The actuator consists of three parts, a micro-coil, a TFPM and a back yoke on TFPM. The gap between TFPM and micro-coil is within $200\mu\text{m}$. Plane 1 is located $100\mu\text{m}$ beneath TFPM surface. Plane A is the cross section of TFPM and back yoke.

Figure 4.9 shows the proposed designs of the electromagnetic actuators.

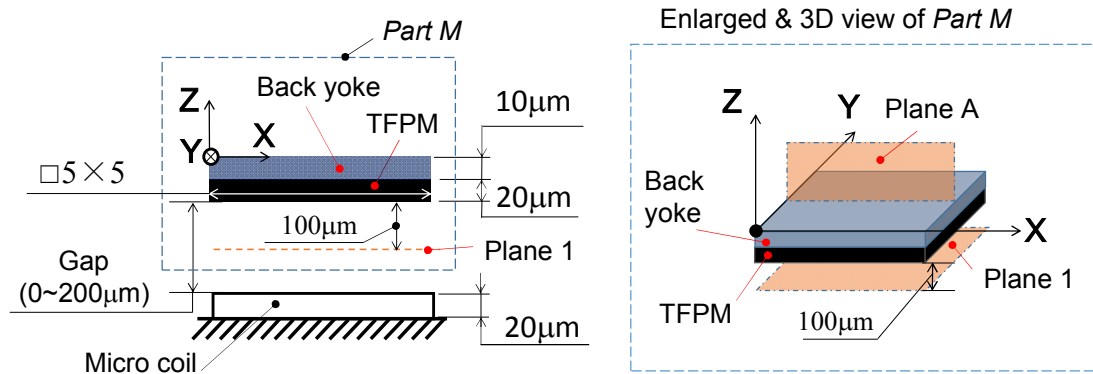


Fig. 4.8 Micro electromagnetic actuator configuration

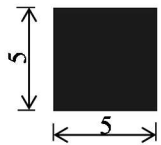
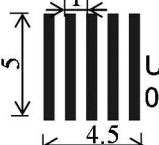
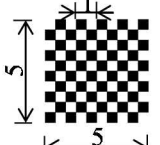
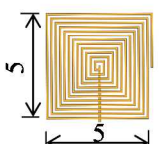
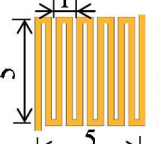
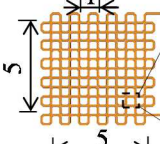
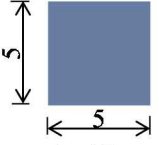
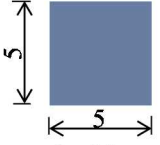
	Type 1	Type 2		Type 3	
		(1)	(2)	(1)	(2)
TFPM	 $t=20\mu\text{m}$	 $t=20\mu\text{m}$ Unit size $0.5 \times 5 \times 0.02$	 $t=20\mu\text{m}$ Unit size $0.5 \times 0.5 \times 0.02$		
Micro coil Current 1A	 $t=20\mu\text{m}$ Line/space $0.1/0.1$ 12 turns	 $t=20\mu\text{m}$ Line width 0.3	 $t=20\mu\text{m}$ Line width 0.3		
Back yoke	None	None	 $t=10\mu\text{m}$ Permalloy (Ni_{48})	None	 $t=10\mu\text{m}$ Permalloy (Ni_{48})

Fig. 4.9 Proposed electromagnetic actuators

Type 1 is a conventional configuration with a non-segmented permanent magnet and a spiral micro-coil, which is adopted in many micro electromagnetic actuators [42, 45].

In Type 2, TFPM is formed into a line/space configuration. The unit size of

permanent magnet is $0.5\text{mm} \times 5\text{mm} \times 20\mu\text{m}$. A micro-coil with a meandering shape is designed. Type 2 has two sub-types with and without back yoke made of permalloy. Permalloy consisting of Ni and Fe is specially chosen for two reasons. Firstly, it has high magnetic permeability, high magnetization saturation and stable chemical property. Secondly, it can be fabricated by electroplating process, which is compatible with MEMS process. On the other hand, although Fe possesses higher magnetic saturation (2.2T) than permalloy (0.6-2.2T) and Ni (0.6T), the deposition of pure Fe film using sputtering or physical evaporation would introduce thermal stress. And the deposition rate is lower than electroplating. Furthermore, pure Fe film is very sensitive to the environment, it will easily be oxidized in humidity atmosphere.

The magnetic flux density saturation of permalloy with the relationship of Ni weight percentage is shown in Fig. 4.10 [51]. When Ni percentage is less than 25%, the magnetic saturation is over 2T. Increasing Ni percentage to 30%, the magnetic saturation decreases to less than 0.4T. Furthermore, when Ni percentage attains 50%, the magnetic saturation reaches a peak of 1.6T. The realization of high Fe content over 80% is difficult using electroplating. Considering the fabrication difficulty, the permalloy material is designed to be Ni_{48} , which is a common industrial permalloy. The Ni_{48} permalloy is reported to possess a magnetic flux density saturation of 1.2T [52].

In Type 3, the permanent magnet has a chessboard pattern. A mesh shape micro-coil is also designed considering the TFPM pattern. Type 3 has two sub-types with and without back yoke made of permalloy. The chessboard pattern has a unit size of $0.5\text{mm} \times 0.5\text{mm} \times 20\mu\text{m}$.

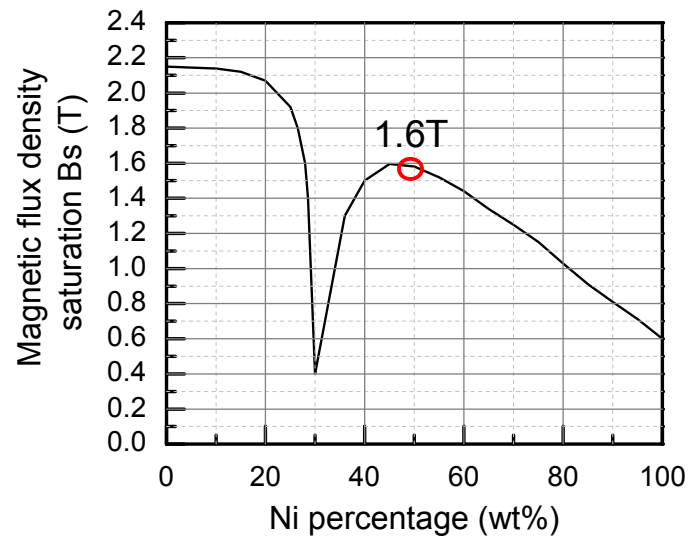


Fig. 4.10 Magnetic flux density saturation V.S. Ni percentage

4.2.3 Magnetic field Simulation

4.2.3.1 Magnetic flux density simulation and N_d calculation

The B generated by the TFPMs on Plane 1 and Plane A are simulated in Fig. 4.11. The dot line represents TFPM's cross section.

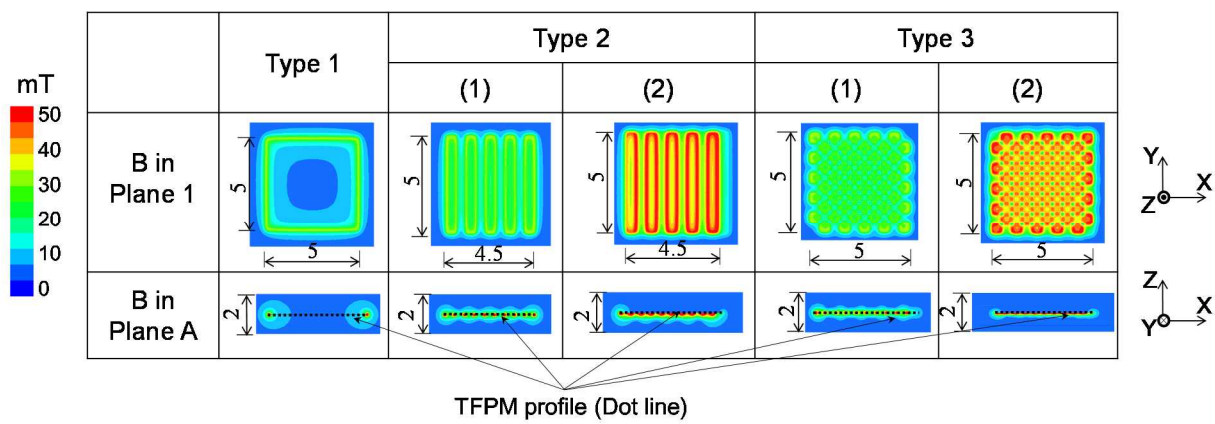
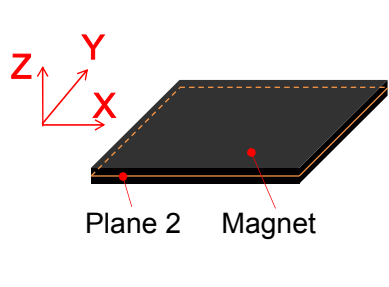


Fig. 4.11 Magnetic flux density distribution
(The Plane 1 and Plane A are defined in Fig. 4.8)

In Type 1, the magnitude of B is maximum around 30mT at the edges and near zero in the center. In Types 2(1) and 3(1), the magnitudes of the B in the

center part are enhanced. Furthermore, due to the smaller unit size, the chessboard pattern possesses more “edges” than the line/space pattern, thus generating a stronger B . In Type 2(2) and 3(2), the magnitudes of B in Plane 1 attain 50mT.

Furthermore, the N_d of TFPM with and without segmentation are calculated, respectively. The calculation method is shown in Fig. 4.12. Plane 2 is the center plane of TFPM in Z direction. As TFPM is very thin, the average H_d can be calculated by firstly integrating the H field on Plane 2. It is then divided by the area of Plane 2. The N_d of Type 1, Type 2(1) and Type 3(1) are 0.985, 0.940 and 0.906, respectively.



$$N_d = \frac{H_d}{M} \quad H_d \approx \frac{\int_{Plane\ 2} H dS}{\int_{Plane\ 2} dS}$$

$$M = B_r / \mu_0 \mu_r$$

B_r : Magnetic remanence
 μ_r : Relative magnetic permeability
 μ_0 : Magnetic permeability in vacuum

Fig. 4.12 Calculation method of self-demagnetization factor

4.2.3.2 Electromagnetic force analysis

The simulated electromagnetic forces generated by the proposed actuators are compared in Fig. 4.13. The current input into each coil is 1A. Type 1 can generate electromagnetic force around 400 μ N when the gap between TFPM and micro-coil is less than 200 μ m. Moreover, Type 1 is not sensitive to the gap.

Compared with Type 1, Type 2(1) and Type 3(1) can generate several times larger electromagnetic forces. When the gap is 20 μ m, the forces generated by Type 2(1) and Type 3(1) are 1500 μ N and 4500 μ N, respectively. However, when the gap increases from 20 μ m to 200 μ m, the electromagnetic forces decrease to 400 μ N. It can be predicted that when the gap is over 200 μ m. The forces

generated by Type 2(1) and Type 3(1) actuator are smaller than that of Type 1.

Types 2(2) and Type 3(2) have larger force magnitude compared with Type 2(1) and Type 3(1) due to the ferromagnetic layer effect. The electromagnetic forces are around 80% higher. The electromagnetic force of the order of several mN can be realized. Type 2(2) and Type 3(2) are also dependent on the gap. Considering the force target of mN order, it is better to utilize these actuators within 200 μm gap.

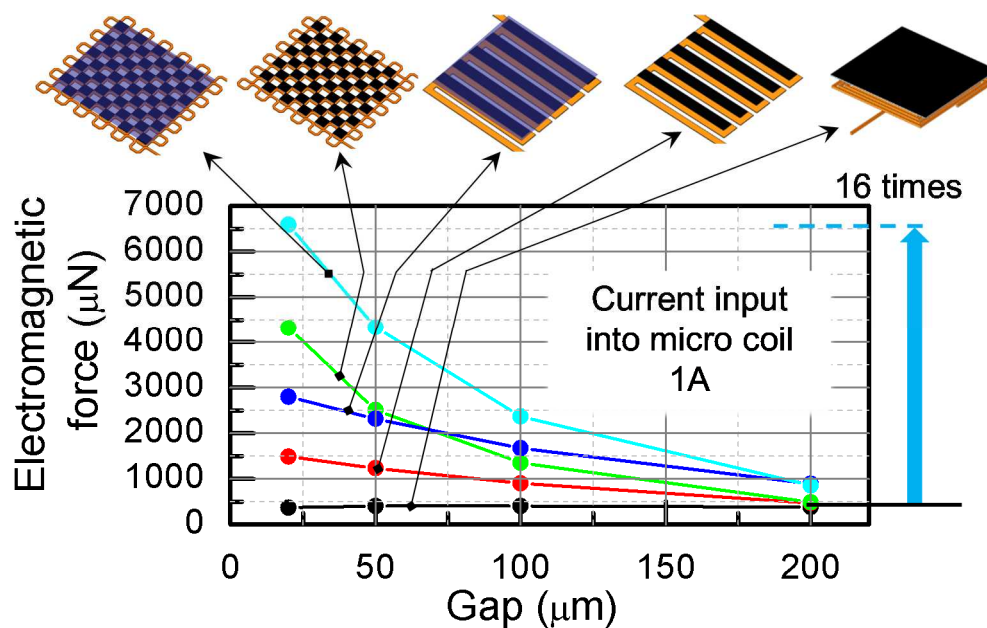


Fig. 4.13 Electromagnetic force between micro-coil and permanent magnet

4.3 Fabrication of the planar-type electromagnetic actuators

4.3.1 Fabrication of TFPM patterns

The fabrication process of the patterned TFPM is shown in Fig. 4.14. The procedure is as follows:

(1) A 20mm \times 20mm, 200 μm thick Si substrate is prepared. A TFPM is deposited onto the Si by magnetron sputtering, the sputtering condition is same

as in Table 2.2. During the sputtering process, the sputtering target is gradually consumed, causing the decrease of the deposition rate. Due to the variation of the deposition rate, the thickness of TFPM is $14.8\mu\text{m}$, which is lower than the designed value of $20\mu\text{m}$. The non-segmented TFPM in Type 1 is then fabricated by only dicing the substrate.

(2) A $20\mu\text{m}$ thick SU8 resist (SU8-25, MicroChem Corp.) is spin-coated and patterned on TFPM surface by photolithography. The process parameters for patterning SU8 resist are the same as in the manual in [53] (Type 2, Type 3).

(3) The substrate is then etched by an argon ion milling process (IMR-3-8, Hitachi, Ltd.), transferring the resist pattern to TFPM (Type 2, Type 3). The parameters for ion milling are:

- Acceleration voltage: 400V
- Acceleration current: 0.6A
- Etching beam angle: 45°
- Etching rate: $1.5\mu\text{m/h}$

(4) The remaining SU8 is removed by oxygen plasma ashing (RIE-101L, SAMCO Inc.). The line/space and chessboard patterns in the Type 2(1) and Type 3(1) are realized after this step. The ashing conditions are:

- Gas flow rate: 20sccm
- RF power: 50W
- Chamber pressure: 100mTorr
- Processing time: 180min

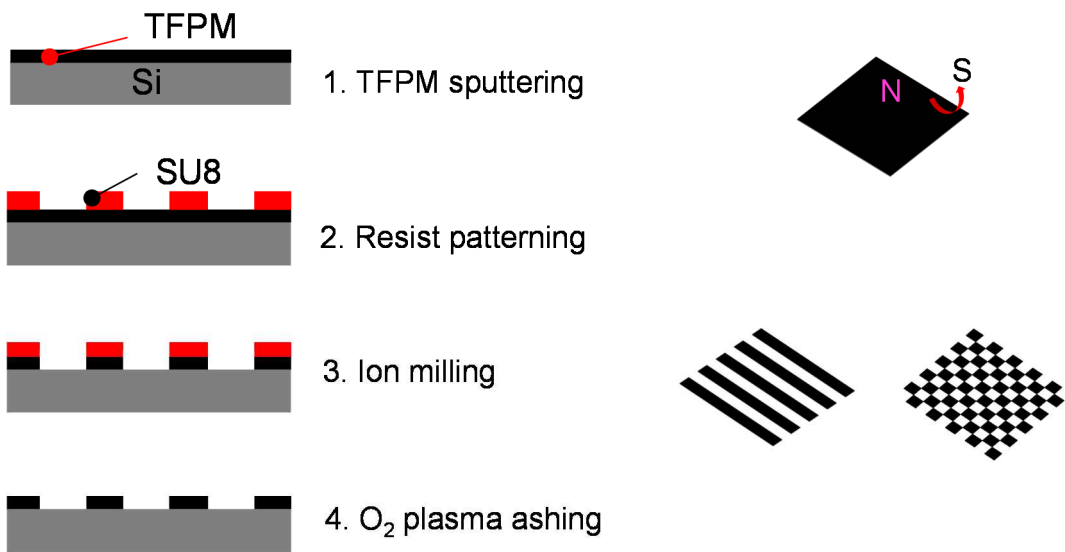


Fig. 4.14 Fabrication process of TFPM patterns



Fig. 4.15 TFPM substrate patterned with SU8-25

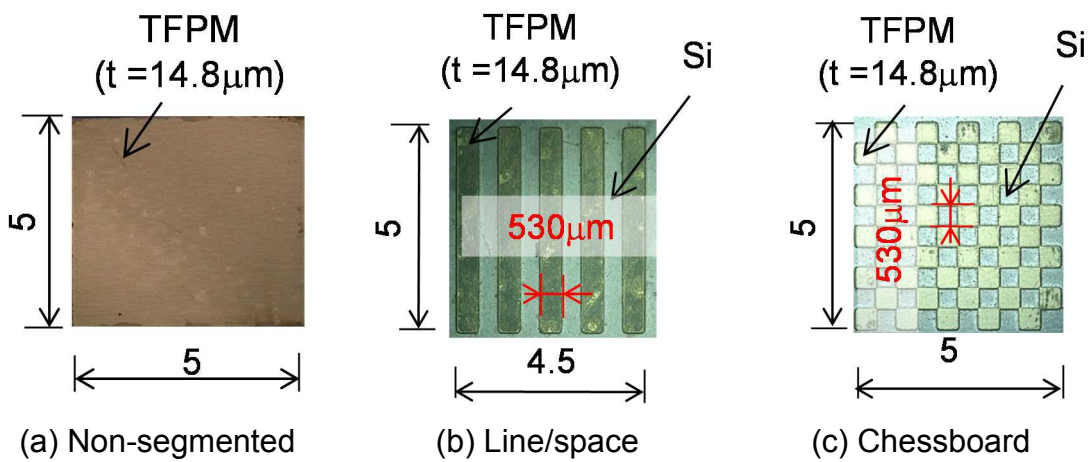


Fig. 4.16 Fabrication result of TFPM patterns

The substrate patterned with 20 μm thick SU8 is shown in Fig. 4.15. The unit size of SU8-25 patterning is from 515 μm to 520 μm . The fabricated TFPM patterns are shown in Fig. 4.16, and the unit size of permanent magnet pattern in line/space and chessboard is 530 μm due to the etching error. As the ion etching angle is 45°, the shading effect enlarges the profile of TFPM after etching.

4.3.2 Fabrication of permalloy layer by electroplating

The fabrication process of the permalloy layer is shown in Fig. 4.17. The procedure is as follows:

(1) A seed layer consisting of 20nm thick Ti and 500nm thick Ni is sputtered onto the substrates through a magnetron sputtering process (L-250S-FH, CANON ANELVA CORP.). The process parameters are:

- Power: 100W for both
- Ar gas flow rate: 10sccm for both
- Chamber pressure: 1Pa for both
- Process time: 7min for Ti and 30min for Ni

(2) An 11 μm thick permalloy ($\text{Ni}_{55}\text{Fe}_{45}$) is electroplated in Type 2(2) and Type 3(2) designs. The experimental parameters are shown in Table. 4.1.

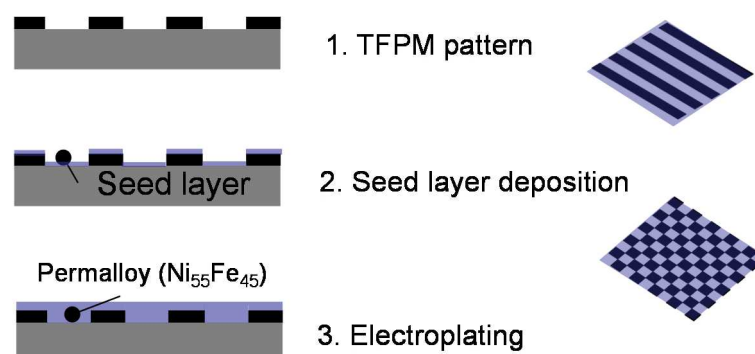


Fig. 4.17 Permalloy fabrication process

Table 4.1 Experimental conditions for electroplating permalloy

Material/Item	Parameter
$(\text{Ni}(\text{H}_2\text{NSO}_3)_2 \cdot 4\text{H}_2\text{O})$	1000mol/m^3
$(\text{NiCl}_2 \cdot 6\text{H}_2\text{O})$	100mol/m^3
H_3BO_3	650mol/m^3
$\text{C}_7\text{H}_5\text{NO}_3\text{SNa}$	1.8kg/m^3
$\text{FeCl}_2 \cdot 4\text{H}_2\text{O}$	200mol/m^3
$\text{NaC}_{12}\text{H}_{25}\text{SO}_4$	0.1kg/m^3
Temperature	313K
pH	2.38
Current	100A/m^2
Electroplating rate	$7.44\mu\text{m/h}$

The element content of the permalloy is tested by a glow discharge optical emission spectroscopy (GDOES, JY 5000 RF, HORIBA, Ltd.). The result is shown in Fig. 4.18. The weight percentages of Ni and Fe are around 55% and 45%, respectively. The fabricated permalloy on TFPM patterns are shown in Fig. 4.19. The permalloy thickness is $11\mu\text{m}$.

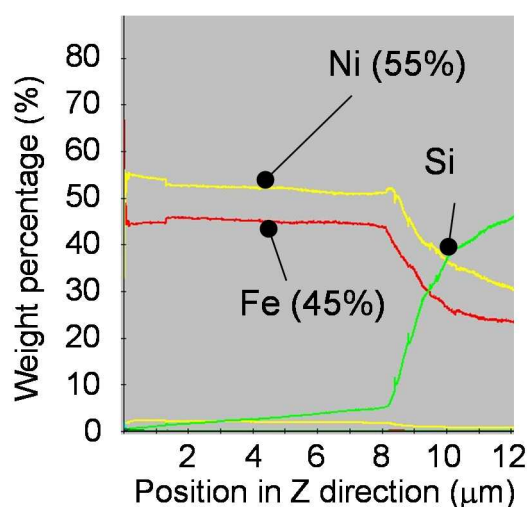
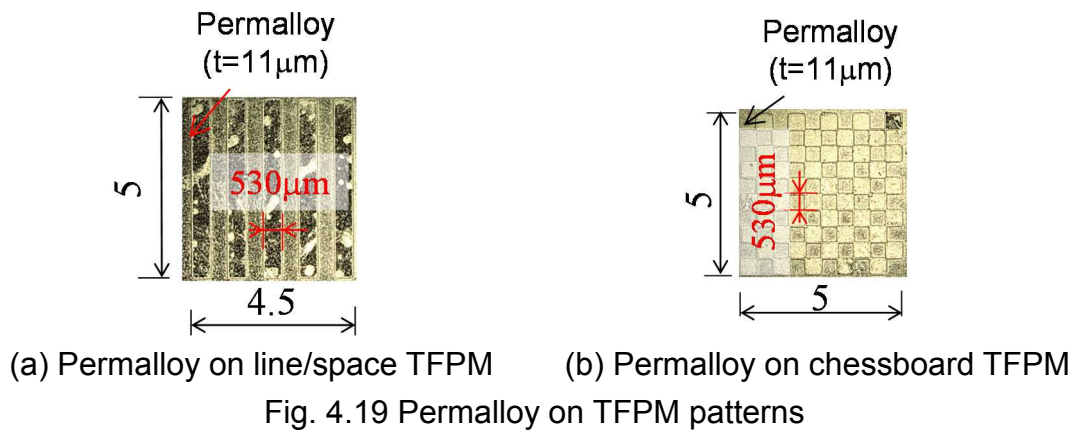


Fig. 4.18 Element content measurement of the test sample (GDOES test)



4.3.3 Fabrication of micro-coil

To fabricate the Type 1 micro-coil, a PCB process is adopted. The detailed fabrication process and result are shown in Fig. 4.20. The coil thickness is $35\mu\text{m}$, and the electric resistance of micro-coil is 0.98Ω .

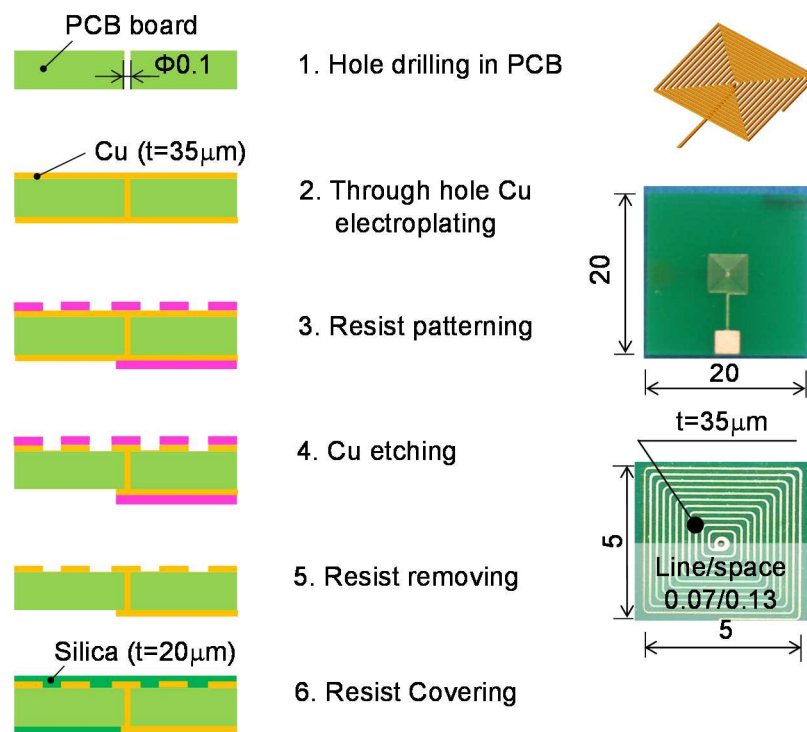


Fig. 4.20 Spiral micro-coil fabricated by PCB process

To fabricate the Type 2 and Type 3 micro-coils, a lift-off process is utilized. The fabrication process is shown in Fig. 4.21. The parameters are as follows:

(1) A 140 μ m thick KMPR resist (KMPR 1035, MicroChem Corp.) is patterned on Si substrate using photolithography. The parameters are:

- Spin-coat: 500rpm, 10s; ramp 300rpm/s; 1400rpm, 30s
- Soft-bake: 373K, 20min
- Exposure: 250s
- Post exposure bake: 373K, 4min
- Development: SU8 developer (MicroChem. Corp.), 10min
- Rinse: IPA 5min; pure water 5min

(2) A 100nm thick Cr contacting layer, a 15 μ m thick Cu conducting layer, and a 100nm thick Cr protection layer are sputtered in sequence onto the substrate (L-250S-FH, CANON ANELVA CORP.). The sputtering parameters are:

- Power: 100W for all
- Ar gas flow rate: 10sccm for all
- Chamber pressure: 1Pa for all
- Process time: 5min for Cr, 5 hours for Cu and 5min for Cr

(3) The KMPR is removed, leaving only the patterned coils on Si substrates. The substrates are treated in the following processes in sequence:

- Remover PG (MicroChem. Corp.) at 343K for 20min
- Remover K (MicroChem. Corp.) at 343K for 20min
- H₂O₂ solution (30% concentration) with ultrasonic treatment for 5min
- Pure water rinse

The Si substrates after patterning with 140 μ m thick KMPR are shown in Fig. 4. 22. The line widths of meander pattern and mesh pattern are 296 μ m and 80 μ m, respectively.

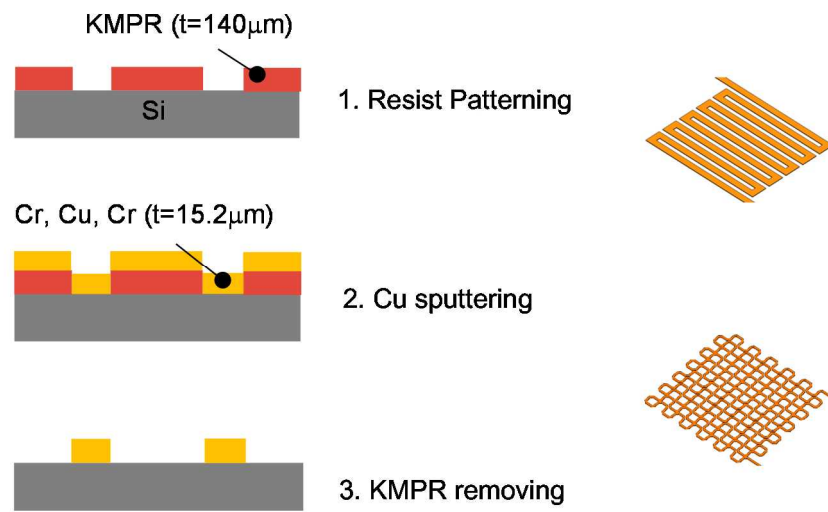


Fig. 4.21 Fabrication process of micro-coil in Type 2 and Type 3

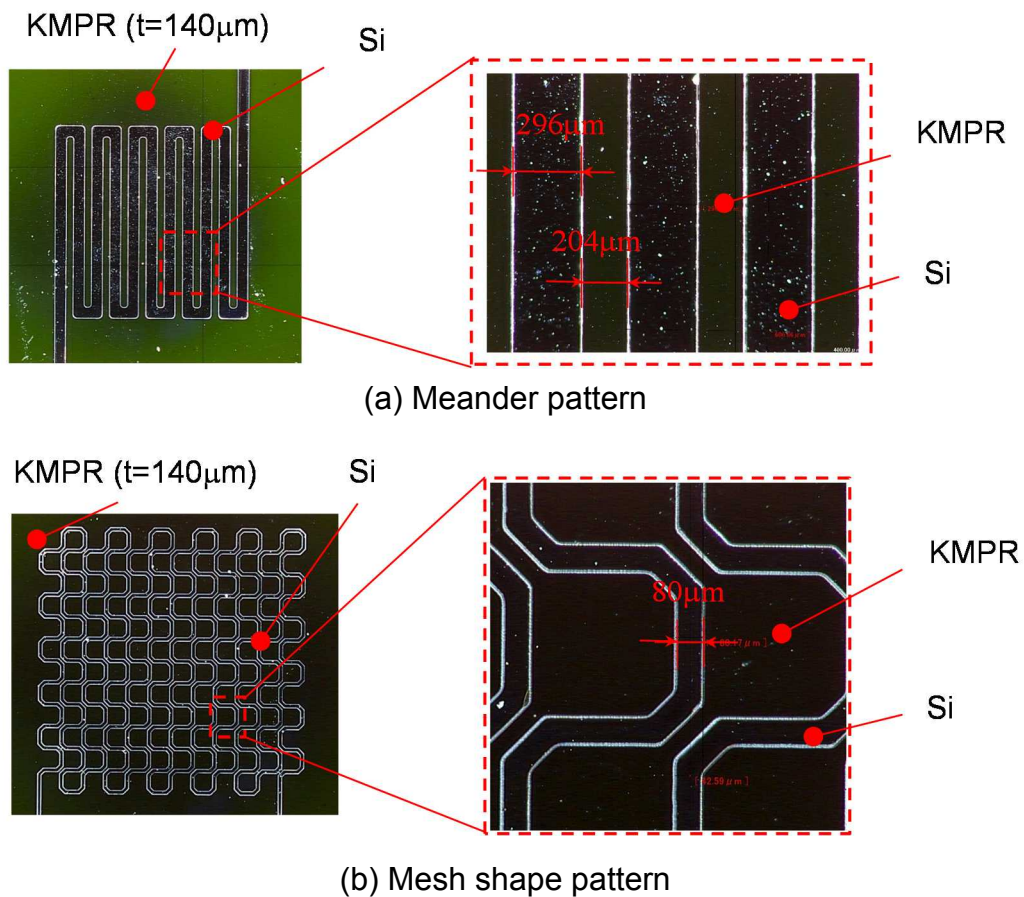
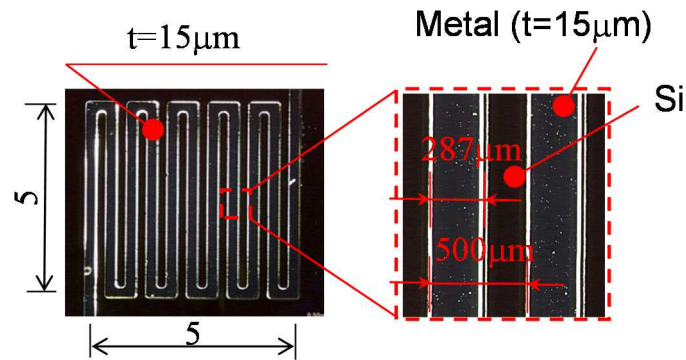
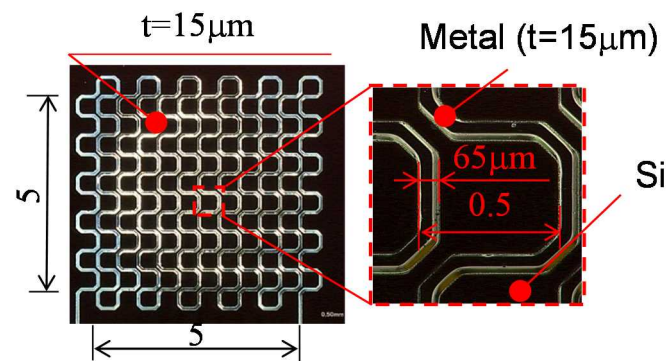


Fig. 4.22 Si substrate patterned with KMPR resist

The fabricated micro-coils on Si are shown in Fig. 4.23. The coil line widths are $287\mu\text{m}$ and $65\mu\text{m}$ for meander pattern and mesh pattern. The thickness of the coil is $15\mu\text{m}$, which is measured by a stylus profiler (Dektak, Bruker, Corp.). The measured resistances of the coils are 0.46Ω and 2.96Ω for the Type 2 and Type 3 designs.



(a) Coil of Type 2



(b) Coil of Type 3

Fig. 4.23 Fabricated micro-coils

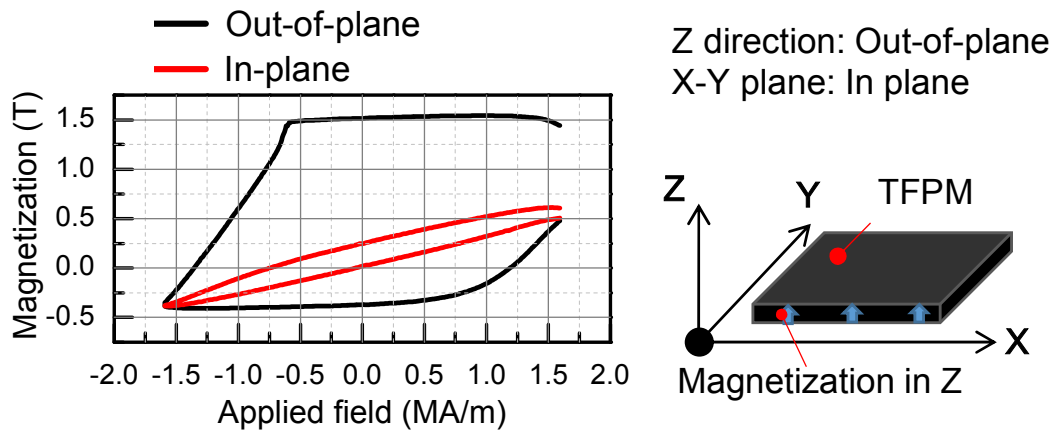


Fig. 4.24 J-H curve of TFPM

4.4 Evaluation of the actuator

4.4.1 Evaluation of the magnetic property of TFPM

VSM is used to measure the magnetic properties of TFPM. The J-H curves of TFPM in both out-of-plane and in-plane are illustrated in Fig. 4.24. The TFPM's B_r and H_c are 1.51T and 1.06MA/m in out-of-plane direction.

4.4.2 Evaluation of the magnetic property of permalloy

The magnetic property of permalloy is evaluated by VSM. The results are shown in Fig. 4.25. The magnetization of permalloy saturates at 1.2T for both out-of-plane and in-plane direction, which is similar to that of $\text{Ni}_{55}\text{Fe}_{45}$ in [51]. However, the permalloy exhibits magnetic anisotropy in out-of-plane and in-plane directions.

The magnetic anisotropy of the permalloy might be caused by the magnetic field generated by electroplating current [60]. Furthermore, the Ni seed layer may also influence the crystal structure of the permalloy, thus changing its magnetic anisotropy.

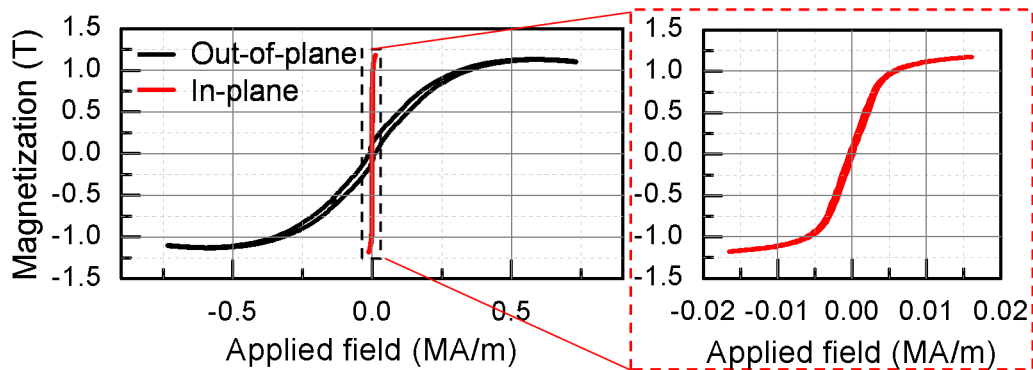


Fig. 4.25 J-H curve of the permalloy

4.4.3 Evaluation of surface magnetic flux density

The magnetic flux density above the surface of the fabricated substrates are measured using a Hall element probe (HG-0711, Asahi Kasei Microdevices Corp.). As the Hall element probe can only measure the magnetic flux density in one direction. The magnetic flux density in Z direction is measured. The measurement path is line B-B in Plane 1. Meanwhile, the magnetic flux density is simulated considering the measured geometrical parameters such as thickness of TFPM, thickness of permalloy and feature size of TFPM pattern and magnetic parameters such as J-H curve of TFPM, J-H curve of permalloy.

Figure 4.26 shows the comparisons between the measured and simulated results, revealing that the experimental results agree well with the simulated ones. It demonstrates that the patterning process of TFPM, especially the SU8 patterning process and argon ion beam etching process do not damage the magnetic property of TFPM.

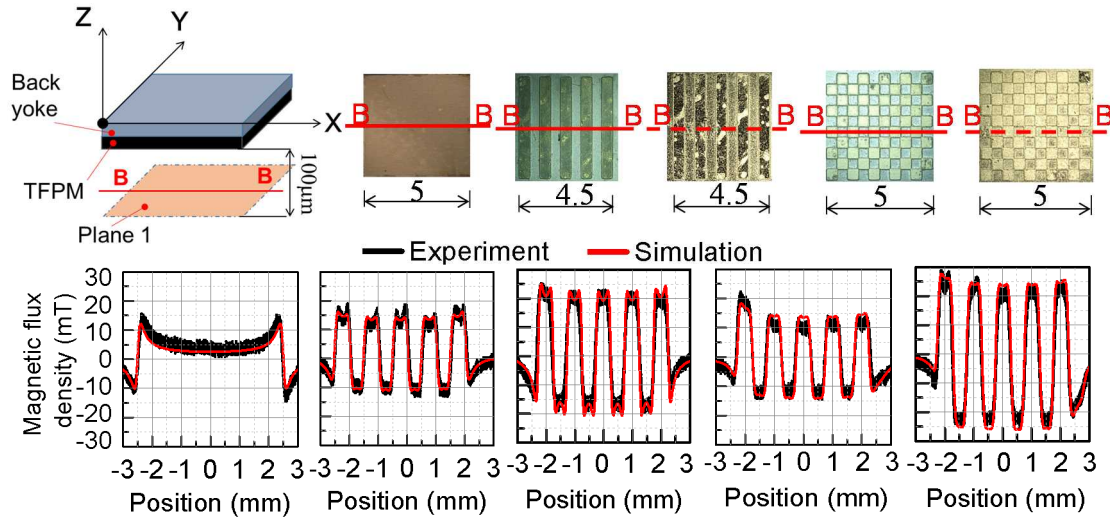


Fig. 4.26 Magnetic flux density distribution in line B-B
(100 μ m beneath the TFPM surface)

4.4.4 Evaluation of the electromagnetic force

The electromagnetic force between permanent magnet pattern and micro-coil is measured using the electronic force balance. The measurement principle is the same as in Chapter 2, and the measurement setup is shown in Fig. 4.27. The micro-coil is placed on the electronic force balance. Meanwhile, the TFPM is attached to a non-magnetic X-Y-Z- Θ_z fine stage, which has a resolution of 1 μ m in X, Y, Z directions and 0.1 degree in Θ_z direction.

The measured results are then compared with the simulated ones in Fig. 4.28. The experimental results are around 70% to 90% of the simulated values. The experimental errors of Type 2 and Type 3 actuators are larger than that of Type 1. Attention should be paid that the alignment between permanent magnet and micro-coil has a significant effect on the electromagnetic force. This effect will be evaluated in detail in Section 4.4.6.

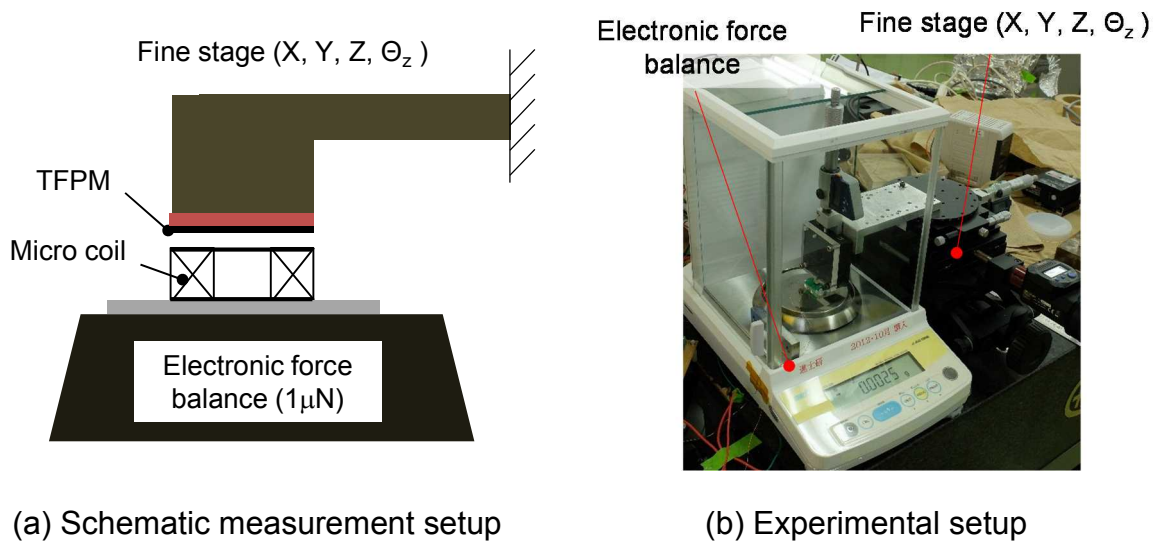
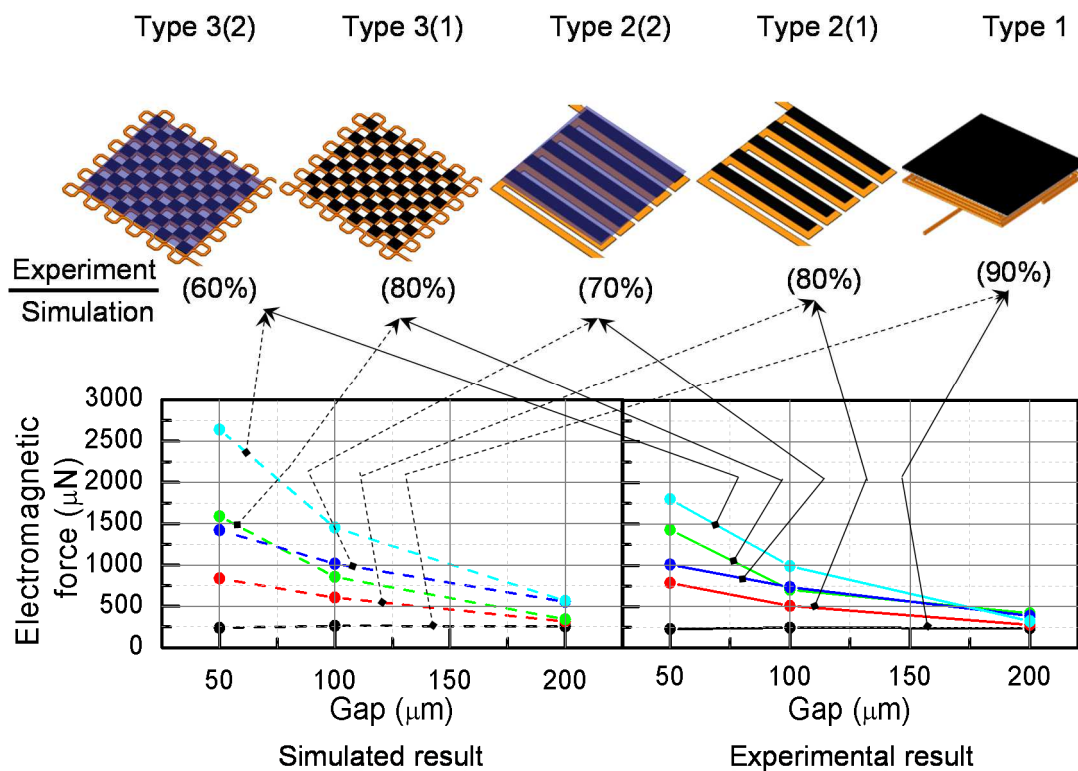


Fig. 4.27 Electromagnetic force evaluation setup

Fig. 4.28 Electromagnetic force evaluation result
(1A Current input into the coil)

4.4.5 Evaluation of force/energy density

As the electromagnetic force between coil and permanent magnet is a kind of body force [10], the force magnitude is proportional to the volume of the actuator. In order to evaluate the actuator's capability of force/energy generation, two indexes are defined: force density (D_F) and energy density (D_E). They can be calculated by the following two equations:

$$D_F = F/V \quad (4.5)$$

$$D_E = \int_l D_F dl \quad (4.6)$$

Where

F : Electromagnetic force with 1A current input into the coil

V : Sum of permanent magnet volume and coil volume

l : Working distance of the actuator

The force density relationship with gap is shown in Fig. 4.29. The Type 3(2) and Type 1 actuator are compared with the planar electromagnetic actuator developed in [42]. Energy density is the integration of force density on its working distance (the "Gap" in Fig. 4.29). It equals to the area beneath the force density curve. The maximum force density and the energy density of the three actuators are calculated in Table 4.2 and compared with the one of bulk electromagnetic actuator in [9]. The Type 3(2) actuator attains a maximum force density 20 times and an energy density that is over 20 times of the one in [42]. The Type 3(2) actuator also exhibits superior force and energy density to the ones of bulk actuator. It can be concluded that the Type 3(2) actuator has high force/energy density.

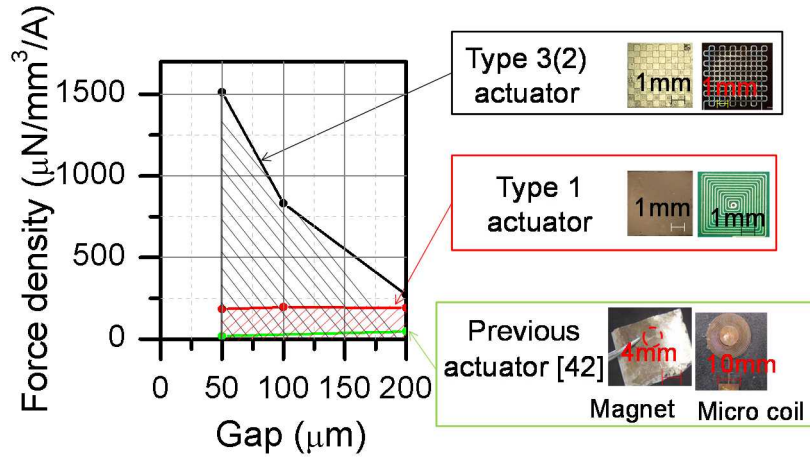


Fig. 4.29 Force density of the three types of actuators

Table 4.2 Maximum force density and energy density comparison

Actuator type	$D_{F\ MAX}$ ($\mu\text{N}/\text{mm}^3/\text{A}$)	D_E ($\text{J}/\text{mm}^3/\text{A}$)
Type 3(2)	1512.6	1.14×10^{-7}
Type 1	195.0	2.87×10^{-8}
Actuator in [42]	75.2	4.23×10^{-9}
Actuator in [9]	43.3	2.97×10^{-9}

4.4.6 Evaluation of misalignment effect on the actuator performance

In Section 4.4.4, the Type 2 and Type 3 attain higher electromagnetic force than that of Type 1 within 200μm gap. The alignment error between the TFPM and micro-coil degrades the performance. In this section, the effect of the alignment error on force is evaluated and explained by simulation.

Figure 4.30(a) shows the simulation model when there is a tilt alignment error between the TFPM and micro-coil by assuming Y axis rotational direction's tilt. Figure 4.30(b) shows the electromagnetic force with and without alignment error. The solid lines represent forces without alignment error, and the dashed lines show the ones with 1° alignment error. For Type 3(1), the force with the alignment

error is 40% lower than that of without alignment error. The force of Type 2(1) decreases 20%. The force of Type 1 keeps almost the same. It can be concluded that Type 2(1) and Type 3(1) are very sensitive to tilt alignment errors, but Type 1 actuators is robust.

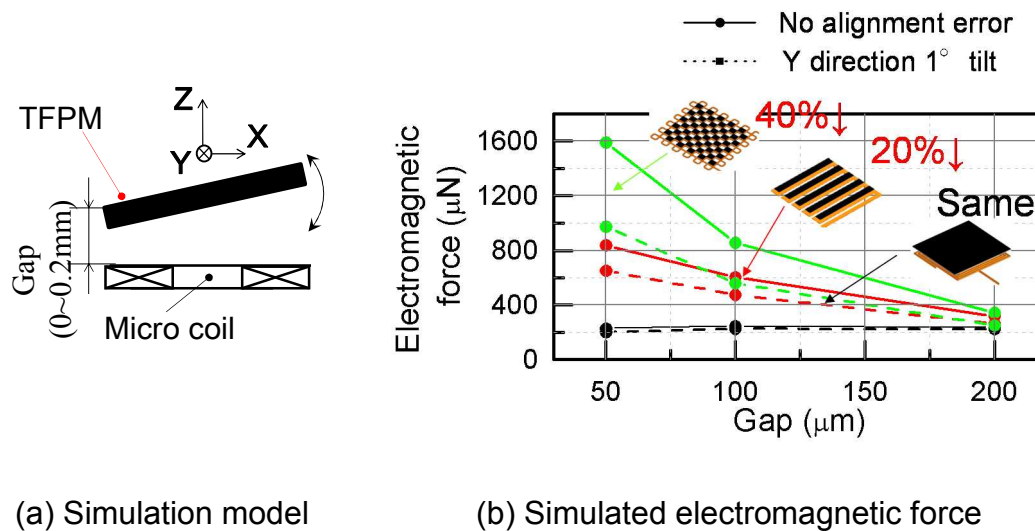


Fig. 4.30 Misalignment effects on the actuator performance

Table 4.3 shows the variations of electromagnetic force for different types of alignment error. Type 1 is insensitive to alignment errors in all direction. Type 3(1) is more sensitive to alignment errors than Type 2(1). To keep the designed force in the case of Type 2(1) and Type 3(1) actuators, precise positioning is necessary.

Table 4.3 Alignment errors' effect on the actuators' force magnitude

	Aligned	ΔX 0.1mm	ΔY 0.1mm	X axis tilt 1°	Y axis tilt 1°
Type 1	100%	101%	95%	90%	93%
Type 2(1)	100%	75%	99%	78%	77%
Type 3(1)	100%	69%	68%	65%	66%

The misalignment effect on the actuator performance can be further explained by Lorentz Law. The electromagnetic force generated on the micro coil by external magnetic field can be calculated, which is expressed in Eq. 4.7.

$$\vec{F} = \int_l I \cdot d\vec{l} \times \vec{B} \quad (4.7)$$

Where I is the current in the coil, \vec{B} is the magnetic flux density and \vec{l} is the wire tangent vector. Figure 4.31 is the schematic view of \vec{B} and force generated on the coil cross section. The \vec{B} at the micro coil plane (XY plane) can be divided into out-of-plane vector (\vec{B}_z) and in-plane vector (\vec{B}_\perp , \vec{B}_\parallel). In the XY plane, \vec{B}_\parallel is parallel to the coil direction and \vec{B}_\perp is perpendicular to the coil direction. \vec{B}_z generates force in the in-plane direction and \vec{B}_\perp generates force in the Z direction. In this research, the force in the Z direction is considered. The force magnitude can be expressed as the integration of B_\perp scalar along the coil path.

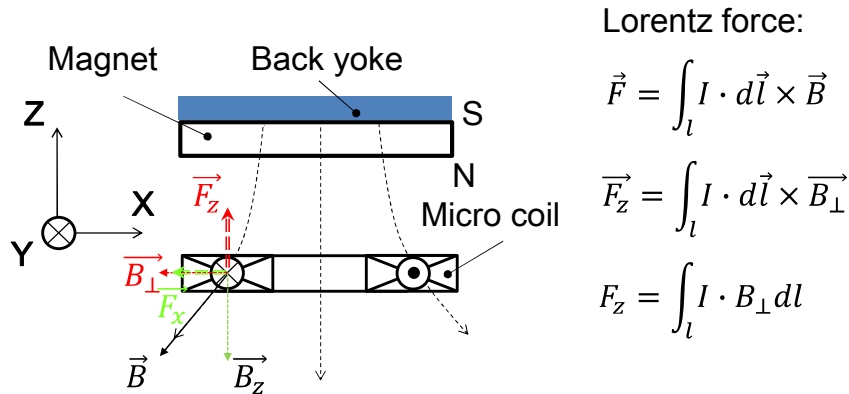


Fig. 4.31 Analysis of B field and force on the coil cross section

The B_\perp working on the micro coils of Type 1, Type 2(1) and Type 3(1) are simulated, respectively. Fig. 4.32 indicates the simulation models. For the micro coil in Type 1, line 1 is selected as a typical coil turn because it can generate the maximum force. In Type 2(1), line 2 is selected as one unit of the meander coil. Line 31 and line 32 are selected as one unit of the mesh coil in Type 3(1). The gap between micro coil and permanent magnet is $100\mu\text{m}$.

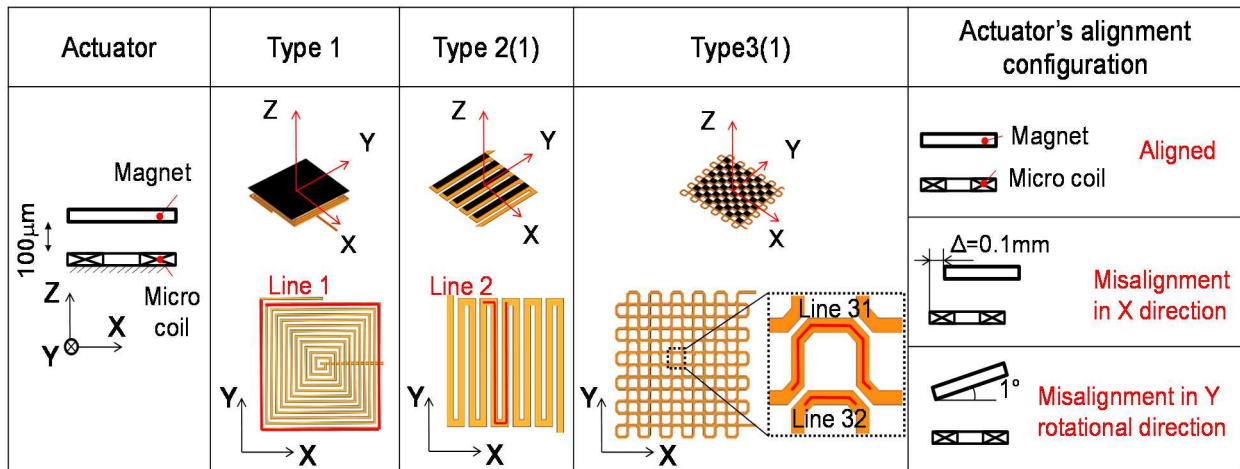


Fig. 4.32 Models of micro coils in Type 1, Type 2(1) and Type 3(1)

The simulated B_{\perp} on the selected lines are shown in Fig. 4.33, Fig. 4.34 and Fig. 4.35. In each figure, black, red and green lines indicate the B_{\perp} generated by no alignment error, 0.1mm alignment error in X direction and 1° alignment error in Y rotational direction. The integration of B_{\perp} along each line is also calculated.

In Fig. 4.33, although the B_{\perp} profile is changed by alignment errors, the integration of B_{\perp} on line 1 keeps almost the same. Thus, the force changes little.

In Fig. 4.34, when alignment errors occur, the magnitude of B_{\perp} decreases. The integration of B_{\perp} decreases to 75% with 0.1mm alignment error in X direction and 76% with 1° alignment error in Y rotational direction.

In Fig. 4.35, the integration of B_{\perp} decreases to 65% with 0.1mm alignment error in X direction and 63% with 1° alignment error in Y rotational direction.

From the discussion above, it can be concluded that the alignment error affects the distribution of magnetic flux density, thus changing the generated electromagnetic force.

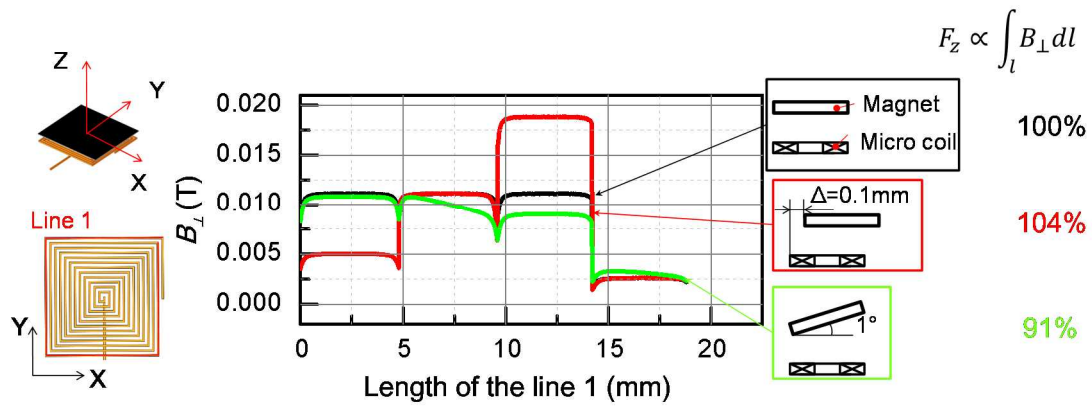


Fig. 4.33 B_{\perp} on line 1 in Type 1 actuator

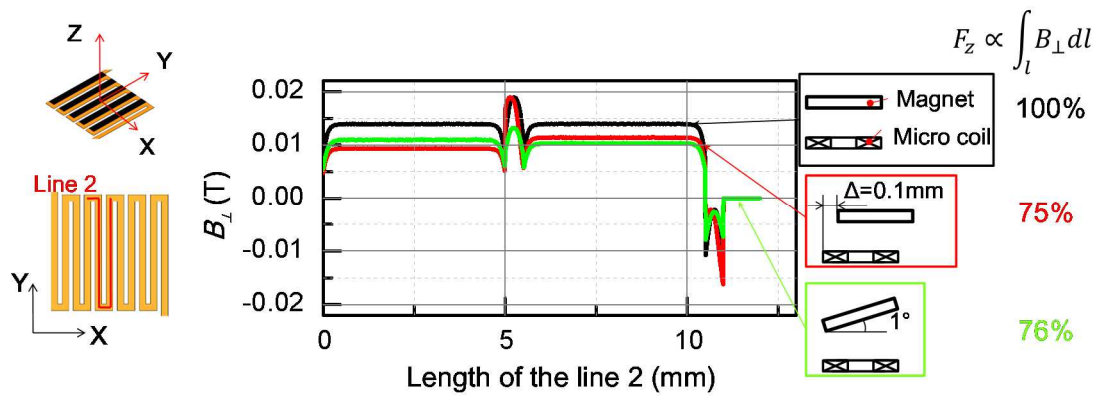


Fig. 4.34 B_{\perp} on line 2 in Type 2(1) actuator

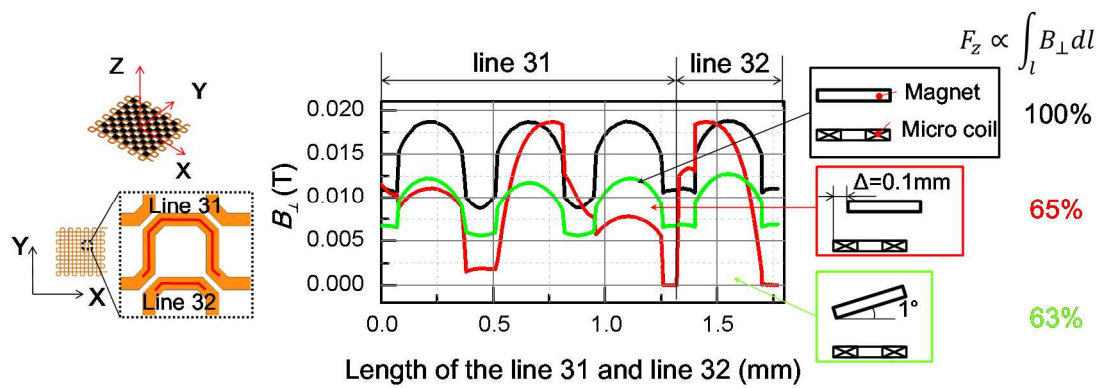


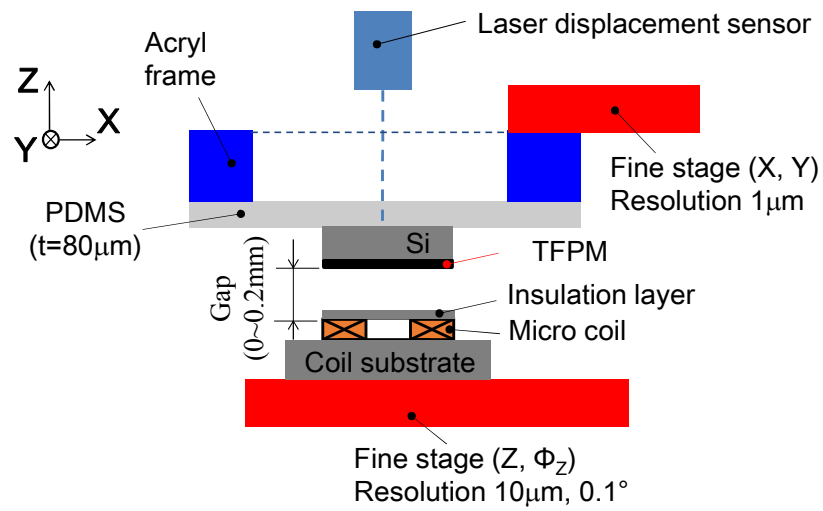
Fig. 4.35 B_{\perp} on line 31 and line 32 in Type 3(1) actuator

4.4.7 Evaluation of PDMS diaphragm's displacement

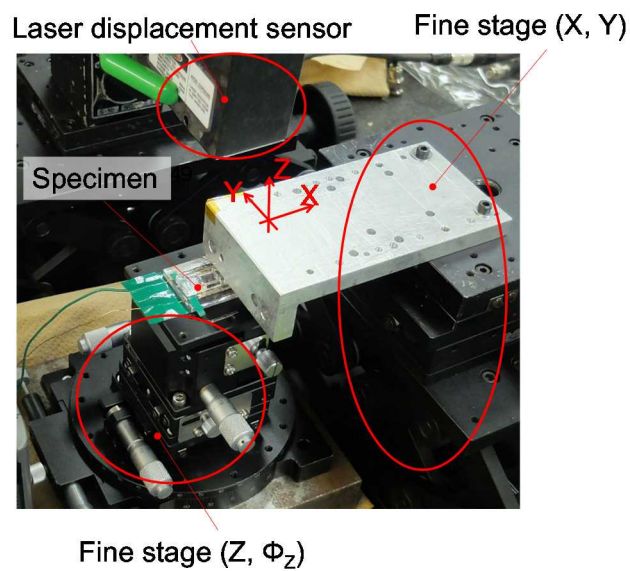
The TFPM is attached on PDMS diaphragm to measure the diaphragm displacement. The evaluation principle is to measure the force-displacement curve of the diaphragm-type actuators, which is the same as the ones in Chapter 2 and Chapter 3.

The schematic measurement setup is illustrated in Fig. 4.36(a). An 80 μm thick PDMS diaphragm is attached to an acryl frame by uncured PDMS and is positioned by a fine X-Y fine stage having 1 μm resolution in X and Y directions. The TFPM pattern on a Si substrate (TFPM-Si) is bonded with the PDMS diaphragm using uncured PDMS followed by curing at room temperature for 24 hours. A fine stage adjusts the position of the micro-coil in the Z and Φ_z directions having 1 μm and 0.1° resolution, respectively. The laser displacement sensor is utilized to measure the displacement at the center of the TFPM. The gap between the TFPM and PDMS is adjusted by the Z fine stage within 0.2mm gap. The experimental setup is shown in Fig. 4.36(b).

Figure 4.37 shows the experimental specimens which consist of TFPM-Si on PDMS diaphragms and micro-coils. To avoid the short circuit between the coil and the TFPM, the coil is covered with an insulation layer. Type 1 coil is covered with a 20 μm thick layer of silica during the PCB fabrication process, as shown in Fig. 4.20. The micro-coils in Type 2 and Type 3 are covered with a 20 μm thick SU8-10 resist after “lift-off” process. The thickness of SU8-10 layer is measured by the stylus profiler.



(a) Schematic measurement setup



(b) Experimental measurement setup

Fig. 4.36 Setup for measuring the diaphragm displacement

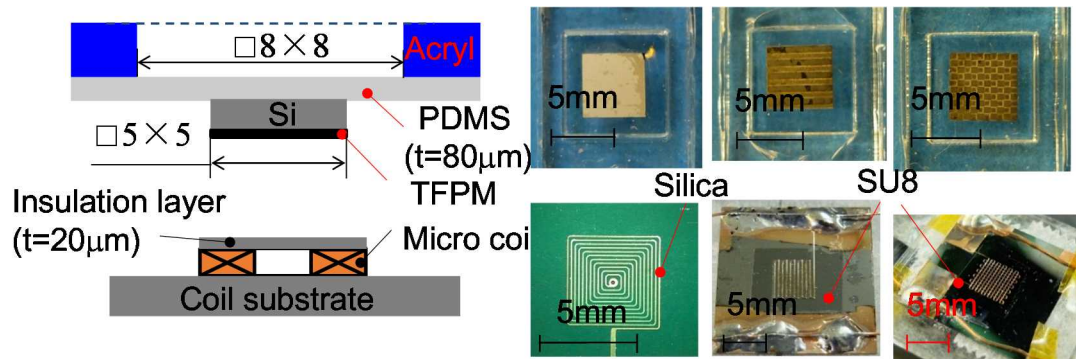


Fig. 4.37 Experimental specimen

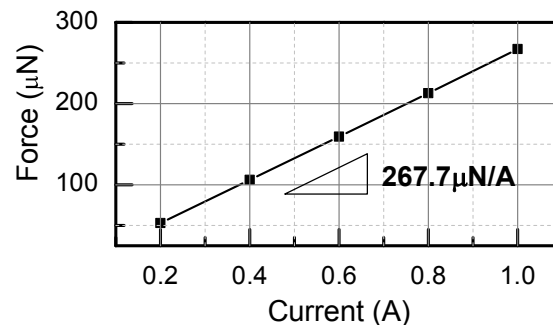
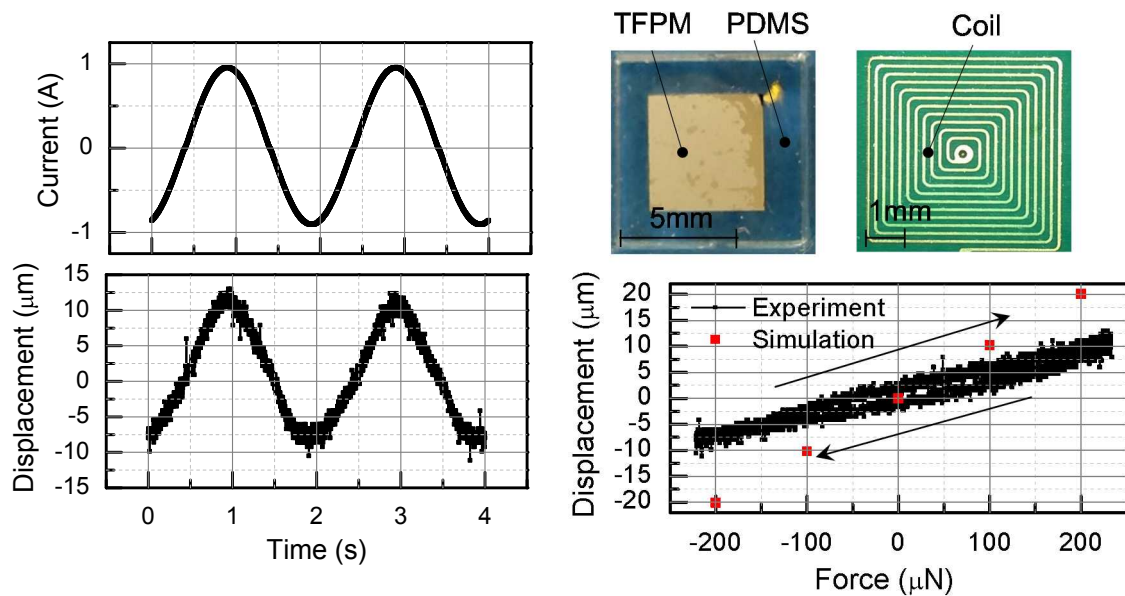


Fig. 4.38 Simulated force-current curve for Type 1 actuator (100μm Gap)



(a) Measured current and displacement

(b) Force-displacement curve

Fig. 4.39 Displacement curve of Type 1 DEMA

The diaphragm displacements of Type 1, Type 2(1) and Type 3(1) DEMAs are then measured, respectively. The initial gap between the TFPM and micro-coil is $100\mu\text{m}$.

The time-current and time-displacement curves of Type 1 DEMA are shown in Fig. 4.39(a). The force keeps almost the same when the gap between the TFPM and micro-coil changes from $50\mu\text{m}$ to $200\mu\text{m}$, which is indicated in Fig. 4.28. With a fixed gap of $100\mu\text{m}$, the force and current relationship is simulated. They have a coefficient of $267.7\mu\text{N/A}$, as shown in Fig. 4.38. The measured one is $244\mu\text{N/A}$. The force-displacement curve is derived and compared with simulated ones in Fig. 4.39(b). The Type 1 DEMA generates displacement of $\pm 8\mu\text{m}$. The reason of error between simulation and experiment is not clear currently.

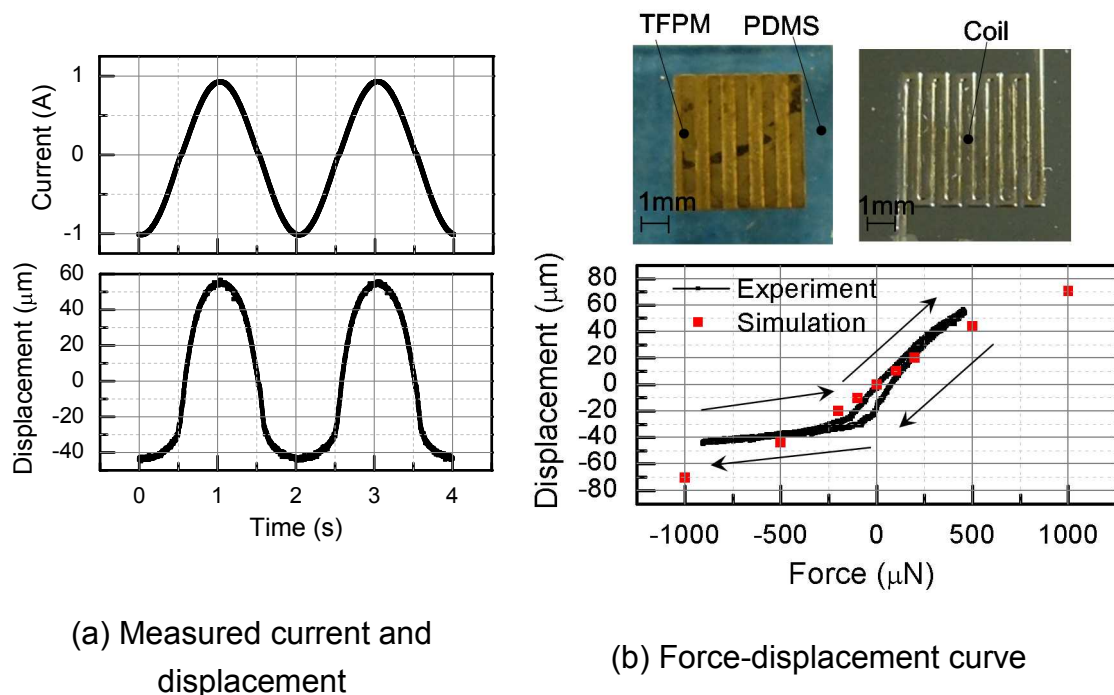


Fig. 4.40 Displacement curve of Type 2(1) DEMA

The time-current and time-displacement curves of the Type 2(1) DEMA and Type 3(1) DEMA are also measured, as shown in Fig 4.40(a) and Fig. 4.41(a). The Type 2(1) DEMA generates a displacement of $[+60\mu\text{m}, -40\mu\text{m}]$ with input current of $[+1\text{A}, -1\text{A}]$. The displacement profile at $-40\mu\text{m}$ at time point 2s is “flat”.

This is caused by the contact between TFPM and micro coil. The mesh coil in Type 3(1) has a relative large electric resistance of 2.96Ω . In the case of stable current input, in order to protect the coil, the current input into the coil is limited to $0.7A$ in amplitude. The Type 3(1) DEMA can generate a displacement of $[+50\mu m, -40\mu m]$ with an input current of $[+0.7A, -0.7A]$.

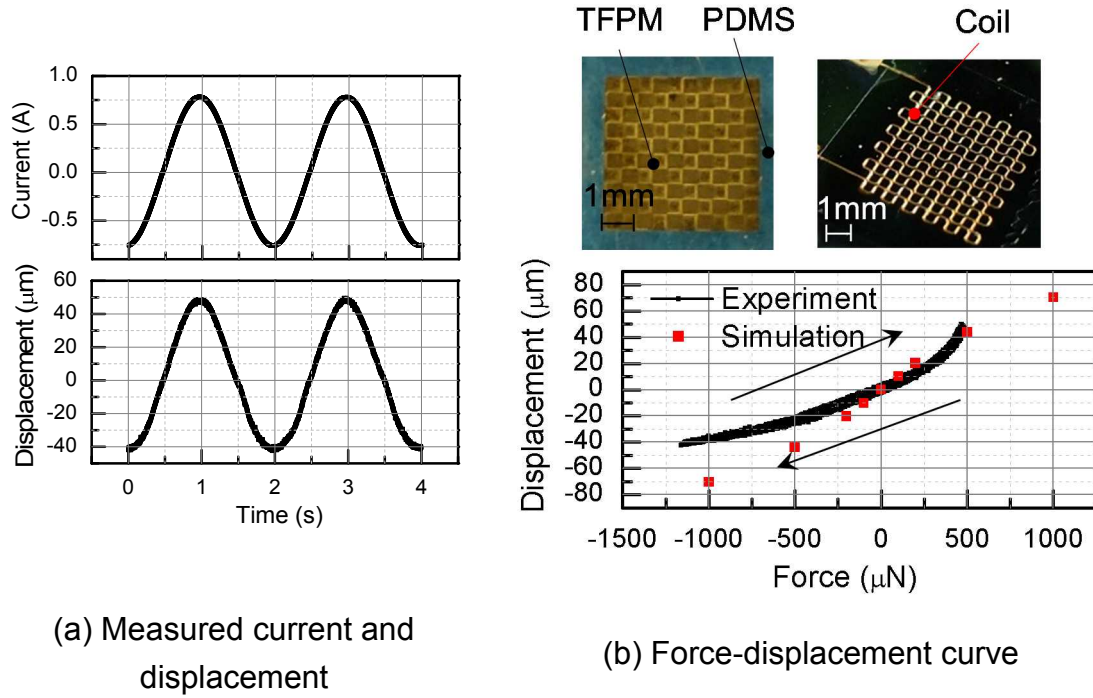


Fig. 4.41 Displacement curve of Type 3(1) DEMA

Because the electromagnetic forces generated by Type 2(1) DEMA and Type 3(1) DEMA are dependent on the gap g , the actuators generate different forces with different gaps. Equation 4.8 and Eq. 4.9 are utilized to transform the current-displacement curve to force-displacement curve for Type 2(1) and Type 3(1) actuators. The equations are derived by curve fitting from the experimental results in Fig. 4.28. The unit of g and F are μm and μN .

$$F_{Type\ 2(1)} = I \times (1175 - 8.88g + 0.022g^2) \quad (4.8)$$

$$F_{Type\ 3(1)} = I \times (3595 - 38g + 0.11g^2) \quad (4.9)$$

The experimentally derived force-displacement curves of Type 2(1) DEMA

and Type 3(1) DEMA are compared with the simulated results in Fig. 4.40(b) and Fig. 4.41(b). The simulated and experimental results do not coincide.

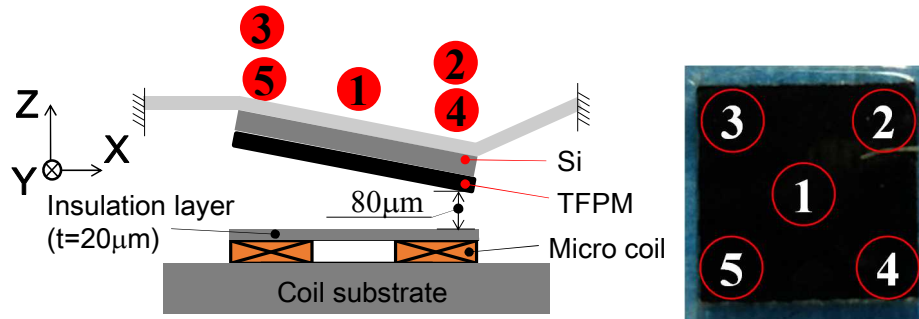


Fig. 4.42 Diaphragm displacements measurement at different points

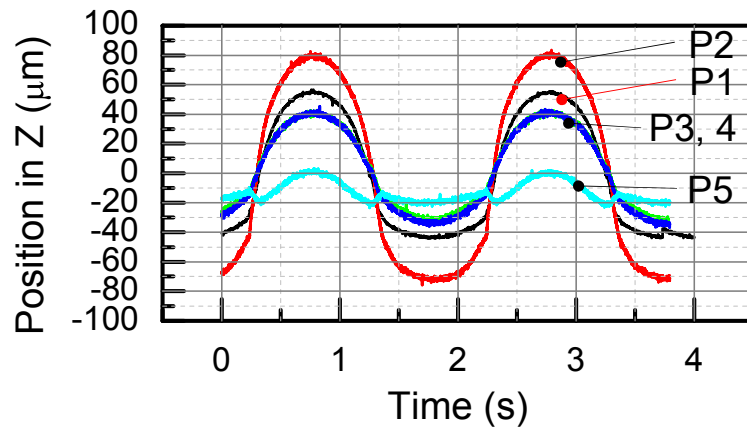


Fig. 4.43 Diaphragm displacements profile at different points

The diaphragm displacements are different at each measurement point. The diaphragm displacement at five points of Type 2(1) DEMA are measured, shown in Fig. 4.42. The displacement magnitude is maximum at point 2 and smallest at point 5. The displacements at point 1, 3, 4 are almost the same. It indicates that the diaphragm has a tilt motion along the rotational axis which passes point 5. While in simulation, the tilt motion is not considered. Thus it may be one reason that causes differences between simulation and experiment.

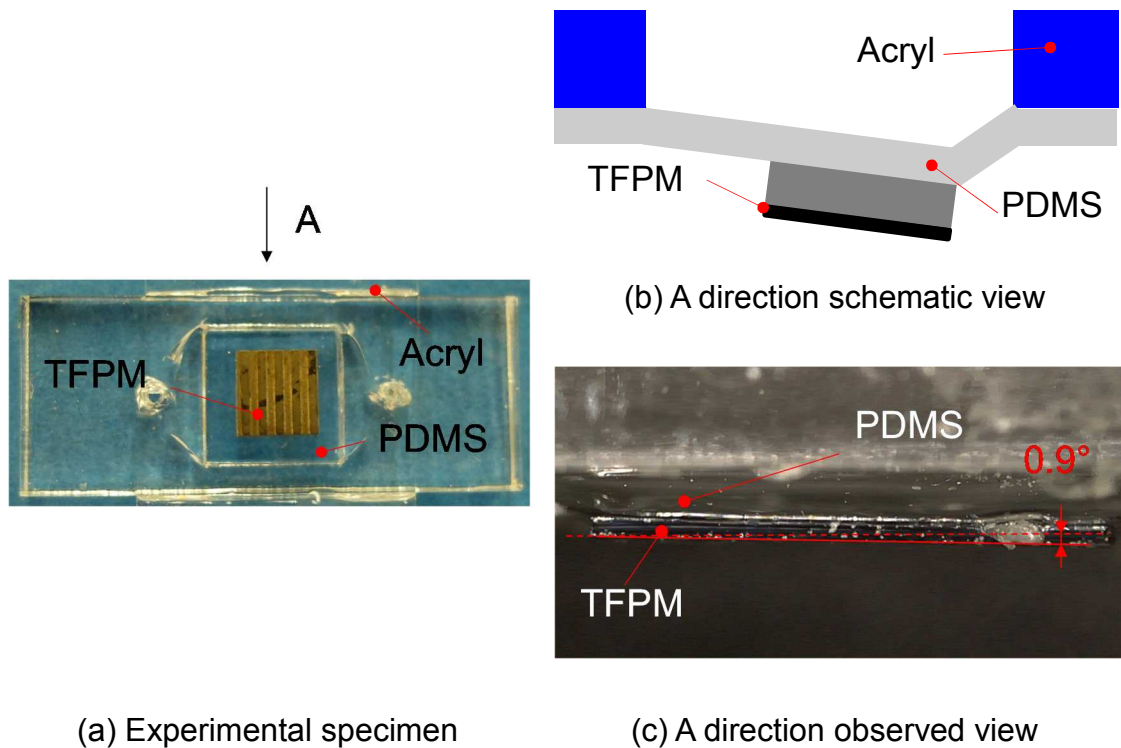


Fig. 4.44 Fabrication error evaluation (Line/space TFPM on PDMS)

The tilt motion is caused by the fabrication error of TFPM-Si substrate with PDMS diaphragm. Figure 4.44 (a) shows the fabricated specimen. The A-direction schematic view and observed view are shown in Figs. 4.44 (b, c). The TFPM-Si tilts 0.9° after fabrication. As a result, the gap between the TFPM and the micro-coil is different at each measurement point. Larger force is applied on the point which is closer to micro-coil and smaller force is applied on farther point. Thus, the displacement is different and tilt motion is generated. Furthermore, the maximum displacement of Point 2 is around $\pm 80\mu\text{m}$, which means that it touches the surface of coil insulation layer. This should be one reason of the “flat” displacement profile at Fig. 4.40. The Type 3(1) DEMA also experiences the non-uniform diaphragm displacement.

4.5 Application of the actuator to a flexible MEMS pump

4.5.1 Design of the flexible MEMS pump

The overview and parts view of the designed flexible MEMS pump are illustrated in Fig. 4.45. The total size of the pump is 20mm×20mm×1mm. It consists of a channel plate, a TFPM on a diaphragm, a coil on a substrate and tubes. In order to realize flexibility, the material of the channel plate is made of PDMS. The substrate of the coil is made of polyimide, which is also a flexible polymeric material.

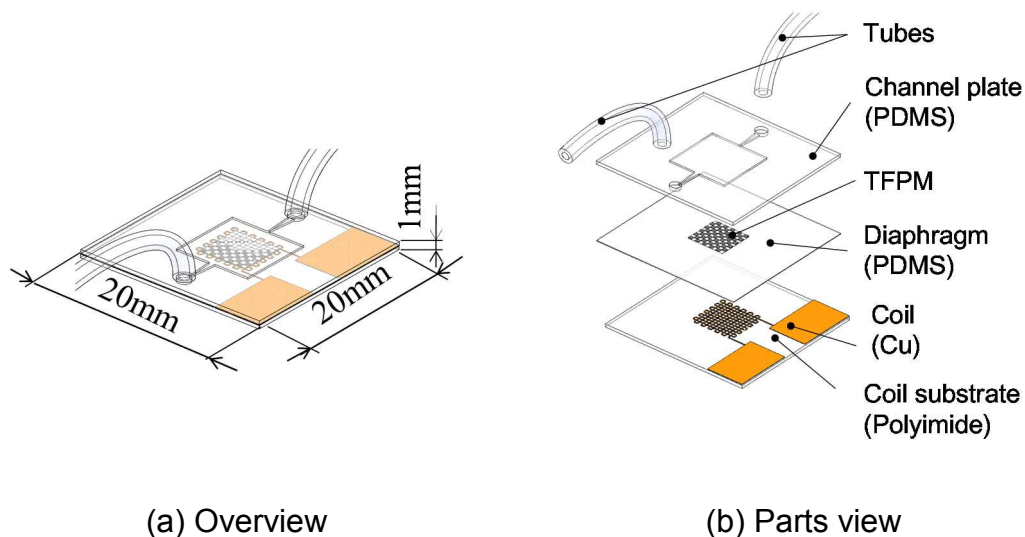


Fig. 4.45 Designed flexible MEMS pump

4.5.2 Fabrication of the flexible MEMS pump

4.5.2.1 Fabrication of PDMS channel

The flexible channel plate is made of PDMS. It is fabricated by a molding process which is an easy and fast process to realize flexible microstructure. Furthermore, PDMS is biocompatible, stable and low cost. The fabrication process is illustrated in Fig. 4.46. It consists of three main steps. The parameters

are explained as follows:

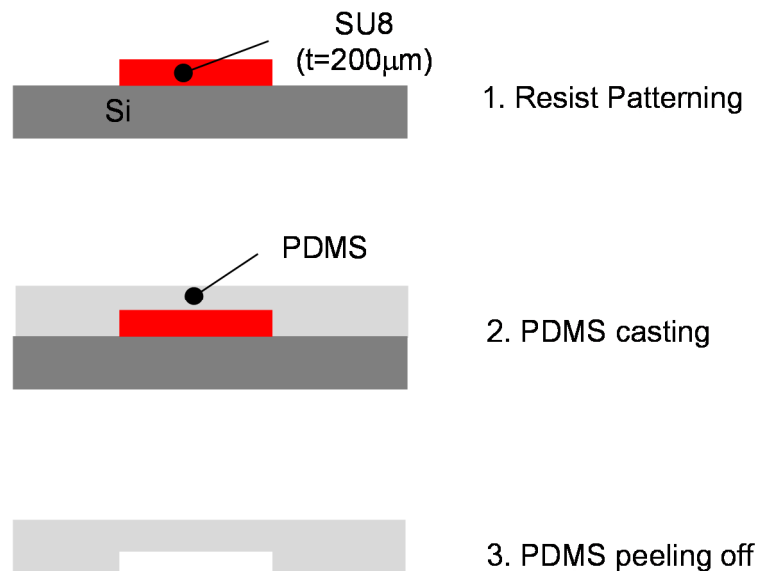


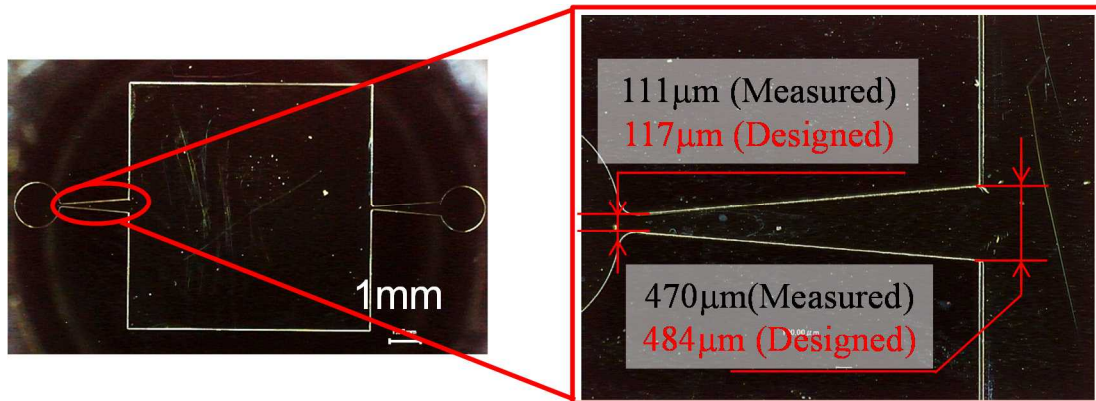
Fig. 4.46 Fabrication process of the flexible PDMS channel

(1) SU8-100 resist with a thickness of $200\mu\text{m}$ is patterned on a Si substrate. The process parameter is the same as in [55].

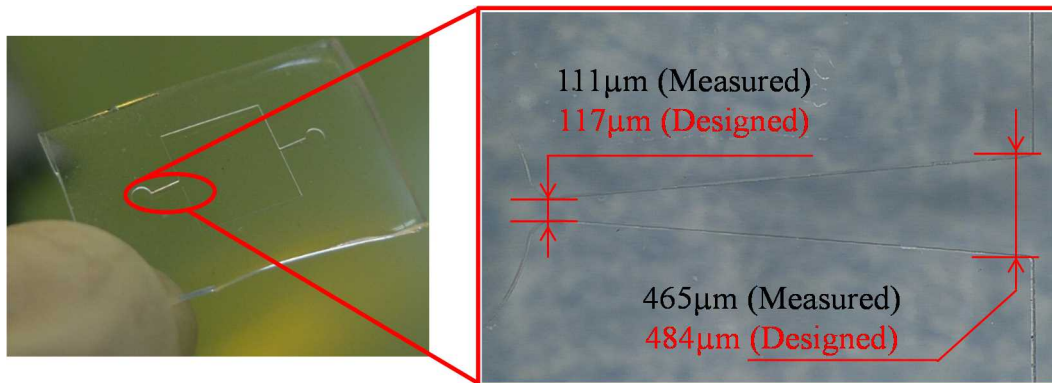
(2) Liquid PDMS is coated on the substrate. Following that, the substrate with liquid PDMS is placed in a vacuumed chamber (Asone Corp., Japan) to remove bubbles. The substrate is then placed on a hot plate to perform a curing process with curing temperature 343K and curing time 4 hours.

(3) The solid PDMS is then peeled off from the substrate.

The fabricated SU8-100 pattern on Si substrate is shown in Fig. 4.47(a). The measured throat widths of the diffuser component are very close to the designed values. The fabricated pattern on PDMS is shown in Fig. 4.47(b). The error between the design and fabrication is within $20\mu\text{m}$. The precision level is in the same order as the channel plate fabricated by wiring cutting in Chapter 2. While this molding method is faster, MEMS-based and low cost.



(a) SU8 master on Si substrate

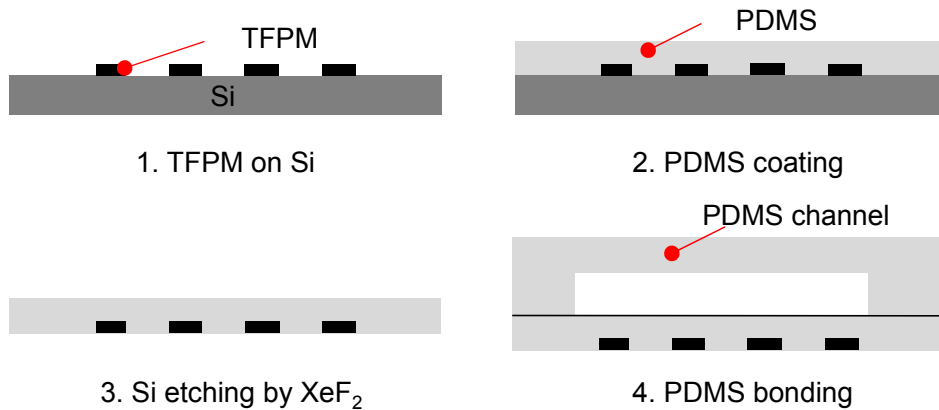


(b) Peeled-off PDMS plate

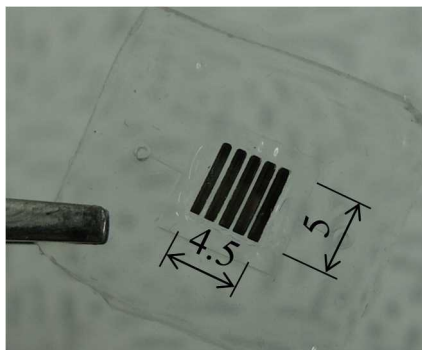
Fig. 4.47 Fabrication of PDMS channel part

4.5.2.2 Fabrication of permanent magnet pattern on PDMS diaphragm

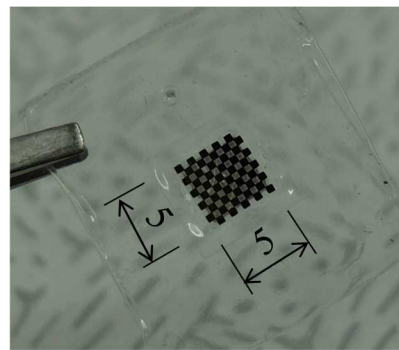
In order to fabricate the TFPM on PDMS (TFPM-PDMS) diaphragm, the method developed in Chapter 3 is utilized. The fabrication process is shown in Fig. 4.48(a). The fabricated TFPM-PDMS diaphragms are bonded with the PDMS channel which is fabricated in Section 4.5.2.1. The results are shown in Figs. 4.48(b, c).



(a) Fabrication process



(b) Line/space permanent magnet on PDMS



(c) Chessboard permanent magnet on PDMS

Fig. 4.48 Fabricated permanent magnet patterns on PDMS

The bonding of the PDMS channel and the PDMS diaphragm in Step (4) in Fig. 4.48(a) is performed by an oxygen plasma treatment device (LF-5, Mercator control systems Inc.). The process parameters are:

- Power: 5W
- Pressure: 0.104Torr
- Time: 1min

The fabrication process of TFPM with permalloy pattern (TFPM-permalloy) on PDMS diaphragm is shown in Fig. 4.49(a). In Step (3), after removing Si by XeF_2 gas, the substrates bend, as shown in Figs. 4.49(b, c).

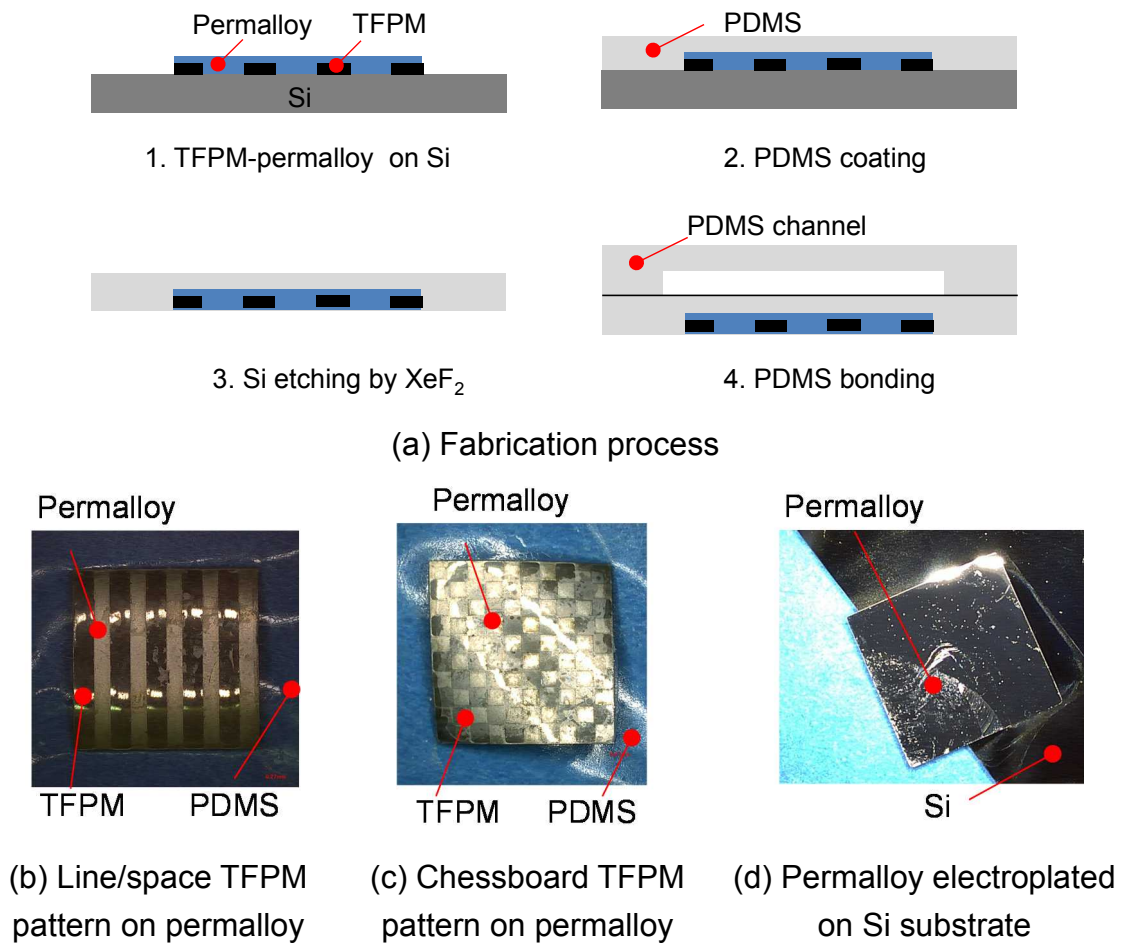


Fig. 4.49 Fabricated TFPM-permalloy patterns on PDMS

In order to evaluate the reason of the bending phenomenon, a comparison experiment is done to electroplate permalloy on a Si substrate. The electroplating process is the same as in Fig. 4.17. The fabricated permalloy is shown in Fig. 4.49(d). No observable deformation occurs. Furthermore, the temperature during the electroplating process is 313K, which generates ignorable thermal stress.

By comparing photographs in Fig. 4.49(b, c, d), it can be concluded that the deformation of the substrate is related with TFPM pattern. There are two factors concerning with TFPM's effect. The first one is magnetostriction effect. The second one is the inner stress of TFPM pattern, which releases after TFPM's isolation from Si substrate. The two factors are evaluated in the following contents.

- Magnetostriction effect

Because NiFe is a magneto-strictive material, it will expand or shrink under the magnetic field generated by TFPM during electroplating [56]. In order to test this effect, the TFPM-permalloy is heated and compared with the one without heating. The heating process is performed by a hot plate with a heating temperature of 593K. Because the Curie temperature of TFPM is 588K, TFPM will lose its magnetization above such temperature.

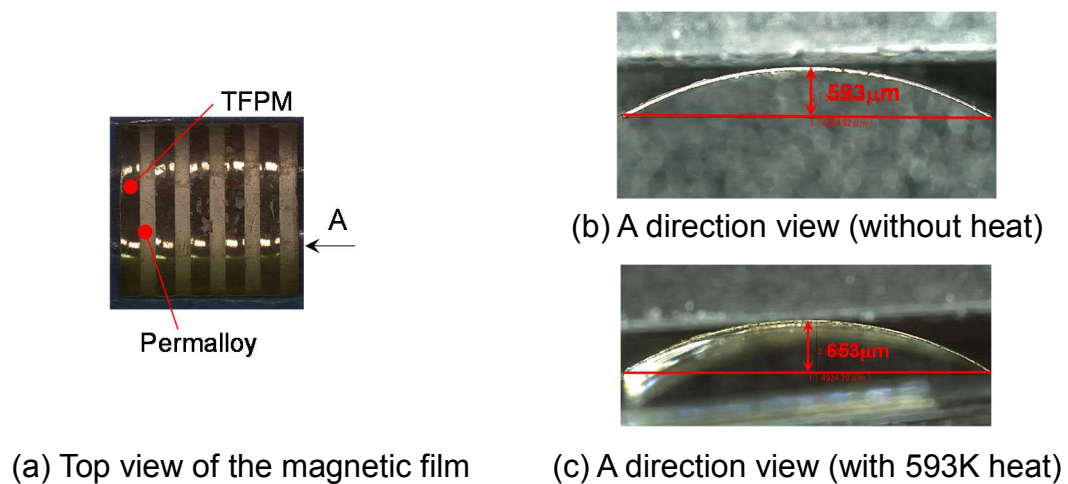


Fig. 4.50 Permalloy fabricated on TFPM substrate and Si substrate

The side views of the TFPM-permalloy film before and after heating are shown in Fig. 4.50. It clearly shows that after heating, the deformation of TFPM-permalloy film changes very little, demonstrating that magnetostriction is not the reason for the residual deformation.

- TFPM's residual stress effect

Another reason is due to the inner stress of TFPM pattern. As mentioned in Chapter 3, the TFPM is suppressed in the perpendicular direction of the magnetization after deposition on Si substrate. After removing Si, the TFPM expands, causing the bending of permalloy.

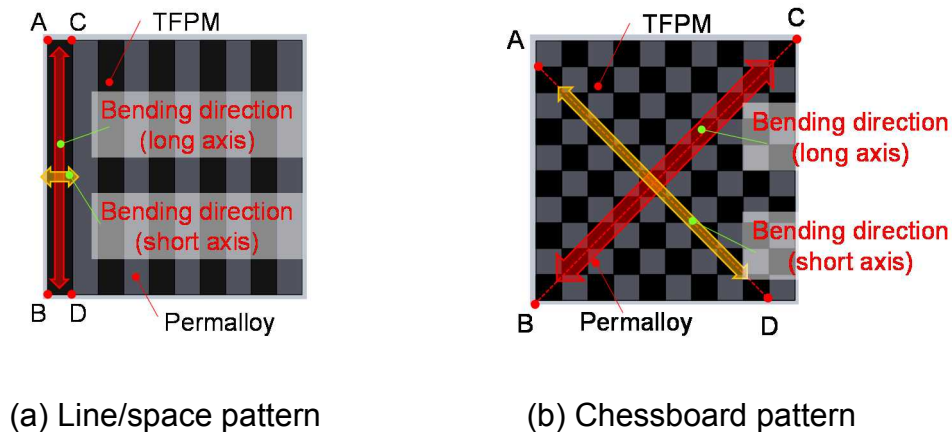


Fig. 4.51 Schematic view of TFPM pattern on permalloy

The schematic view of line/space patterned TFPM-permalloy structure is shown in Fig. 4.51(a). As TFPM's unit size is $5\text{mm} \times 0.53\text{mm}$, it should expand in the long axis direction, denoted as line AB in Fig. 4.51(a), the expanding in AB direction can explain the bending phenomenon in Fig. 4.49(b). In Fig. 4.49(c), the TFPM's unit size is $0.53\text{mm} \times 0.53\text{mm}$. The edges of the adjacent TFPM units are connected at four quarters. Thus, the TFPM pattern can be viewed as one unit. In Fig. 4.51(b), the longest line of the TFPM pattern is line BC, so the substrate should expand in BC direction. The substrate bending direction in Figs. 4.51(a, b) coincides well with the substrate in Fig. 4.49(b, c). It can be concluded that the TFPM's inner stress causes the bending of the substrate.

4.5.2.3 Fabrication of Cu coil on polyimide

Currently, the flexible polyimide substrate which is patterned with Cu circuit becomes commercially available. A custom-made flexible coil substrate sample is shown in Fig. 4.52. The polyimide film is $20\mu\text{m}$ thick, and the Cu thickness can reach $10\mu\text{m}$.

Based on the described fabrication result, the flexible MEMS pump can be realized by the following parts: flexible coil with polyimide substrate in 4.5.2.3,

flexible PDMS channel in Section 4.5.2.1 and the flexible PDMS diaphragm with TFPM patterning in Section 4.5.2.2. The prospective view is shown in Fig. 4.53.

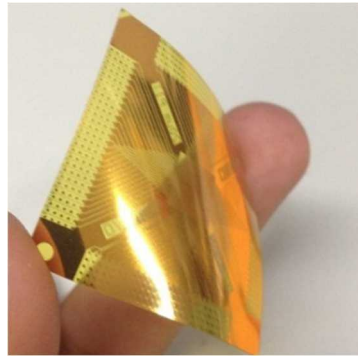


Fig. 4.52 A custom-made flexible coil sample [49]

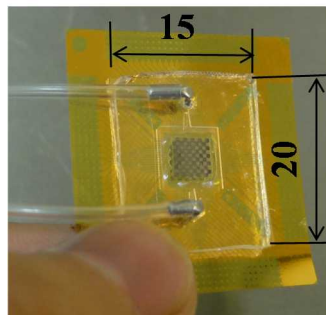
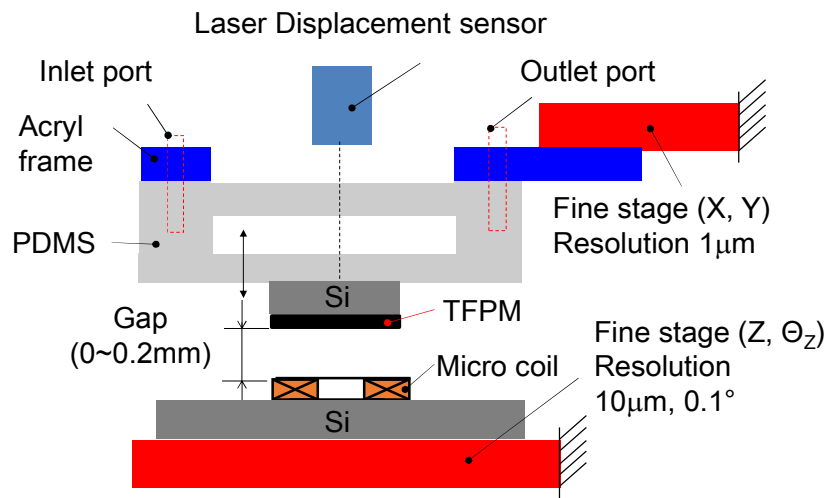


Fig. 4.53 Prospective view of the MEMS pump

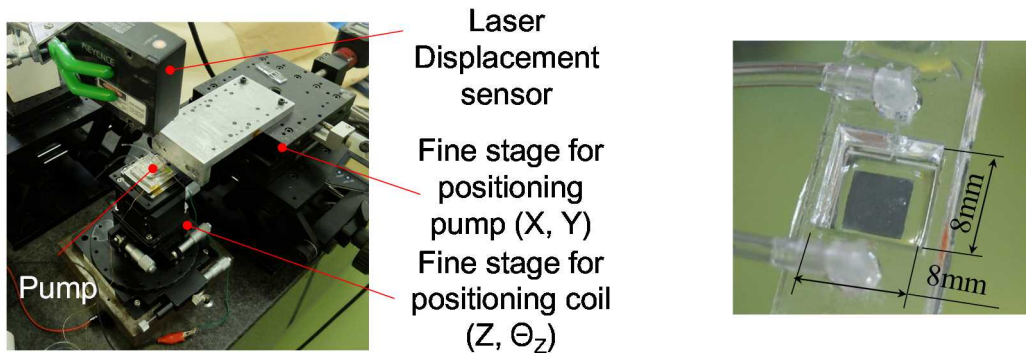
4.5.3 Evaluation of the flexible MEMS pump

To evaluate the MEMS pump performance, the flexible pump body is attached with an acrylic frame. Furthermore, as TFPM on PDMS diaphragms fabricated in Figs. 4.48(b, c) are very easy to deform and thus are very difficult to be aligned when it is driven by micro-coil, TFPM-Si substrate is utilized and is attached with PDMS diaphragm. The micro-coil on Si substrate is also utilized. The schematic evaluation setup is shown in Fig. 4.54(a).

The pump chip with acryl frame is attached with a fine stage which could adjust the position in X and Y direction with $1\mu\text{m}$ resolution. Meanwhile, the micro-



(a) Schematic evaluation setup



(b) Experimental setup

(c) Pump chip with acryl frame

Fig. 4.54 Evaluation setup of the pump performance

coil is also placed on a fine stage with a positioning resolution of $10\mu\text{m}$ in Z direction and 0.1° in Θ_z direction. Figure 4.54(b) indicates the experimental setup, and Fig. 4.54(c) shows the pump chip with acryl frame.

However, the pump could not function due to the alignment error between TFPM and micro coil. Figure 4.55(a) shows the bottom view of the evaluated pump with an enlarged view of the permanent magnet. The A direction view in Fig. 4.55(b) shows that the permanent magnet surface is not horizontal, the

misalignment angle is 1.73° in one direction. This alignment error is larger than the one that is observed in Fig. 4.44(c), Section 4.4.7. Such misalignment greatly decreases the actuator's force magnitude and the diaphragm displacement. As a result, the pump can not be actuated. To avoid the misalignment effect, special diaphragm mechanical structure or anisotropic material which has small stiffness in Z direction and large stiffness in X and Y direction should be considered.

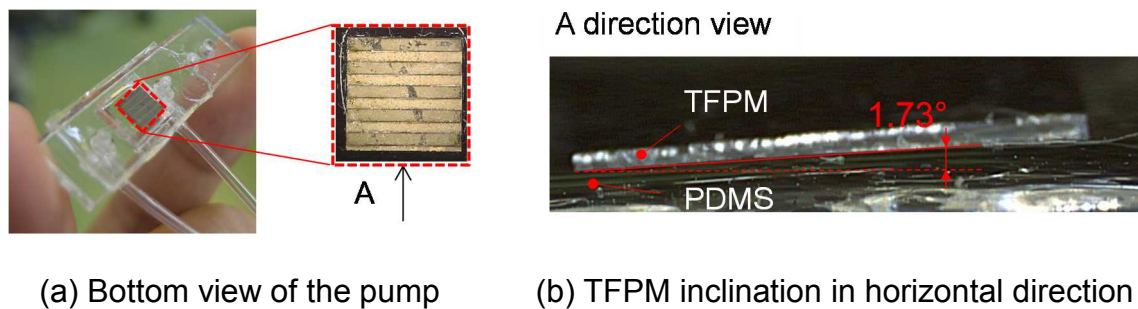


Fig. 4.55 Reason of the pump's malfunction

4.6 Further enhancement of the actuator's force

This section is to explore the possibility of further enhancing the force magnitude of the micro electromagnetic actuator. The solutions to enhance the force are based on alternate magnetization of TFPM and scaling down of the permanent magnet's feature size.

4.6.1 Alternate magnetization of TFPM

In Section 4.2, the TFPM is segmented into line/space or chessboard pattern to enhance the magnetic flux density. However, the spaces between the adjacent permanent magnets are not effectively utilized. If the spaces are replaced with permanent magnets that have opposite magnetization direction, the generated magnetic flux density at the surface can be doubled. To evaluate the above effect, alternately magnetized TFPM with stripe pattern is designed in Fig. 4.56.

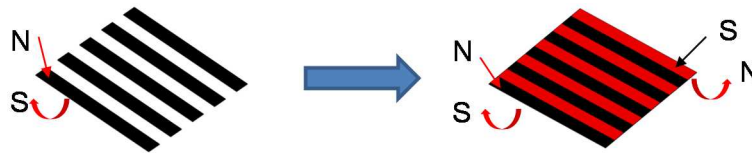


Fig. 4.56 Segmented permanent magnets and the alternately magnetized one

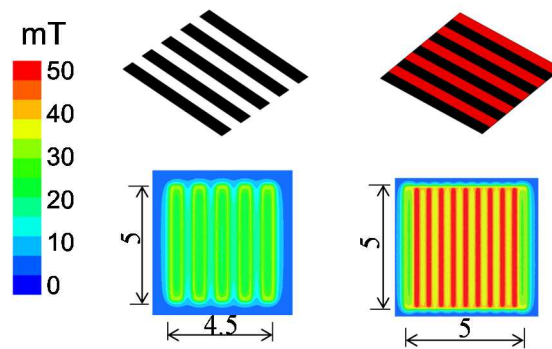


Fig. 4.57 Surface magnetic flux density comparison
(L/S segmented permanent magnets V.S. alternately magnetized one)

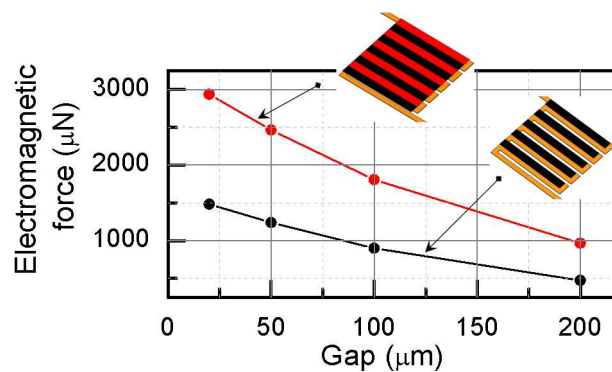


Fig. 4.58 Electromagnetic force comparison
(1A current input into coil)

The surface (100μm above the permanent magnet surface) magnetic flux density magnitude generated by the two types permanent magnet pattern are compared in Fig. 4.57. The magnetic flux density generated by the alternately magnetized permanent magnet almost doubles the one generated by line/space type.

The force generated by the actuators are compared in Fig. 4.58. The actuator with alternate magnetization doubles the force. In the same way, it can be speculated that alternate magnetization also works for chessboard pattern.

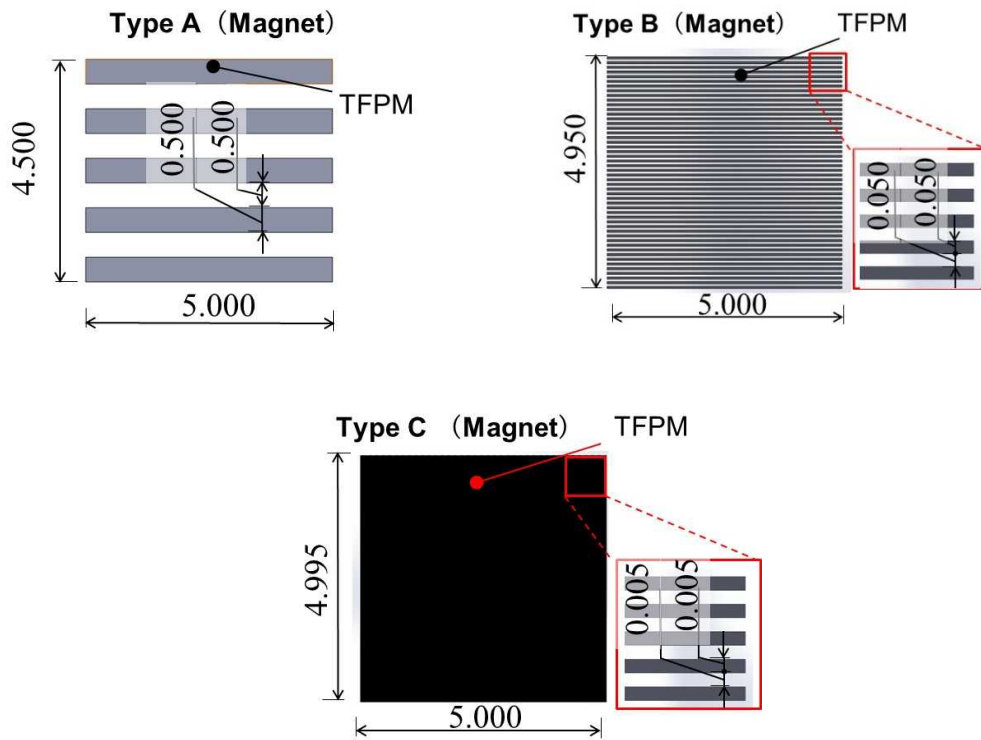


Fig. 4.59 Proposal of line/space permanent magnets

4.6.2 Scaling down of the permanent magnet feature size

In section 4.2, the force of planar micro electromagnetic actuator was enhanced due to the segmentation of the TFPM. The self-demagnetization effect is suppressed. This section is to explore the phenomenon when the feature size of the segmentation is further scaled down.

Line/space TFPM pattern is utilized to demonstrate this size effect. The TFPM's total size is $5\text{mm} \times 5\text{mm} \times 10\mu\text{m}$. TFPM's unit size are $0.5\text{mm} \times 5\text{mm} \times 10\mu\text{m}$, $0.05\text{mm} \times 5\text{mm} \times 10\mu\text{m}$ and $0.005\text{mm} \times 5\text{mm} \times 10\mu\text{m}$, respectively. The TFPM's configurations are illustrated in Fig. 4.59, and they are denoted as Type A, Type

B and Type C.

Meanwhile, meander coils are also designed accordingly with feature pitch size of 0.5mm, 0.05mm and 0.005mm, respectively. The designed models of micro-coil are shown in Fig. 4.60.

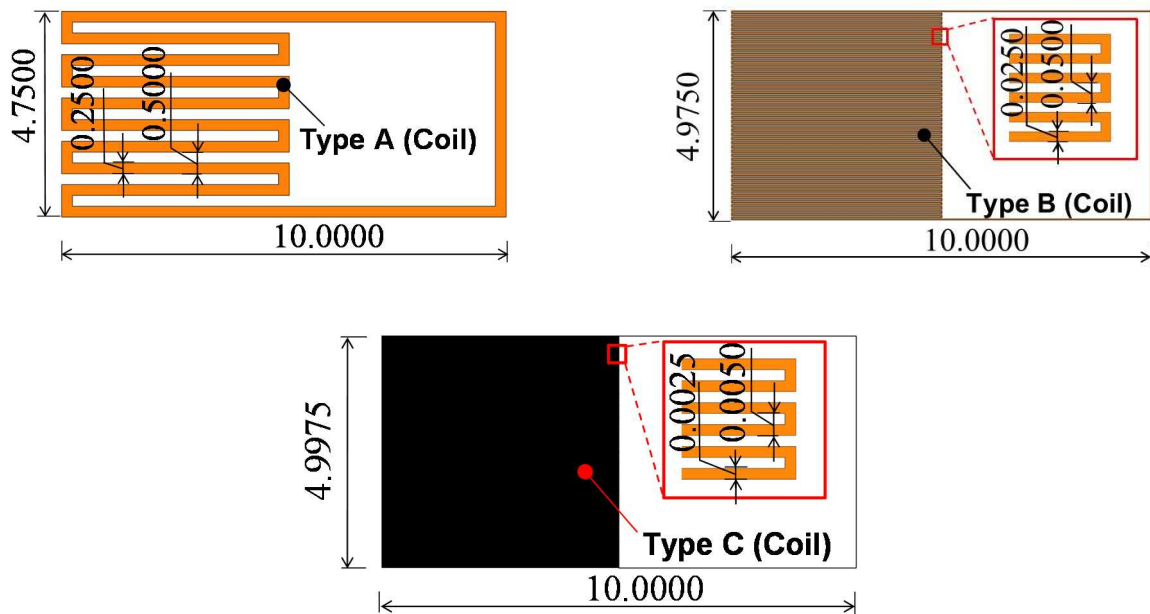


Fig. 4.60 Proposal of meander micro-coil with different pitch size

The maximum current density that can be input into the coil stably is around 10A/mm^2 , which is an empirical value in the conventional electromagnet design. For micro-coil design, the admissible current density is increased due to the large surface to volume ratio, which could efficiently transfer and conduct heat. Furthermore, the substrates for planar micro-coil deposition are usually made of Si, which is a good heat conductor with a heat conductivity of $130\text{ W/(m}\cdot\text{K)}$ as well as metal. Thus, the admissible current density in the microsystems increases to the order of $10^3\text{-}10^5\text{ A/mm}^2$ [57]. In the following simulation, the maximum stable current densities input into the coil are 100A/mm^2 for Type B coil and 1000A/mm^2 for Type C coil.

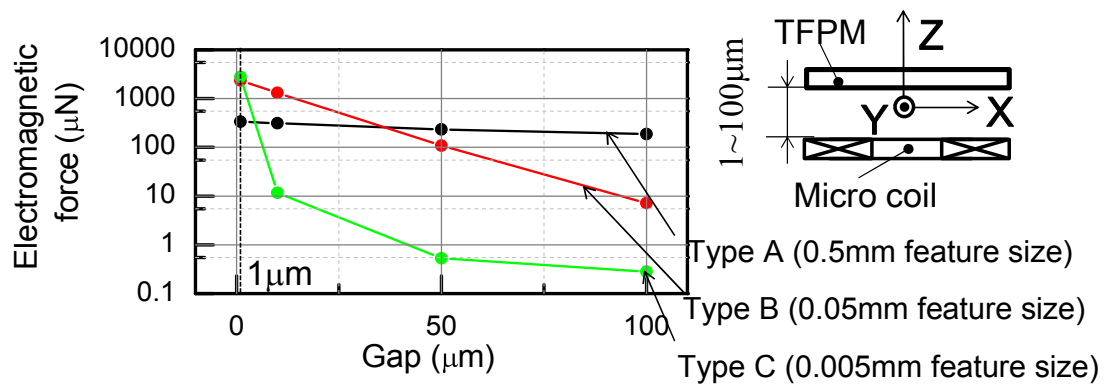


Fig. 4.61 Electromagnetic force comparison in simulation

Figure 4.61 shows the simulation results. The gap between the coil and the TFPM patterns ranges from 1 to 100 μm . For Type A actuator, it can generate 330 μN force at 1 μm gap, and the force decreases to 180 μN when the gap is 100 μm . For Type B actuator, the force reaches 2300 μN at 1 μm gap. The force decreases to around 7 $\mu\text{N/m}$ when the gap increases to 100 μm . For Type C actuator, the force is 2800 μN at 1 μm gap. The force then decreases to 0.3 μN at 100 μm gap.

From the simulation above, the following conclusions can be made:

1. As the feature size of TFPM decreases, the generated force increases due to the suppression of the demagnetization effect and the increase of current density.
2. When the feature size of the TFPM is scaled down, the actuator's effective working distance in which large force is generated decreases.

4.7 Conclusion

4.7.1 Summary

In this chapter, researches related with planar type micro electromagnetic actuators and flexible MEMS pump were performed. High force/energy density planar electromagnetic actuators fabricated by MEMS-based processes were realized. Flexible MEMS pump was fabricated. The following conclusions could be reached.

1. Chessboard and line/space pattern of permanent magnets were originally proposed. Mesh type and meander type micro-coils were designed accordingly. After segmentation of the TFPM, the self-demagnetization factor decreases. The force of the proposed actuators were several times higher than the convention spiral shape coil and non-segmented permanent magnet, provided the gap between the permanent magnet and coil was less than 200 μ m. The force/energy density of the proposed actuator was superior to previous micro planar electromagnetic actuators or bulk electromagnetic actuators. Furthermore, the proposed structures all have 2D structures and thus could be easily fabricated by MEMS-based fabrication process.

2. The actuators' force were further enhanced by covering a ferromagnetic layer on the surface of TFPM pattern. Permalloy was selected as the ferromagnetic layer due to its easy fabrication process.

3. The experimentally measured forces were between 70% and 90% of the simulated results due to alignment errors between the segmented permanent magnet patterns and the micro-coils. Furthermore, simulation showed that alignment errors have little effect on conventional actuators.

4. The fabricated actuators were utilized to drive a flexible and transparent MEMS pump. The flexible micro pump was fabricated using MEMS process. Unfortunately, the pump could not function due to the alignment error between

TFPM and micro-coil. The inner stress between TFPM and permalloy bended the structure, degrading the actuator's performance.

5. Simulation of alternate magnetization and scaling down of permanent magnets pattern were performed. The actuator's force could be doubled by alternate magnetization. The actuator's force could also be enhanced by decreasing the feature size. Meanwhile, the requirement for positioning became more precise to generate a larger force.

4.7.2 Future work

The electromagnetic actuators proposed in this chapter possess the characteristic of large force, which could be utilized in micro motors, micro levitators or other micro devices in the future work.

Another future work of this chapter should be concentrated on avoiding the misalignment effect on the actuator's performance. Special mechanical structure or anisotropic material which has large stiffness in one direction and small stiffness in other directions should be proposed or utilized to avoid the alignment error.

Chapter 5 Conclusion and future work

5.1 Conclusions

Towards the research objective of “Fabrication and Application of Micro Diaphragm-type Electromagnetic Actuators Utilizing Thin Film Permanent Magnet”, this thesis realized several achievements.

In Chapter 2, a micro DEMA utilizing a TFPM and closed loop iron-cored electromagnet was realized and applied to drive a diffuser valveless pump. The TFPM was 3mm in diameter and 20 μ m in thickness, fabricated by MEMS-based sputtering process. The DEMA attained 28mN/A force and 500 μ m displacement. The pump realized a maximum flow rate of 50 μ L/min by applying a square voltage signal with a peak to peak amplitude of 16V at a frequency of 10Hz. A maximum pressure of 110Pa was reached at the same condition. The pump achieved bubble tolerance and self-priming due to the large diaphragm displacement (~500 μ m).

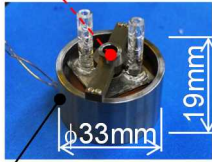
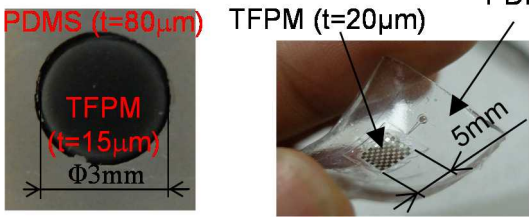
In Chapter 3, a fully MEMS-based fabrication process which enabled the integration of a sputtered TFPM on a PDMS diaphragm was proposed. Si was used as a sacrificial layer during TFPM sputtering and was thoroughly etched by a XeF₂ etching process. The substrate temperature during XeF₂ etching process, the magnetic performance of the TFPM and the mechanical properties of the PDMS were evaluated, respectively. The XeF₂ etching process temperature could be adjusted by controlling the XeF₂ etching pressure. The fabricated magnetic diaphragm retained its profile, mechanical property and magnetic properties.

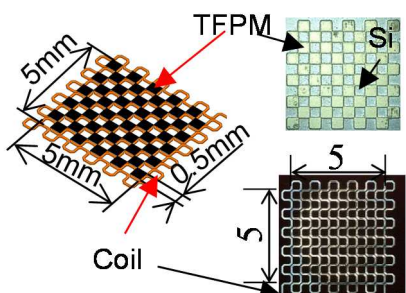
In Chapter 4, planar type micro electromagnetic actuators with high force density and energy density were proposed. Several TFPM patterns such as chessboard and line/space pattern were originally proposed. Mesh type and meander type micro-coils were designed accordingly to drive these patterned

TFPM effectively. The generated force of the proposed actuators are several times higher than conventional spiral shape coil and non-segmented permanent magnet. Ferromagnetic layers above the surface of TFPM patterns were proposed to enhance the force of the actuators. The proposed actuators were fabricated and evaluated. The experimentally measured forces were between 70% and 90% of the simulated results due to alignment errors between the TFPM and the micro-coil. The proposed actuator exhibits superior force/energy density to previous planar micro electromagnetic actuator or bulk electromagnetic actuator. The fabricated actuators were utilized to drive a flexible and transparent MEMS pump. Currently, the pump could not function due to the alignment error between the TFPM and micro-coil. The actuator's force could be further improved by alternate magnetization and decreasing the feature size of permanent magnet pattern.

The summary of the main research achievements are shown in the following table.

Table 5.1 Summary of the research achievement in this thesis

<p>1. Closed electromagnetic actuator (Chapter 2)</p>	<p>TFPM($\Phi 3\text{mm} \times 20\mu\text{m}$)</p>  <p>Electromagnet</p>	<p>DEMA: 35mN/A, 500μm Pump: 50$\mu\text{L}/\text{min}$, 110Pa</p>
<p>2. TFPM integration with PDMS (Chapter 3)</p>	 <p>PDMS ($t=80\mu\text{m}$) TFPM ($t=15\mu\text{m}$) $\Phi 3\text{mm}$</p> <p>PDMS TFPM ($t=20\mu\text{m}$) 5mm</p>	<p>Flexible magnetic diaphragm</p>

<p>3.High force/energy density micro electromagnetic actuator (Chapter 4)</p>	 <p>The diagram illustrates a micro electromagnetic actuator structure. It features a TFPM (Thin Film Piezoelectric Material) layer on a Si (Silicon) substrate. A coil is positioned below the TFPM layer. Dimensions are indicated: the TFPM layer is 5mm wide, the coil pitch is 0.5mm, and the coil width is 5. The coil is shown as a series of small squares, and the TFPM layer is shown as a grid of small squares.</p>	<p>20 times larger force/energy density of conventional design</p>
--	---	--

5.2 Future works

The alignment problem between TFPM and micro coil which was generated in Chapter 4 should be solved in the future work. Proper package between TFPM and micro coil is necessary to avoid the alignment errors in the required directions.

The developed technology can be applied for many devices such as energy harvesting devices, micro magnetic levitation systems and so on.

References

- [1] Status of the MEMS Industry report, April 2014, Yole Development
- [2] A. Olsson, "Valve-less Diffuser Micropumps", Ph.D. Thesis, Royal Institute of Technology, 1998
- [3] T. Zhang and Q. Wang, "Valveless piezoelectric micropump for fuel delivery in direct methanol fuel cell (DMFC) devices", Journal of Power Sources 140, pp. 72-80, 2005
- [4] N. Wang, "Fabrication and integration of permanent magnet materials into MEMS transducers", Ph. D. Thesis, University of Florida, 2010
- [5] J. Streque, A. Talbi, P. Pernod, and V. Preobrazhensky, "New Magnetic Microactuator Design Based on PDMS Elastomer and MEMS Technologies for Tactile Display", IEEE TRANSACTIONS ON HAPTICS 3(2), pp. 88-97, 2010
- [6] R. Zengerle, S. Kluge, M. Richter and A. Richter, "A Bidirectional Silicon Micro pump", IEEE, pp. 19-24, 1995
- [7] S. K. Pandey, A.R. James, C. Prakash, T.C. Goel and K. Zimik, "Electrical properties of PZT thin films grown by sol-gel and PLD using a seed layer", Materials Science & Engineering B 112, pp. 96-100, 2004
- [8] K. Kim, H. Yoon, O. Jeong and S. Yang, "Fabrication and test of a micro electromagnetic actuator", Sensors and Actuators A 117, pp. 8-16, 2005
- [9] Y. Zhou and Farid Amirouche, "An Electromagnetically-Actuated All-PDMS Valveless Micropump for Drug Delivery", Micromachines 2, pp. 345-355, 2011
- [10] O. Cugat, J. Delamare and G. Reyne, "Magnetic Micro-Actuators and Systems (MAGMAS)", IEEE TRANSACTIONS ON MAGNETICS 39(5), pp.

3607-3612, 2003

- [11] D. P. Arnold and N. Wang, "Permanent Magnets for MEMS", JOURNAL OF MICROELECTROMECHANICAL SYSTEMS 18(6), pp. 1255-1266, 2009
- [12] S. Guan and B. J. Nelson, "Electrodeposition of low residual stress CoNiMnP hard magnetic thin films for magnetic MEMS actuators", Journal of Magnetism and Magnetic Materials 292, pp. 49–58, 2005
- [13] Y. Su, H. Wang, G. Ding, F. Cui, W. Zhang and W. Chen, "Electroplated Hard Magnetic Material and Its Application in Microelectromechanical Systems", IEEE TRANSACTIONS ON MAGNETICS 41(12), pp. 4380-4383, 2005
- [14] M. Nakano, S. Sato, H. Fukunaga, and F. Yamashita, "A method of preparing anisotropic NdFeB film magnets by pulsed laser deposition", JOURNAL OF APPLIED PHYSICS 99, 08N301, 2006
- [15] M. Uehara, "Microstructure and permanent magnet properties of a perpendicular anisotropic NdFeB/Ta multilayered thin film prepared by magnetron sputtering", Journal of Magnetism and Magnetic Materials 284, pp. 281–286, 2004
- [16] N. M. Dempsey, A. Walther, F. May, D. Givord and K. Khlopkov, "High performance hard magnetic NdFeB thick films for integration into micro-electro-mechanical systems", APPLIED PHYSICS LETTERS 90, 092509, 2007
- [17] M. Uehara and T. Shinshi, "Characteristics of Nd-Fe-B/Ta Multilayered Permanent Magnet Thin-films and Their Application to Magnetic Devices", Hitachi Metals Technical Review 28(14), pp. 14-19, 2012
- [18] W.F. Liu, S. Suzuki and K. Machida, "Magnetic properties of Nd–Fe–B film

- magnets prepared by RF sputtering”, *Journal of Magnetism and Magnetic Materials* 308, pp. 126-130, 2007
- [19] M. Nakano, S. Shibata, T. Yanai and H. Fukunaga, “Anisotropic properties in Fe-Pt thick film magnets”, *JOURNAL OF APPLIED PHYSICS* 105, 07A732, 2009
 - [20] B. Pawlowski, J. T. Opfer, “Permanent magnetic NdFeB thick films”, *JOURNAL OF MATERIALS SCIENCE* 39, pp. 1321-1324, 2004
 - [21] Naigang Wang and David P. Arnold, “Thick Electroplated Co-Rich Co-Pt Micromagnet Arrays for Magnetic MEMS”, *IEEE TRANSACTIONS ON MAGNETICS* 44 (11), pp. 3969-3972, 2008
 - [22] W. K. Schomburg, R. Ahrens, W. Bather, S. Engemam, P. Krehl and J. Martin, “Long-Term Performance Analysis of Thermo-Pneumatic Micropump Actuators”, 1997 International Conference on Solid-State Sensors and Actuators, Chicago, 76-79, 1997
 - [23] M. Shena, L. Dovat and M.A.M. Gijs, “Magnetic active-valve micropump actuated by a rotating magnetic assembly”, *Sensors and Actuators B*, 154, pp. 52-58, 2011
 - [24] C. Yamahata, F. Lacharme and M. A. M. Gijs, “Glass valveless micropump using electromagnetic actuation”, *Microelectronic Engineering* 78–79, pp. 132–137, 2005
 - [25] C. Yamahata, C. Lotto, E. Al-Assaf and M. A. M. Gijs, “A PMMA valveless micropump using electromagnetic actuation”, *Microfluid Nanofluid* 1, pp. 197-207, 2005
 - [26] A. Feustel, O. Krusemark, J. Miiller, “Numerical simulation and optimization of planar electromagnetic actuators”, *Sensors and Actuators A* 70, pp. 276-282, 1998

- [27] C. Lee, H. Chang and C. Wen, "A MEMS-based valveless impedance pump utilizing electromagnetic actuation", *J. Micromech. Microeng.* 18, 035044, 2008
- [28] M. A. Hopcroft, W. D. Nix and T. W. Kenny, "What is the Young's Modulus of Silicon?", *JOURNAL OF MICROELECTROMECHANICAL SYSTEMS* 19(2), 2010
- [29] MEMS net Home, <https://www.memsnet.org/material/siliconsibulk-/?keywords=Si>
- [30] Material Property Database, Polyimide, <http://www.mit.edu/~6.777/matp-rops/polyimide.htm>
- [31] N. Suzuki, S. Kiba, Y. Kamachi, N. Miyamoto and Y. Yamauchi, "Mesoporous silica as smart inorganic filler: preparation of robust silicone rubber with low thermal expansion property", *J. Mater. Chem.*, 21, pp. 5338-5344, 2011
- [32] M. H. Lu and Y. P. Zheng, "Indentation test of soft tissues with curved substrates: A finite element study", *Medical & Biological Engineering & Computing* 42, pp. 535-540, 2004
- [33] M. Liu, J. Sun and Q. Chen, "Influences of heating temperature on mechanical properties of polydimethylsiloxane", *Sensors and Actuators A* 151, pp. 42-45, 2009
- [34] R. S. Mottram, A. J. Williams and I. R. Harris, "The effects of blending additions of copper and cobalt to $\text{Nd}_{16}\text{Fe}_{76}\text{B}_8$ milled powder to produce sintered magnets", *Journal of Magnetism and Magnetic Materials* 234, pp. 80-89, 2001
- [35] M. Richter, R. Linnemann and P. Woias, "Robust design of gas and liquid micropumps", *Sensors and Actuators A* 68, pp. 480-486,

1998

- [36] Y. Jiang, T. Fujita, M. Uehara, D. Zhang, J. Cai, K. Higuchi and K. Maenaka, "Characterization of Mechanical Properties of Cantilevered Nd₂Fe₁₄B/Ta Magnetic Microstructures", Applied Physics Express 4,116401, 2011
- [37] B. Behkam and M. Sitti, "Bacterial Propulsion of Chemically Patterned Micro-Cylinders", Proceedings of the 2nd Biennial IEEE/RAS-EMBS International Conference on Biomedical Robotics and Biomechatronics, Scottsdale, AZ, USA, pp. 753-757, 2008
- [38] F. I. Chang, R. Yeh, G. Lin, P. B. Chu, E. Hoffman, E. J. J. Kruglick, and K. S.J. Pister, "Gas-phase silicon micromachining with xenon difluoride", SPIE Vol. 2641, pp. 117-123, 1995
- [39] "Infrared Thermometry- Understanding and using the Infrared Thermometer", http://www.calex.co.uk/downloads/application_guidance-/understanding_and_using_ir.pdf
- [40] Sigma Koki Co. LTD., http://www.sigma-koki.com/pages/guide/B_optical-data-2_jp.php
- [41] Y. Su and W. Chen, "Investigation on Electromagnetic Microactuator and Its Application in Micro-Electro-Mechanical System (MEMS)", Proceedings of the 2007 IEEE International Conference on Mechatronics and Automation, Harbin, China, pp. 3250-3254, 2007
- [42] C. Lee and Z. Chen, "Valveless impedance micropump with integrated magnetic diaphragm", Biomed Microdevices 12, pp. 197-205, 2010
- [43] E-Magnets UK, Co., Ltd., <http://www.ndfeb-info.com/characteristics.aspx3>
- [44] M. Ke, J. Zhong, and C. Lee, "Electromagnetically-Actuated Reciprocating Pump for High-Flow-Rate Microfluidic Applications", Sensors, 12, pp. 13075-13087, 2012

- [45] C. Lee, H. Chang and C. Wen, "A MEMS-based valveless impedance pump utilizing electromagnetic actuation", J. Micromech. Microeng. 18, 035044, 2008
- [46] B. D. CULLITY and C. D. GRAHAM, "INTRODUCTION TO MAGNETIC MATERIALS", 2nd edition, IEEE press, pp. 48-55, 2009
- [47] D. Kim, J. Ahn, W. Choi, H. Kim, T. Kim, J. Song, Y. Huang, Z. Liu, C. Lu, J. A. Rogers, "Stretchable and Foldable Silicon Integrated Circuits", SCIENCE 320(25), pp. 507-511, 2008
- [48] M. Kaltenbrunner, T. Sekitani, J. Reeder, T. Yokota, K. Kuribara, T. Tokuhara, M. Drack, R. S. Diauer, I. Graz, S. B. Gogonea, S. Bauer and T. Someya, "An ultra-lightweight design for imperceptible plastic electronics", NATURE, 499, pp. 458-463, 2013
- [49] Sanyo Co. LTD., <http://www.wsanyo.jp/>
- [50] A. Aharoni, "Demagnetizing factors for rectangular ferromagnetic prisms", JOURNAL OF APPLIED PHYSICS 83(6), pp. 3432-3434, 1998
- [51] R. M. Bozorth, Ferromagnetism, IEEE Press, New York, pp. 109, 1951
- [52] Tape-Wound-Core-Hysteresis-Loops, Magnetics. Butler, PA, pp. 35
- [53] Manual of SU8 (2-25), http://www.microchem.com/pdf/SU8_2-25.pdf
- [54] LG Electronics, http://www.lg.com/jp/mobile-phones/promotion/G_Flex_L-GL23/index.html
- [55] Manual of SU8 (50-100), http://www.microchem.com/pdf/SU8_50-100.pdf
- [56] L. W. McKEEHAN and P. P. CIQFFI, "MAGNETOSTRICTION IN PERMALLOY", Physical Review 28, pp. 146-157, 1926
- [57] J. Liu, E. Fullerton, O. Gutfleisch and D. J. Sellmyer, "Nanoscale Magnetic

Materials and Applications”, Springer Press, NY, pp. 664, 2009

- [58] J. Namkung, M.C. Kim, C. G. Park, “Effect of Si addition on the magnetic properties of melt-quenched Ni-Fe alloy strip”, *Materials Science and Engineering A* 449-451, pp. 430-434, 2007
- [59] M. Uehara, “Improved Perpendicular Anisotropy and Permanent Magnet Properties in Co-Doped Nd-Fe-B Films Multiplayered With Ta”, *IEEE TRANSACTIONS ON MAGNETICS*, 41 (10), pp. 3838-3843, 2005
- [60] D. M. Kirkwood, G. Pattanaik and G. Zangari, “Electrodeposited CoNiP Films with Perpendicular Magnetic Anisotropy”, *Journal of The Electrochemical Society* 154 (8), pp. 363-36-8, 2007
- [61] Japan Sensor Corp, JSC-3, <http://www.japansensor.co.jp/products/popup/download/blackpaint.pdf>
- [62] Hitachi Metals, Co., Ltd., <https://www.hitachi-metals.co.jp/index.html>
- [63] Nippon Signal, Co., Ltd., <http://www.signal.co.jp/vbc/mems/>
- [64] Arnold, Magnetic Technologies, SMMA Fall Technical Conference
- [65] J. Kestin, M. Sokolov and W. A. Wakeham, “Viscosity of Liquid Water in the Range -8°C to 150°C”, *J. Phys. Chem. Ref. Data* 7 (3), pp. 941-948, 1978
- [66] M. J. Assael and S. K. Polimatidou, “Measurement of the viscosity of Alcohols in the Temperature range 290-340K at Pressures up to 30MPa”, *International Journal of Thermophysics* 15(1), pp. 95-107, 1994
- [67] E. Stemme and G. Stemme, “A valveless diffuser/nozzle-based fluid pump”, *Sensors and Actuators A* 39, pp. 159-167, 1993
- [68] HyperPhysics, <http://hyperphysics.phy-astr.gsu.edu/hbase/tables/magprop.html#c2>

- [69] Y. C. Chen, W. L. Tseng and C. H. Lin, "PDMS-based Optical Leaky Waveguide Coated with Self-assemble Au-NPs for Bio-analytical Detections", *Bio-Inspired Sensing and Actuation* 2 (1), pp. 63-68, 2012
- [70] P. E. Cavarec, H. B. Ahmed and B. Multon, "Force Density Improvements from Increasing the Number of Airgap Surface in Synchronous Linear Actuators", *IEE Proc-Elec. Power Appl.* Vol.150, n°1, pp.106-120, 2003
- [71] R. J. Wood, E. Steltz and R. S. Fearing, "Optimal energy density piezoelectric bending actuators", *Sensors and Actuators A* 119, pp. 476–488, 2005
- [72] J. Stohr and H. C. Siegmann, "Magnetism: From Fundamentals to Nanoscale Dynamics", Springer press, p. 50, 2009

Acknowledgements

I would like to personally thank the following people who supported me with my sincere gratitude.

First, I want to express my sincere gratitude to my supervisor, Prof. Tadahiko SHINSHI. I received much instruction from Professor SHINSHI. From him, I know the way to do research and the way to solve problems. Professor SHINSHI encouraged me a lot and gave me much confidence. I also received much training about how to write academic articles and how to do academic presentation. These experiences would be unforgettable in my life forever. It is also my fortune to meet a good supervisor who does what a “Supervisor” should do. I wish Professor Shinshi healthy and happy.

I want to express my gratitude to my doctor thesis examiners:

Professor Haruo HOUJOH, Professor Yoshiharu KAGAWA, Professor Takeshi HATSUZAWA, Professor Kazuhiro YOSHIDA

I also express gratitude to Professor Rongqiang LIU in Harbin Institute of Technology and Professor Xiaoyou ZHANG in Nippon Institute of Technology for helping me entered Tokyo Tech, and for their valuable advices and orientations in my study and life.

I here express special gratitude to Mr. Uehara, who was an engineering in Hitachi Metals Company. In my research, Mr. Uehara helped me a lot in sputtering the TFPM and taught me a lot in the magnetic property of TFPM. I am also grateful to the staff of Semiconductor and MEMS Processing Center, Precision Laboratory's Factory and Mono-tsukuri Center in Tokyo Institute of Technology, Nano Technology Research Laboratory (NTRC) in Waseda University, Japan Sensor Corporation and Tokyo Metropolitan Industrial Technology Research Institute.

Thanks are due to Dr. Junpei SAKURAI, Assistant Professor Wataru HIJIKATA, Dr. Atsushi YUMOTO, Dr. Dongjue HE, Dr. Yoshitaka UYEYAMA, Dr. Hechang LEI, Dr. Xiao ZHANG and Mr. Masato ISHIBASHI for their instruction about MEMS, physics and mechanical engineering.

Thanks are due to Mr. Yoshihiro MORIMOTO for his help, friendship and instruction of P&D. Thanks to Mr. Ryogen FUJIWARA for his inspiring discussion, kindly advices and precious time in checking my E-mail in Japanese.

I also want to express my gratitude to Miss SUN, Mr. Jun RAO, Mr. Gentai SAHARA, Mr. Takatori SHIMADA, Mr. Daisuke KATSUMATA, Mr. Yuki SUZUMORI, Mr. Wataru TSUNODA, Mr. Tatsuhiko KAMIYA, Mr. Kouta TOMIOKA, Mr. Fumiya TAKAHASHI, Mr. Greed, and Mr. Thomas for their friendship and pleasure time together.

Thanks are due to Mr. Atsushi SHINOHARA, Miss Yue WANG, Miss Zi YAN, Mr. Bin XIE, Mr. Yingdi HE and Mr. Richard GU for their precious friendship.

Finally, I want to express my gratitude to my family and friends for their unyielding support.

Chao ZHI